Universitá degli Studi di Roma "Sapienza"

FACOLTÀ DI SCIENZE MATEMATICHE, FISICHE E NATURALI

Corso di Laurea Specialistica in Astronomia e Astrofisica

ASTROPHYSICS ISSUES AND LOW FREQUENCY MECHANICAL NOISE FOR THIRD GENERATION GRAVITATIONAL WAVES DETECTORS

Tesi di Laurea Specialistica in Astronomia e Astrofisica

Relatori:

Prof. Fulvio Ricci

Dott. Riccardo De Salvo

Candidata:

Arianna Di Cintio

matricola 698482

Anno Accademico 2008/2009

II

Contents

1 Gravitational Waves **5**
- 1.1 GW in General Relativity . . . 5
- 1.2 Gravitational radiation from rotating stars . . . 8
- 1.3 GW from coalescing binary system . . . 10

2 Detection of gravitational waves **15**
- 2.1 Interferometric detectors . . . 15
- 2.2 LIGO and VIRGO . . . 17
- 2.3 Underground detectors . . . 21

3 Einstein Telescope: an european challenge **27**
- 3.1 ET project . . . 27
- 3.2 ET sensitivity curve . . . 30
- 3.3 ET astrophysics issues . . . 34
- 3.4 Detecting GWs from pulsars with ET . . . 39

4 Low frequency noise in Maraging blades **47**
- 4.1 Abstract . . . 47
- 4.2 Geometric Anti Spring (GAS) filter . . . 48
- 4.3 Experimental setup . . . 52
- 4.4 Motivations to this research . . . 57
- 4.5 Theoretical models . . . 58
- 4.6 Data acquisition, analysis and results . . . 61
  - 4.6.1 Thermal hysteresis . . . 61
  - 4.6.2 Hysteresis versus GAS filter frequency tune . . . 62
  - 4.6.3 Quality factor measurements . . . 65
  - 4.6.4 Low frequency instability . . . 70
  - 4.6.5 Expected and measured frequency versus amplitude . . . 76

4.6.6 Dissipation dependence from oscillation amplitude . . . 82

5 Conclusions **85**

A Labview code **93**

B Paper **95**

Riassunto

La teoria della Relativita' Genarale di Einstein predice l'esistenza delle onde gravitazionali (OG), perturbazioni della metrica dello spazio-tempo che viaggiano alla velocita' della luce. Negli anni passati sono stati compiuti notevoli sforzi in tutto il mondo per la costruzione di rivelatori interferometrici in grado di osservare tali segnali gravitazionali. I due interferometri LIGO (USA), il rivelatore VIRGO (Italia) e GEO600 (Germania) acquisiscono ed analizzano dati come un unico network dal Maggio 2007. I due rivelatori LIGO sono stati disegnati per essere sensibili alle onde gravitazionali nella banda di frequenza 40-7000 Hz, mentre VIRGO e' sensibile in un piu' ampio range, da 10 a 10000 Hz. Insieme a LISA, il primo osservatorio di onde gravitazionali che verra' costruito nello spazio, il cui obiettivo e' la rivelazione di OG nella banda 10^{-4}-1 Hz, l'unico range di frequenza non coperto sara' quello tra 1 e 10 Hz.
Tale range e' piu' che interessante: un'elevata sensibilita' a queste frequenze significherebbe, infatti, poter rivelare OG da sorgenti quali pulsars, coalescenza e merger di buchi neri di massa intermedia e background stocastico. La maggiore sfida nell'astronomia delle onde gravitazionali e', al momento, la realizzazione di un modello di rivelatore interferometrico di terza generazione, che dovrebbe essere in grado di raggiungere una buona sensibilita' nella banda di frequenza suddetta, dando cosi' il via ad una nuova era nell'osservazione della radiazione gravitazionale.
Nei primi due capitoli parlero' della teoria della rivelazione di OG mediante interferometri ed esporro' la necessita' di costruire una struttura sotterranea per coprire il range di frequenza 1-10 Hz.
L'Einstein Telescope (ET), un progetto Europeo volto alla realizzazione di un interferometro sotterraneo, sara' presentato nel terzo capitolo. Discutero' le sue caratteristiche, la sensibilita' attesa e le potenzialita' astrofisiche. Mostrero', inoltre, che e' possibile osservare, con l'antenna ET, l'emissione

di onde gravitazionali provenienti da qualche centinaio di pulsars.
Uno dei principali problemi, nella realizzazione di un interferometro di terza generazione, sara' la riduzione del rumore a basse frequenze, che e' dominato dal rumore sismico e da quello newtoniano: l'isolamento sismico gioca quindi un ruolo fondamentale nel miglioramento della banda di sensibilita' di questi interferometri a basse frequenze. Tutti i sistemi di isolamento sismico fin'ora sviluppati per gli interferometri LIGO, VIRGO e TAMA fanno uso di lame di acciaio Maraging, una lega che permette la produzione di molle (lame) prive di deformazioni permanenti. Sebbene tali lame offrano eccezionali prestazioni nell'attenuazione ad alte frequenze (>1 Hz), sono state osservate diverse anomalie a frequenze piu' basse.
L'argomento principale di questa tesi sara' presentato nel quarto capitolo, che e' il risultato del mio lavoro sperimentale al California Institute of Technology, nell'ambito del progetto LIGO.
Esso riguarda le proprieta' dissipative delle suddette lame, studiate a basse frequenze utilizzando un filtro GAS (Geometric Anti Spring) che, insieme al meccanismo EMAS (Electro Magnetic Anti Spring), ha reso possibile l'esplorazione di frequenze di risonanza al di sotto dei 100 mHz. A tale frequenza e' stata osservata, nel filtro GAS, una funzione di trasferimento inaspettata: questa e' una delle molte motivazioni che hanno condotto ad iniziare la presente ricerca.
Discutero' circa il filtro meccanico utilizzato, la procedura sperimentale, l'analisi dati e i risultati ottenuti. Parlero' inoltre del modello teorico che meglio illustra tali risultati.
Concludero' con una panoramica dei progetti futuri in questo campo.

Introduction

Einstein's theory of General Relativity predicts the existence of gravitational waves (GW), perturbations of the metric of the space-time traveling at the speed of light. In the past decades many efforts have been made worldwide in the construction of interferometric detectors capable to reveal such gravitational signals. The two LIGO interferometers (USA), the VIRGO detector (Italy) and the GEO600 one (Germany) are acquiring data as a unified network since May 2007. The initial LIGO detectors were designed to be sensitive to gravitational waves in the frequency band 40-7000 Hz, while VIRGO is sensitive in a wider frequency range, from 10 to 10000 Hz. Together with LISA, the proposed space-based gravitational waves observatory, whose goal is to detect GW in the range 10^{-4} to 1 Hz, the only sensitivity range not covered will be between 1 and 10 Hz.
This range is more than interesting: high sensitivity at those frequencies would mean the possibility to detect GW from sources as different as pulsars, coalescence and merger of intermediate mass black holes and the stochastic background. The major challenge in GW astronomy, at present, is the realization of the conceptual design of a third generation, lower frequency interferometric detector, which should be able to reach a good sensitivity in the above mentioned frequency range, thus opening a new GW era.
In the first two chapters I will talk about the theory of GW detection and I will expose the necessity to build an underground facility to cover the sensitivity range 1 to 10 Hz.
The Einstein Telescope (ET), the European design study project for the construction of an underground GW interferometer, will be presented in the third chapter. I will discuss its features, expected sensitivity and astrophysics potentialities. I will show, moreover, that the emission of continuous gravitational waves from a few hundred pulsars is detectable by the ET antenna, using its proposed sensitivity.

One of the major challenges, in the realization of a third generation GW detector, will be the reduction of the noise at low frequency, which is dominated by the seismic and the gravity gradient one: the seismic isolation thus plays a fundamental role in the improvement of the low frequency band sensitivity of these interferometers.
All seismic isolation systems developed for gravitational waves interferometric detectors, such as LIGO, VIRGO and TAMA, make use of Maraging steel blades, a precipitation hardened alloy that allows the production of creep-free blade springs. Although these springs provide exceptional attenuation performance at high frequency (>1 Hz), anomalies were observed at lower frequency.
The main subject of my thesis will be presented in chapter four, which is the result of my experimental work at the California Institute of Technology, LIGO project.
It concerns the dissipation properties of the above mentioned blades, studied at low frequencies using a Geometric Anti Spring (GAS) filter, which, together with the Electro Magnetic Anti Spring (EMAS) mechanism, allowed the exploration of resonant frequencies below 100 mHz. At this frequency an anomalous transfer function has been observed in the GAS filter: this is one of the several motivations for starting this research.
I will discuss the theoretical model which best explains our experimental findings, the mechanical filter that we used, the experimental procedure, the data analysis and the results obtained.
Finally, in chapter five, I will conclude giving an overview about the future plans in this field.

Chapter 1

Gravitational Waves

1.1 GW in General Relativity

One of the most fascinating predictions of General Relativity [1] is the existence of gravitational waves (GW): the information about a changing mass-energy distribution is carried out in the form of waves, which propagate away from the source at the speed of light c. The existence of such a waves has been inferred indirectly by studying the binary neutron star system PRS1913+16 [2][3], which loses energy at the rate predicted by General Relativity. The starting point are the Einstein field equations:

$$R_{\mu\nu} - \frac{1}{2} g_{\mu\nu} R = \frac{8\pi G}{c^4} T_{\mu\nu} \tag{1.1}$$

where $R_{\mu\nu}$ is the Ricci tensor, $g_{\mu\nu}$ the metric tensor, R the scalar curvature and $T_{\mu\nu}$ the stress-energy tensor. These equations connect the curvature of the space-time, given by $g_{\mu\nu}$, with the energy-mass distribution in the universe, expressed by the tensor $T_{\mu\nu}$. In the weak field approximation the curvature tensor $g_{\mu\nu}$ can be written as the Minkowski's one, $\eta_{\mu\nu}$, plus a small perturbation $h_{\mu\nu}$:

$$g_{\mu\nu} = \eta_{\mu\nu} + h_{\mu\nu} \tag{1.2}$$

with $|h_{\mu\nu}| \ll 1$.
By solving the Einstein's equations for the metric (1.2), in the vacuum space and in the linear approximation, we get:

$$(\nabla^2 - \frac{1}{c^2}\frac{\partial^2}{\partial t^2})h_{\mu\nu} = 0 \tag{1.3}$$

whose solution is a monocromatic plane wave travelling at c.
Using the transverse-traceless gauge it is possible to demonstrate that a gravitational wave has only two physical degrees of freedom, which correspond to the two possible polarization states; the tensor $h_{\mu\nu}$ is different from zero on the plane orthogonal to the direction of propagation of the wave and, for a wave moving along the x axis, we have:

$$h^{TT}_{\mu\nu} = \begin{pmatrix} 0 & 0 & 0 & 0 \\ 0 & 0 & 0 & 0 \\ 0 & 0 & h_{yy} & h_{yz} \\ 0 & 0 & h_{yz} & -h_{yy} \end{pmatrix} \tag{1.4}$$

A gravitational wave can thus be expressed as a combination of two terms taking into account the "plus" and "cross" polarization states

$$h_{yy} = h_{\oplus} = \Re\{A_{\oplus} e^{i\omega(t-\frac{x}{c})}\} \qquad h_{yz} = h_{\otimes} = \Re\{A_{\otimes} e^{i\omega(t-\frac{x}{c})}\} \tag{1.5}$$

which generate, respectively, the space deformation shown in fig.1.1:

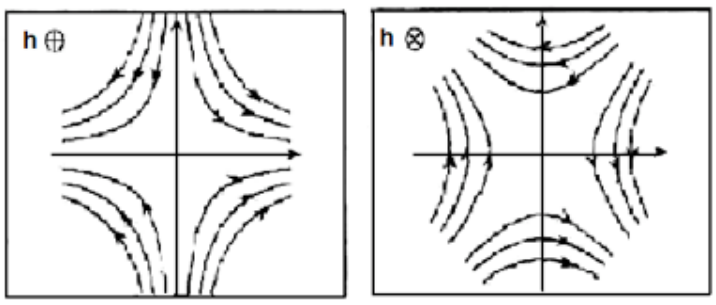

Figure 1.1: Space deformation due to the propagation of gravitational waves, for the two polarization states.

Since the transit of gravitational waves does not affect the motion of a single particle, because it only changes the metric locally, we have to study the proper distance between two particles in order to detect those waves.

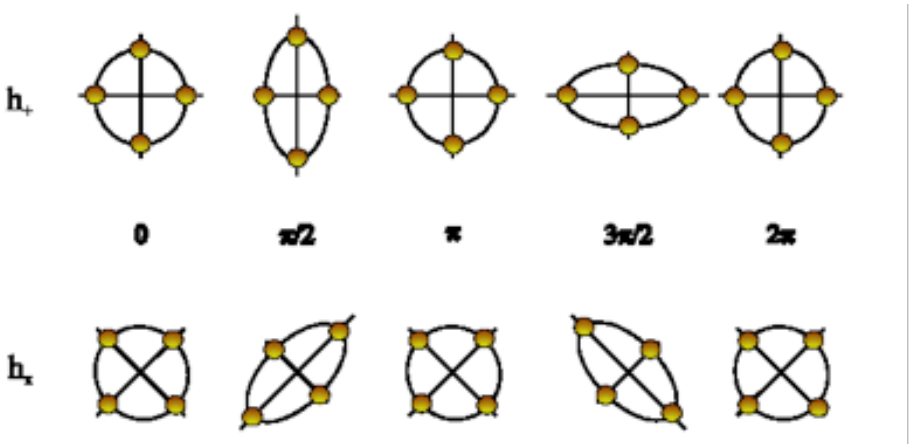

Figure 1.2: Effect produced by a gravitational wave crossing a circumference of test particles.

Starting from the equation of geodesic deviation, which shows that the relative acceleration of two close particles A and B depends on the curvature tensor, and considering a gravitational wave propagating along the x direction with polarization state $h_{\oplus}$, we obtain [41]:

$$\frac{\triangle l_{AB}}{l_{AB}} = \frac{h_{yy}}{2} \tag{1.6}$$

where l_{AB} is the relative position of the particle A with respect to the particle B. Equation (1.6) points out that, even if the two free masses will remain fixed in their coordinate positions, their relative distance will extend and contract at the frequency of the gravitational wave crossing them.

How large is the amplitude of a gravitational wave? To answer to this question we first have to note that, unlike the electromagnetic case, gravitational radiation cannot be associated with a dipole contribution: by defining a gravitational dipole moment $\overrightarrow{d_G} = \sum_i m_i \overrightarrow{r_i}$ we see that for an isolated system of masses it must satisfy the conservation law of the total momentum, thus giving $\frac{d^2}{dt^2}\overrightarrow{d_G} = 0$.
Gravitational waves have an intrinsic quadrupolar nature. Developing the stress-energy tensor in multipoles we get, for the strongest component of the gravitational radiation,

$$h_{\mu\nu} = \frac{2G}{c^4 r}\ddot{Q}_{\mu\nu} \tag{1.7}$$

where r is the distance from the emitting source and $\ddot{Q}_{\mu\nu}$ is the second time derivative of the reduced quadrupole moment, defined as

$$Q_{\mu\nu} = \int dV(x_\mu x_\nu - \frac{1}{3}\delta_{\mu\nu}r^2)\rho(r). \tag{1.8}$$

From (1.7) follows that, since the term $\frac{G}{c^4} \sim 10^{-50} s^2/g\ cm$, the amplitude of a gravitational wave is extremely small: for this reason the only detectable sources are astrophysical sources.
The most promising events in this sense are non-radial pulsation of neutron stars, non-axial collapse of supernovae and coalescence of massive bodies, such as black holes and massive stars, as well as the stochastic background from the big bang.

1.2 Gravitational radiation from rotating stars

From equation (1.8) it follows that, in order to emit gravitational waves, an object rigidly rotating around its symmetry axis must have some degree of asymmetry; otherwise its reduced quadrupole moment is constant. It is useful to express $Q_{\mu\nu}$ in terms of a dimensionless parameter ϵ, the ellipticity, which expresses the deviation from axisymmetry [5]:

$$\epsilon = \frac{a-b}{(a+b)/2} \tag{1.9}$$

where a and b are the two semiaxes of the star, as shown in fig.1.3.

If the pulsar is rotating around the z axis with an angular velocity Ω and a moment of inertia I_3, then the quadrupole moment is found to be

$$Q_{\mu\nu} = \frac{\epsilon I_3}{2} \begin{pmatrix} \cos 2\Omega t & \sin 2\Omega t & 0 \\ \sin 2\Omega t & -\cos 2\Omega t & 0 \\ 0 & 0 & 0 \end{pmatrix} + constant \tag{1.10}$$

The last equation shows that GW are emitted at twice the rotation frequency of the star. Using eq (1.7) and the transverse-trasless projector $P_{jkmn} = P_{jm}P_{kn} - \frac{1}{2}P_{jk}P_{mn}$, which selects the transverse-traceless part of a tensor, we finally obtain a waveform

$$h^{TT}_{\mu\nu} = \frac{4G\Omega^2 I_3 \epsilon}{c^4 r} \left[P \begin{pmatrix} -\cos 2\Omega t' & -\sin 2\Omega t' & 0 \\ -\sin 2\Omega t' & \cos 2\Omega t' & 0 \\ 0 & 0 & 0 \end{pmatrix} \right] \tag{1.11}$$

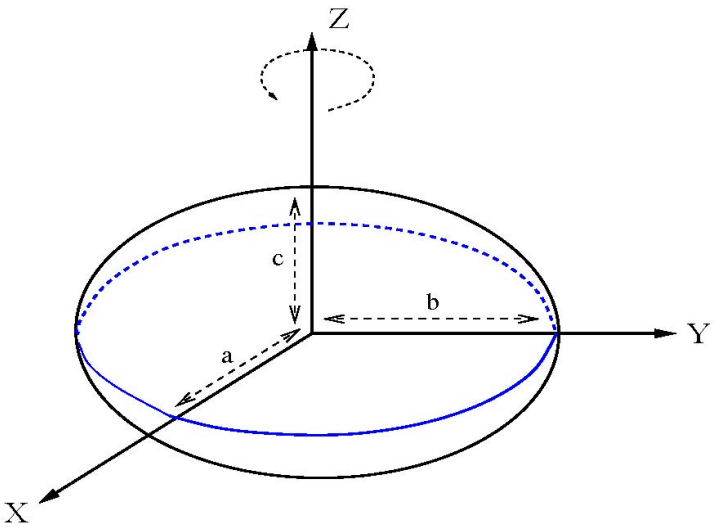

Figure 1.3: Schematic of a pulsar rotating along its z axis, with angular velocity Ω and ellipticity ϵ. Picture from [5].

where $t' = t - \frac{r}{c}$ is the retarded time.
The constant part of eq (1.11) can be normalized as follow

$$h_0 = 2.08 \cdot 10^{-25} (\frac{\Omega}{100Hz})^2 (\frac{Kpc}{r})(\frac{I_3}{10^{38}Kgm^2})(\frac{\epsilon}{10^{-6}}) \tag{1.12}$$

where we selected standard values for the moment of inertia and the ellipticity. By defining two polarization states,

$$h_{\oplus} = \frac{h_0}{2} cos2\Omega t'(1 + cos^2\theta) \tag{1.13}$$

$$h_{\otimes} = h_0 sin2\Omega t' cos\theta \tag{1.14}$$

with θ angle between the rotation axis of the star and the line of sight, we finally obtain the equations that connect the amplitude of gravitational waves with the geometrical properties of the rotating star. From (1.12) it is clear that the knowledge of ϵ is fundamental to estimate this wave amplitude: new observational upper limits have been set on this value, based on the

assumption that pulsars spin-down (i.e. the rotational period increases with time) is due to both electromagnetic and gravitational torque [6].

pulsar name	$\nu_{GW}(Hz)$	ϵ_{max}	h_{max}
Vela	22.4	$3.3 \cdot 10^{-4}$	$3.5 \cdot 10^{-25}$
Crab	59.9	$3 \cdot 10^{-4}$	$5.5 \cdot 10^{-25}$
PSR0540-69	39.7	$2.4 \cdot 10^{-4}$	$3.2 \cdot 10^{-26}$

On the other hand, theoretical studies, that take into account the maximum strain that the crust of a neutron star can support without breaking, set a further constraint on ϵ:

$$\epsilon \lesssim 10^{-7} \tag{1.15}$$

At the present, given the high uncertainty on the ellipticity, it is reasonable to consider ϵ as a parameter to be determined with the detection of gravitational waves from neutron stars.

1.3 GW from coalescing binary system

Let us consider a binary system composed of two stars, or black holes, moving on a circular orbit around their common center of mass, and let's assume that these two masses, m_1 and m_2, are pointlike. By defining $l = r_1 + r_2$ as shown in fig.1.4 and an orbital frequency $\omega = \sqrt{G(m_1 + m_2)/l^3}$, in the quadrupole formalism and using the TT gauge, we get:

$$h^{TT}_{\mu\nu} = -\frac{4m_1 m_2 G^2}{rlc^4}[P_{\mu\nu kl} A_{kl}] \tag{1.16}$$

where r is, as usual, the distance from the source and $P_{\mu\nu kl}$ the transverse-traceless projector.
The quantity A_{kl} is defined as

$$A_{kl} = \begin{pmatrix} \cos 2\omega t & \sin 2\omega t & 0 \\ \sin 2\omega t & -\cos 2\omega t & 0 \\ 0 & 0 & 0 \end{pmatrix} \tag{1.17}$$

from which we see that the radiation is emitted at twice the orbital frequency.

From eq (1.16) we can estimate, for example, the dimensionless amplitude of the gravitational waves emitted by the binary system PRS1913+16 discovered by Hulse and Taylor:

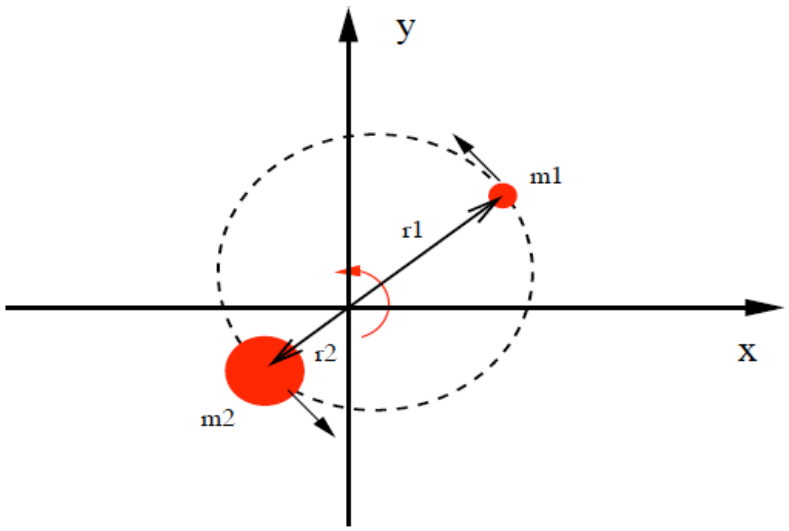

Figure 1.4: Binary system rotating around its center of mass. Picture from [5].

$$h_{0-PSR1913+16} = \frac{4m_1m_2G^2}{rlc^4} \sim 5 \cdot 10^{-23} \tag{1.18}$$

The orbital period of a binary system decreases in time due to gravitational waves emission, and the orbital frequency will increase corresponding

$$\omega(t) = \omega^{in}\left[1 - \frac{t}{t_{coal}}\right]^{-3/8} \tag{1.19}$$

with $\omega^{in} = \sqrt{G(m_1+m_2)/l_{in}^3}$ and

$$t_{coal} = \frac{5}{256}\frac{c^5}{G^3}\frac{l_{in}^4}{(m_1+m_2)m_1m_2} \tag{1.20}$$

Of course, since we are talking about stars and black holes that are not pointlike, the system will start merging and coalesce before $t = t_{coal}$. Eq (1.20), however, gives an indication of the time the two bodies need to merge beginning from an initial distance l_{in}. The distance $l(t)$ will decrease as well, following

$$l(t) = l_{in}\left[1 - \frac{t}{t_{coal}}\right]^{1/4} \tag{1.21}$$

The instantaneous amplitude of the emitted wave can now be found by substituting eq (1.21) into eq (1.16)

$$h_0(t) = \frac{4m_1m_2G^2}{rl(t)c^4} = \frac{4m_1m_2G^2}{rc^4}\frac{\omega^{2/3}(t)}{G^{1/3}(m_1+m_2)^{1/3}} \tag{1.22}$$

and, by defining a *chirp mass* $M = (m_1m_2)^{3/5}/(m_1+m_2)^{1/5}$ and recalling that the frequency of the emitted wave ν_{GW} is twice the orbital frequency, we finally obtain:

$$h_0(t) = \frac{4\pi^{2/3}(GM)^{5/3}}{c^4 r}\nu_{GW}^{2/3}(t) \tag{1.23}$$

The last equation shows that the frequency and amplitude of the gravitational radiation emitted by a coalescing system increases with time. This waveform is called *chirp* and is directly proportional to the mass of the two bodies involved in the merging process: coalescence of black holes and/or neutron stars is thus the most promising event to be detected. A typical waveform is shown in fig.1.5, in which the three stages of inspiral, merger and ring-down are highlighted.

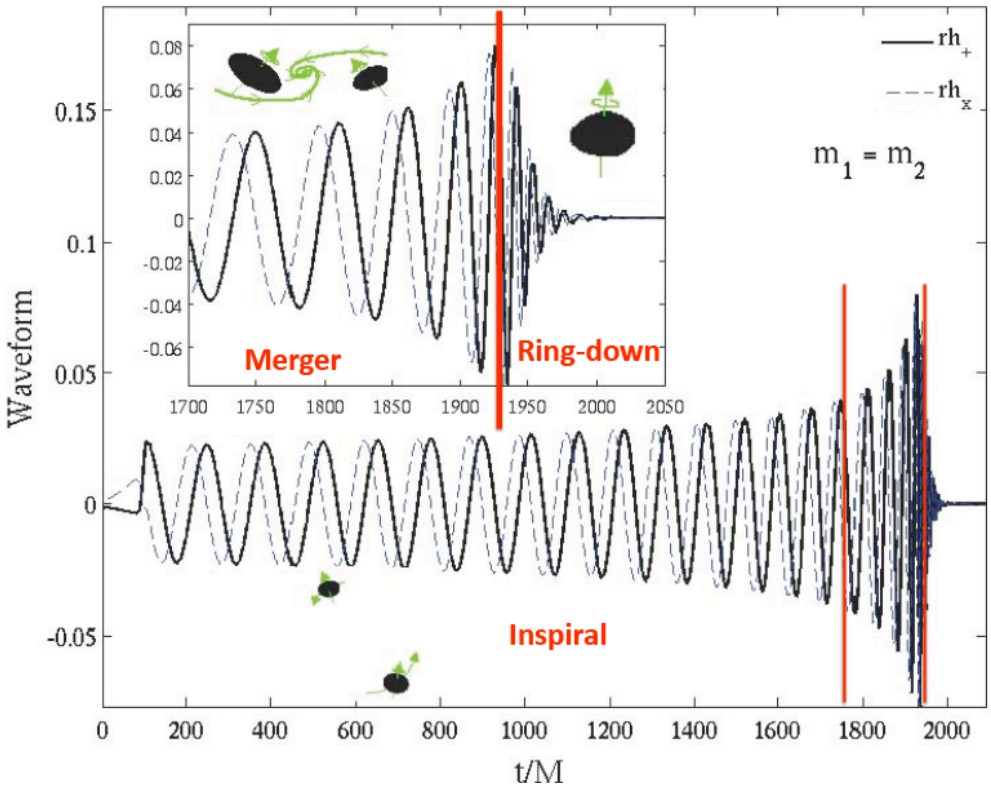

Figure 1.5: Characteristic waveform generated by coalescing bodies.

Chapter 2

Detection of gravitational waves

2.1 Interferometric detectors

To detect a gravitational wave we have to measure the displacement between test masses separated by a very large distance in order to obtain a significant signal (see eq.(1.6)). A simple Michelson interferometer appears to be the most useful solution, since we can monitor the relative separations of test masses by measuring the round trip travel time of light beams. The basic configuration of a Michelson interferometer is shown in fig.2.1.

The beam splitter divides the incoming laser beam into two equal intensity, orthogonal beams, which are reflected from the two mirrors at the end of each arm, and recombined on the beam splitter surface. A fraction of the recombined beam transmits through the beam splitter and the rest is reflected from it. The intensity of such a beam is detected by a photodetector. Assuming that a gravitational wave is passing through the interferometer, the difference between the travel time of each laser beam into the two arms is:

$$\triangle\tau(t) = h(t)\frac{2L}{c} \tag{2.1}$$

where L is the arm length. The previous equation can be written in terms of wave phase variation:

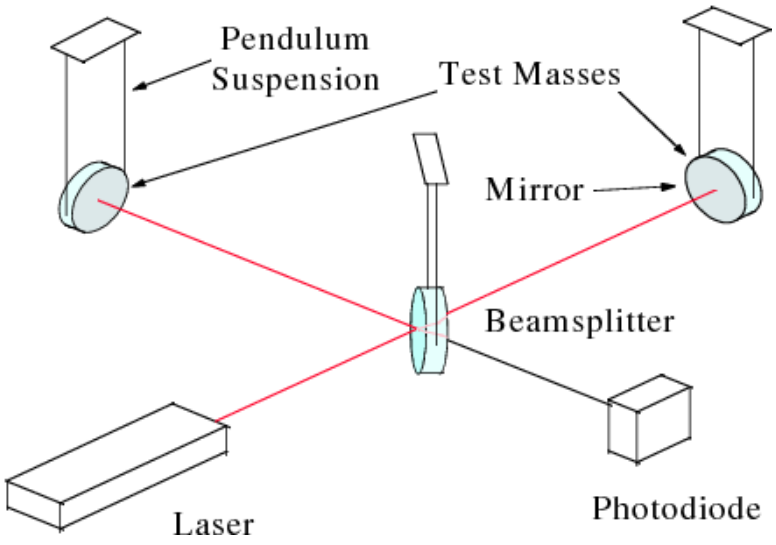

Figure 2.1: A simple Michelson interferometer.

$$\triangle\phi(t) = \triangle\tau(t)\frac{2\pi c}{\lambda} = h(t)\frac{4\pi L}{c} \tag{2.2}$$

where λ is the laser wavelenght. The phase shift described above is the guiding principle to detect gravitational waves: at the interferometer's output the well-known interference fringes will appear, and, by measuring the output power through a photodiode, it is immediate to get information about the amplitude of the metric perturbation $h(t)$. The interferometer operates on a dark fringe, where the resulting intensity at the photodetector is minimized: this also reduces the signal amplitude, but the remaining power is rejected on the other arm back towards the laser.
From eq.(2.1) and (2.2) it is clear that the larger is the arm length L the larger is the phase variation $\triangle\phi(t)$, and the optimal solution would be to build a Michelson interferometer with arms of thousands of km: this can only be accomplished in space and another solution has to be found for ground-based detectors. The problem is solved by inserting a Fabry-Perot cavity in each arm, in which the optical path of the light beams is folded. This cavity consist of two suspended mirrors, as in fig.2.2.

Inside the Fabry-Perot cavity the laser beam is reflected several times, generating spatially superposed beams, so the amplitude of the light that would reach the photodiode is the coherent sum of the individual beams. The

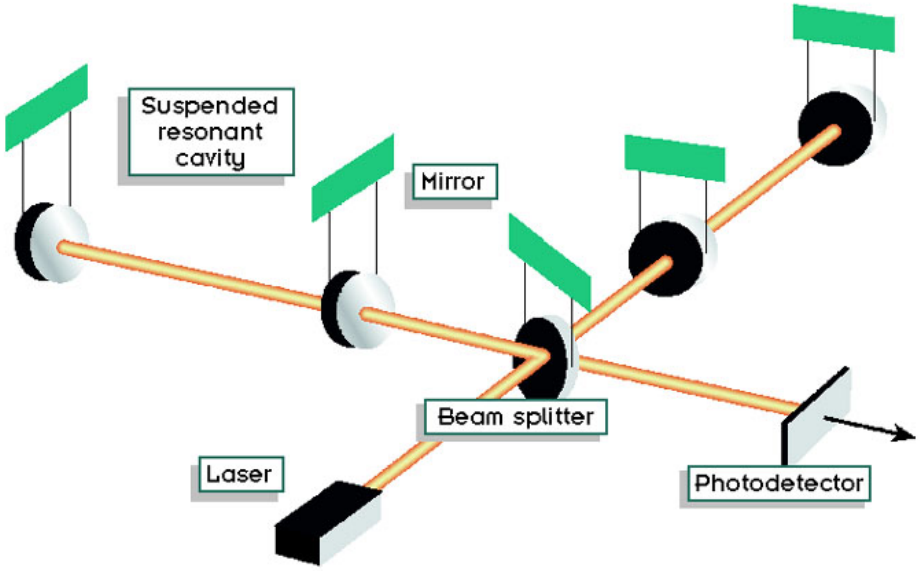

Figure 2.2: Suspended Fabry-Perot cavities placed along the interferometer arms. Each cavity is composed by the end mirror and the intermediate one.

optical cavity is kept in resonance, assuring the maximum power transmitted. In this configuration the GW induced phase shift of the light returning to the Michelson beam splitter is increased by a factor proportional to the finesse of the Fabry-Perot. To conclude, let's say that most of the input laser power is reflected from the interferometer back toward the laser source, and since increasing the laser power results in better sensitivity, a partially transmitting mirror can be placed between the input laser and the beam splitter: this is the so called power recycling.

2.2 LIGO and VIRGO

Many interferometric detectors have already been built around the world, such as LIGO (USA), VIRGO (Italy), GEO600 (Germany) and TAMA (Japan). Funded by the NSF (National Science Foundation), LIGO is a collaboration between scientists from the California Institute of Technology and the Massachusetts Institute of Technology. The LIGO project [7][8] consist of two observatories, one in Hanford, Washington, which houses two interferom-

eters with armlengths of 4 km and 2 km respectively, and the other one in Livingston, Louisiana, again with 4 km long arms: at least two detectors located at widely separated sites are essential, in fact, for the certain detection of gravitational waves, to reject instrumental and environmental noises and to determine the direction of the source. Two modification to a basic Michelson, shown in fig.2.4, increase the carrier power in the arms and hence the sensitivity. First, each arm contains a resonant Fabry-Perot cavity, which multiplies the signal by a factor of 100 at 100 Hz. Second, a partially-reflecting mirror is placed between the laser and the beam splitter to implement power recycling: in this configuration the LIGO interferometers increase the power in the arms by a factor of 8,000 with respect to a simple Michelson. The laser source emits 10W in a single frequency at 1064 nm, and its power and frequency are actively stabilized through a mode cleaner cavity. All the main interferometer optical components and beam path are enclosed in the ultra vacuum system to avoid phase shifts from the noise of air density fluctuations and for acoustical isolation. Each mirror is suspended as a pendulum by a loop of steel wire and the bulk of the vibration isolation is provided by four-layer mass-spring isolation stacks, to which the pendulums are mounted. The position and orientation of the suspended optics is controlled by electromagnetic actuators.

Figure 2.3: The Hanford and Livingston LIGO interferometers.

VIRGO [9][10] is an European collaboration, funded by the French CNRS and the Italian INFN, located within the site of EGO (European Gravitational Observatory), based at Cascina, near Pisa (Italy). VIRGO is optically similar to LIGO, with two orthogonal, 3 kilometers long arms. In each arm, a two mirror Fabry-Perot cavity extends the effective optical length from 3 to

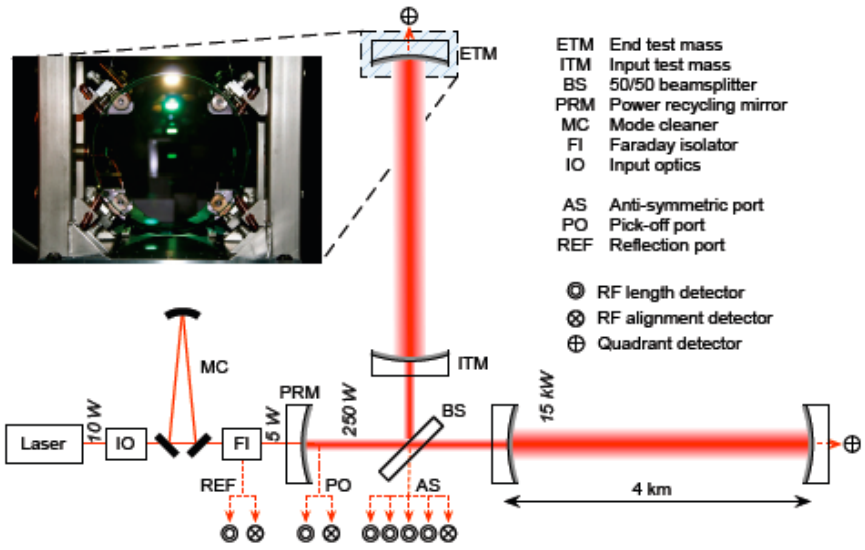

Figure 2.4: Optical configuration of the LIGO 4 km interferometers. The insert photo shows an input test mass mirror in its pendulum suspension.

about 1000 kilometers and, in order to increase the beam power, a recycling mirror is placed just after the interferometer input, exactly as in LIGO. The central area contains a huge optical table under ultra high vacuum, and each optical element is suspended to a seismic isolation system contained in a vacuum tower. The tower themselves are linked by vacuum tubes. The seisimc isolation is achieved through a chain of suspended seismic filters made of triangular cantilever Maraging blade springs, similar to those later studied in this thesis; the whole system is called the SuperAttenuator. The springs provide the vertical isolation while the inverted pendulum provides isolation against horizontal motion. The ultimate mirror position control is obtained through small forces generated between the mirror and a recoil mass by sets of electro-magnetic actuators. The 20 watts laser beam of VIRGO is stabilized in frequency and amplitude through a mode cleaner cavity.

Early in its operation GEO joined with the LIGO project [11], and although with its shorter length the GEO600 detector is not as sensitive as the LIGO detectors, for strong sources it can provide added confidence and directional and polarization information. In May 2007 the VIRGO detector

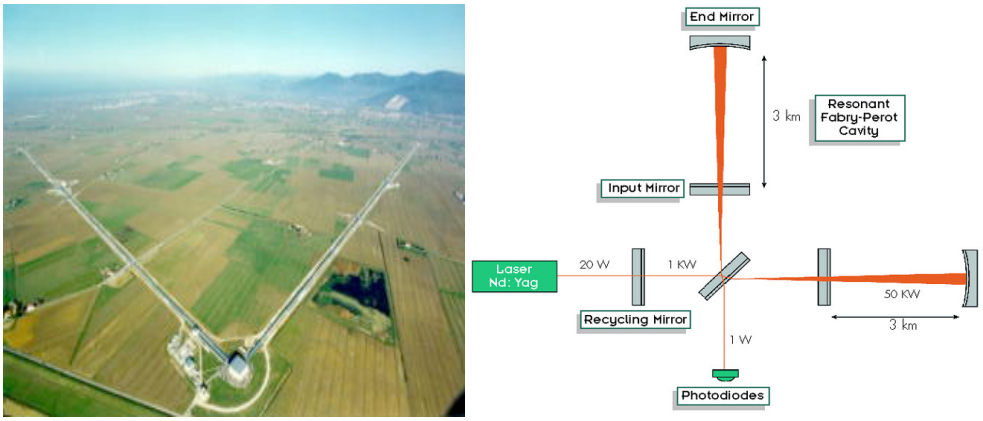

Figure 2.5: Picture and schematic of the VIRGO interferometer, Cascina.

began joint observations with LIGO. Since that date all four observatories are taking data as an unified network. The initial LIGO detectors were designed to be sensitive to gravitational waves in the frequency band 40-7000 Hz, while VIRGO is sensitive in a wider frequency range, from 10 to 10000

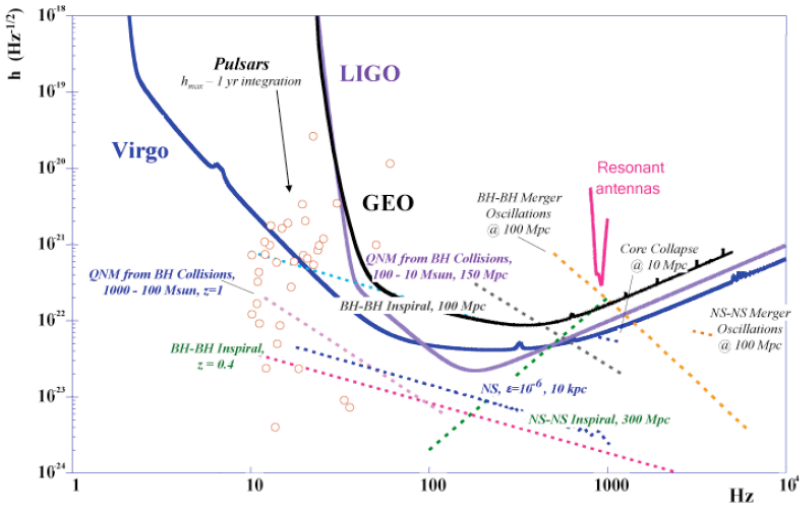

Figure 2.6: The sensitivity curves of LIGO, VIRGO and GEO600 are compared. The estimates for some of the possible signals coming from astrophysical sources are indicated. Picture from [12].

Hz; a comparison between their sensitivity curves is shown in fig.2.6. The above mentioned ranges, as well as the very high sensitivity of these interferometers, should allow the detection of gravitational radiation caused by the coalescence of binary systems or produced by pulsars and supernovae in the milky way and nearby galaxies. So far, unfortunately, no GW have been detected over the expected background of instruments noise.

2.3 Underground detectors

The second generation interferometers, such as Advanced LIGO and Advanced VIRGO, will give more than a factor of 10 greater sensitivity, in the same frequency range, with respect to the initial detectors. Together with LISA [13] (Laser Interferometer Space Antenna), the proposed first dedicated space-based gravitational wave observatory whose goal is to detect GW in the range 10^{-4} to 1 Hz, the frequency spectrum covered will be as in fig.2.7:

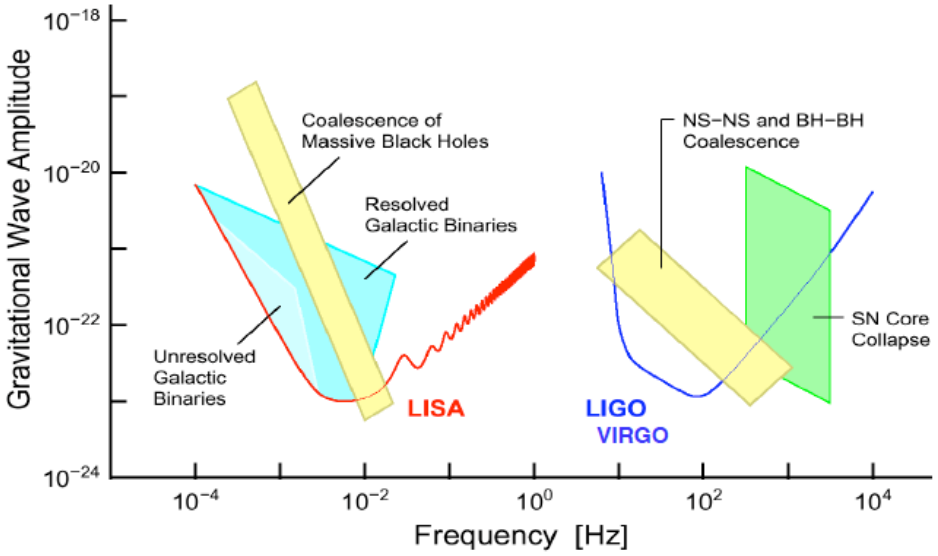

Figure 2.7: The sensitivity curve of the Advanced detectors and LISA.

It is now evident that, even combining these sensitivities, there is still a gap between 0.1 and 10 Hz, where the present detectors are unable to reveal GW. LISA sensitivity is limited, at high frequencies, by the laser

shot noise, while the sensitivity curves of LIGO and VIRGO are limited, at low frequencies, by the seismic and the gravity gradient noise, which are the dominating noise sources below 10 Hz. The seismic noise is due to the continuous ground motion which results in a perturbation of the test masses position: it comes from human activity as well as from micro-earthquakes, ocean wave activity, atmospheric pressure variation and movements of the Earth's crust. The seismic noise spectral density is described by [14]:

$$x(f) = \frac{\delta}{f^2}\frac{m}{\sqrt{Hz}} \tag{2.3}$$

where the δ constant changes with respect to the site between 10^{-9} and 10^{-6}. At 10Hz, a value of $\delta \sim 10^{-6}$ would thus produce a displacement, in the test masses position, of $10^{-8}m/\sqrt{Hz}$, which is several orders of magnitude greater than the GW amplitude that we want to reveal. Seismic isolation is thus fundamental to achieve good sensitivity at low frequency. However, even with its seismic attenuation system, LIGO is able to reach a good sensitivity ($S_n^{1/2}(f) \leqslant 10^{-19}Hz^{-1/2}$) only above 40 Hz and Advanced LIGO above 10 Hz; below these frequencies, there is the so called "seismic wall", which depends from the resonant frequency of the used attenuator. Moreover, connected with the seismic one, the gravity gradient noise sets a limit to the sensitivity at low frequency. When the distribution of matter in the vicinity of the interferometer is time dependent, then the gravitational field will fluctuate as well, coupling with the test masses and giving a spurious response. The mass density fluctuations are driven by micro-seismic waves propagating on the ground and by acoustic pressure waves in the atmosphere. The gravity gradient noise spectral density decreases as f^4 [14]: it is necessary to monitor the density perturbation of masses which are close enough to the test masses, calculate the fluctuating gravitational forces thus produced, and correct the data stream taking into account these forces. This procedure, however, is not trivial: the surface variability would require a forbidding density of high precision seismic motion sensors

How can the sensitivity of GW interferometers be improved at low frequency and how can be the gap at 1 Hz be filled? A possible answer is by going underground. Different types of seismic waves, as in fig.2.8, can produce gravity gradient noise, but the Rayleigh waves, which have both vertical and longitudinal components, are the greatest concern in this scenario. An interesting property of such a waves, however, is that the displacement decreases exponentially with depth, with a decreasing rate dependent on the wavelength,

as in fig.2.9.

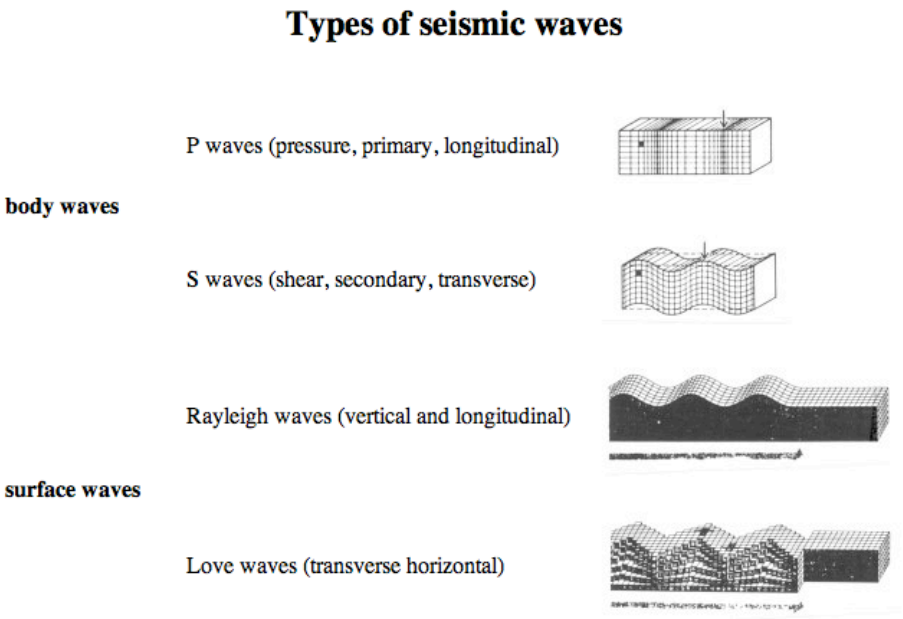

Figure 2.8: Illustration and characteristics of the seismic waves.

Developing an underground GW detector would thus be beneficial for this source of gravity gradient noise: apart from the natural improvement due to the exponential reduction of the seismic noise, which is proportional to $e^{-4d/\lambda}$ where d is the depth and λ the wavelength, the speed of sound 2 km underground is around 5 km/s, implying that the seismic waves in the 0.1-10 Hz band will have a very large wavelength, around 500 m-50 km. This value is much larger than the size of a cavity that would host the interferometer mirror, so the passage of seismic waves would have only a small effect on the gravitational field at the center of the cavity. In addition to this, the atmospheric fluctuations would have negligible effect on the gravitational field deep underground and the air pressure and temperature variations can be reliably monitored and stabilized. Finally, the human-induced gravitational fluctuations are much more controllable underground.

There are several question, however, to be answered in order to have a clear idea of the effective sensitivity of these interferometers:

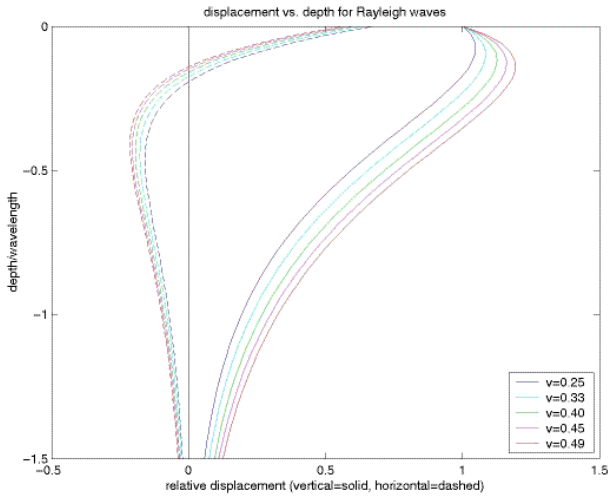

Figure 2.9: Rayleigh waves displacement versus depth. Picture from [16].

1. How does the amplitude of the seismic noise vary as a function of depth and frequency?

2. How large is the non-uniformity of the underground rock density, and what is its impact on the gravity gradient noise?

3. What is the correlation length of the seismic noise, as a function of depth and frequency?

4. How large is the anisotropy in sound velocity, and what is its impact on the gravity gradient noise?

In order to find these answers many scientists have already been involved in this study: I want to underline, particularly, the DUSEL (Deep Underground Science and Engineering Laboratory) [15] proposal, a collaboration project between Caltech, the University of Minnesota, Florida, Carleton and Lousiana State, whose goal is the design of a future underground GW detector that will target the 0.1-10 Hz band. The research proposal is to perform a detailed set of measurements of the seismic motion in the Homestake mine, South Dakota, as well as to develop a model that would estimate the gravity gradient noise caused by the measured seismic noise. My connection to this project is the possible contribution in understanding the noise properties

of the flexures of the sensors that should be used for gravity gradient subtraction. Another project, already in its design study phase, is the Einstein Telescope (ET), supported by the European Commission: an overview of ET will be given deeply in the next chapter, together with the very strong scientific motivations for exploring the 1 Hz frequency region, in which several astrophysical sources are expected to emit gravitational radiation. To conclude, the realization of a third generation, underground interferometer for GW detection seems to be the most promising solution to study the frequency range below 10 Hz.

Chapter 3

Einstein Telescope: an european challenge

3.1 ET project

The Einstein Telescope (ET) [17] is a design study project supported by the European Commission under the Grant Agreement 211743. It concerns the conceptual design of a new underground gravitational waves detector, with eight european research institutions working together to achieve the target. This third generation detector should potentially cover the complete frequency range from about 1 Hz to 10 kHz that is observable from ground. Four technical working groups have been established in order to study the feasibility of this observatory: site location and characterization (WP1), suspension design and technologies (WP2), detector topology and geometry (WP3) and astrophysics potentialities (WP4).
Current GW detectors are limited, in the low frequency range, by the seismic noise that enters in the detector sensitivity both through the seismic filter chain used to suspend the main optics of the interferometer and by direct gravitational coupling of the vibrating soil with the suspended masses (the so-called Newtonian noise or gravity gradient noise). Additionally, low frequency sensibility is limited by the radiation pressure and the by mirror control noise.

The first target of the ET design study is to identify the strategies to

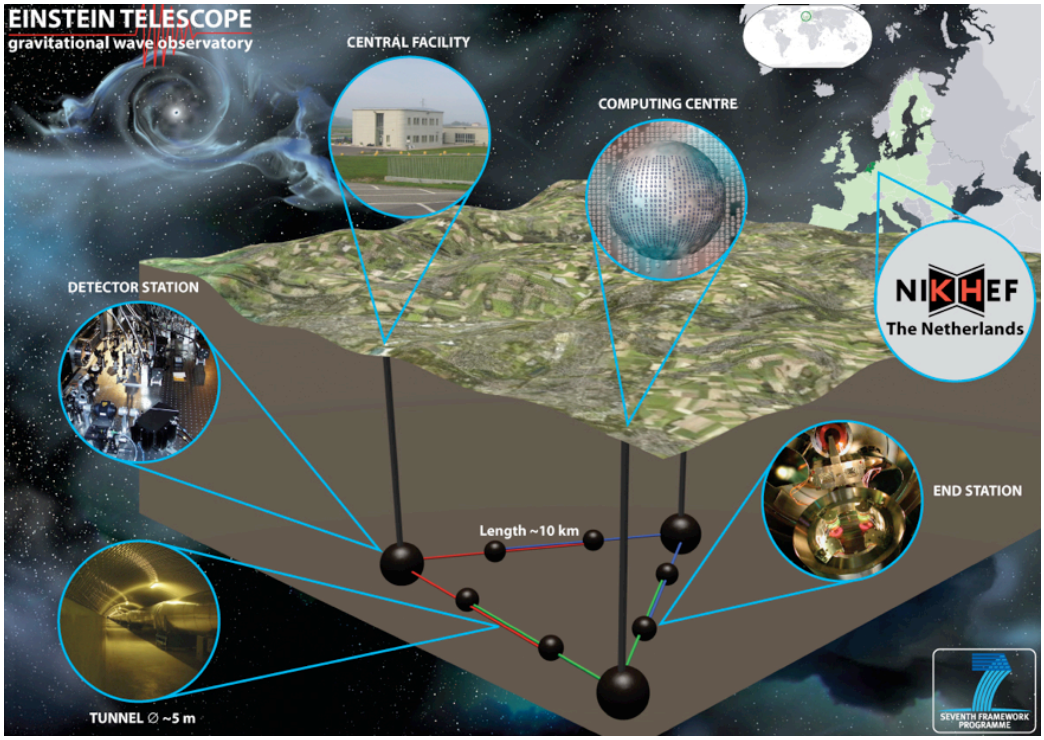

Figure 3.1: Picture of a possible ET configuration, from [17].

reach a further reduction of the seismic noise effects with respect to the second generation detectors expectations. This is expected to be attained trough in two parallel ways:

- identification of a site with a lower seismic and Newtonian noise
- improvement of the mirror vibration isolation and of the controllability of the suspension

The first one is the main activity of the first work package: the definition of the site requirements and the proposition of the possible sites in Europe, having satisfactory specifications. The need to reduce both the seismic and Newtonian noise seems to be fulfilled by an underground site, where the reduced seismic activity and the uniformity of the rock is expected to play a dominant role in improving the GW detector sensitivity. For example measurements at the Japanese Kamioka underground site (1000 m underground from the top of the mountain) reveal an average reduction of seismic noise of

about 10^2 (and as much as 10^3 at 4 Hz) compared to surface sites. It is important to note, however, that one can always improve the mechanical seismic isolation on the surface, by adding several stages in the attenuation chains: the real justification of an underground site is the reducton of the Newtonian noise, which requires necessarily an underground location to be lowered. The use of active reduction of Newtonian noise using information from seismometers, accelerometers, strainmeters and tiltmeters to the test masses will be studied as well. The final result of the above described studies will be a conceptual design report on the requirements for seismic displacement noise and gravity gradient noise.

The second target of the ET design study is the identification of the specifications of the last stage suspension and test mass that can satisfy the thermal noise requirements of a third generation GW detector. The suspensions of the optical elements of the interferometer are among the most crucial components of the detector. They must provide the necessary attenuation from seismic and acoustic noise and must implement the control strategy necessary to keep the interferometer at its working point. The first step of the conceptual design will be a study which will define material, size, optical properties, input power, desired attenuation and desired temperature for the mirror. For instance, the mass of the mirror itself must be decided according to the necessity to limit both the suspension thermal noise and the motion noise due to the recoil of the mirror from radiation pressure. Once the mirror properties will be identified, the design of the suspension chain will continue on two parallel paths: the definition of the upper part and the design of the last stage. The outcome of the study will be a conceptual design of the suspension including many highlights on the control strategies to be implemented.

The third target of the ET study is to find and define a conceptual design of the core interferometer with regard to geometry, topology and configuration that can surpass the Standard Quantum Limit (SQL) significantly. The parallel tasks of work package 3 (WP3) are dedicated to:

- detector geometry: the boundary conditions for the detector geometry are defined by the possible sites (WP1) and the type of gravitational waves we aim to detect with maximum signal-to-noise ratio (WP4)
- reduction of quantum noise : a rich selection of optical technologies

have been proposed to reduce the quantum fluctuation below the SQL

The baseline of the ET design study is the expected performance of the advanced detectors; any further improvement of the design concepts must be compared with the expected sensitivity of the Advanced LIGO and Advanced Virgo detectors. The aim is to arrive to the conceptual design of a 3rd generation GW detector showing a sensitivity curve roughly an order of magnitude better than the advanced detectors, opening, in this way, the astronomy era for the GW radiation.

3.2 ET sensitivity curve

A quantitative way to evaluate the advance respect to the baseline of the project is represented by the sensitivity curve, reported in the following figure.

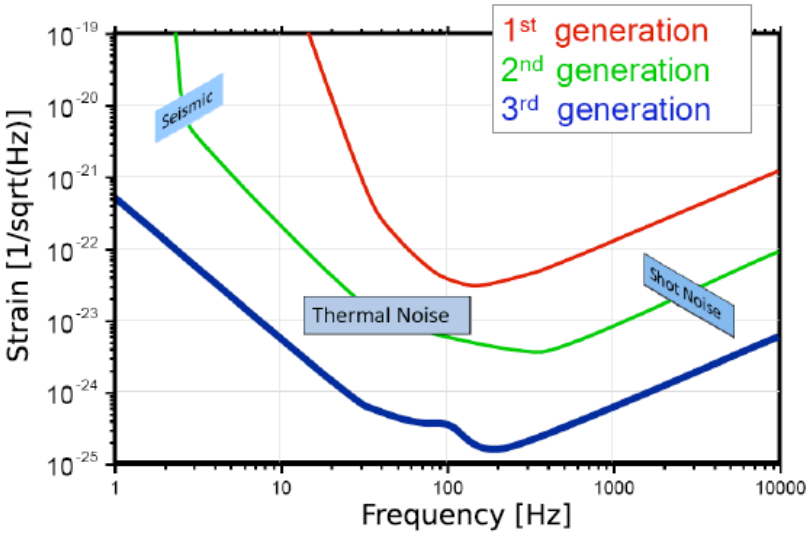

Figure 3.2: Comparison between the sensitivity curves of the different GW interferometric detectors. The 3rd generation curve represents the envelope of the improvement attainable for this kind of detectors. Picture from [18].

An initial analysis has been made by the Birmingham group [19] in order to obtain this sensitivity curve starting from the advanced interferometers

noise curve. The idea is to show, step by step, which modifications and improvements are necessary to go from second generation gravitational waves detectors to the Einstein Telescope.
The following list indicates briefly some of the parameter changes that have been performed to obtain the curve of fig.3.2.

1. The arm length has been increased from 3 to 10km, which proportionally reduces the relative effects of all displacement noises (seismic, suspension thermal etc.) by a factor 3.3.

2. The laser input power has been increased from 125 Watt to 500 Watts, which yields an intracavity power of about 3MW. The value of 500Watts has been chosen as a trade off between improved shot noise at high frequencies and higher radiation pressure noise at low frequencies.

3. A reduction of the temperature from 290 to 20K has been made. Going to cryogenic temperatures could involve a change of the test mass material from fused silica to sapphire.

4. In order to reduce the noise from residual gas pressure we had to improve the vacuum from $1.2 \cdot 10^{-7}$ to at least $5 \cdot 10^{-9}$ mbar. This challenging value is necessary to get the residual gas pressure noise just a tiny bit below the ET target.

5. The next step was to reduce the seismic noise. The Virgo super attenuator has been replaced by a suspension consisting of 5 stages each 10m long. A simplified spectrum of the horizontal seismic noise measured at Virgo site has been used ($1 \cdot 10^{-7} m/f^2$ for $f > 1Hz$).

6. In order to further improve the sensitivity we had to go underground. The main reason to go underground is to reduce the Newtonian noise contribution and to be able to better subtract the remaining one. The lower underground seismic noise, on the other hand, significantly reduces the control strategy problem. It has been assumed the underground seismic spectrum to be about $5 \cdot 10^{-9} m/f^2$ for $f > 1Hz$ which corresponds roughly to the seismic level measured in the Japanese Kamioka mine. This is assumed to reduce both the seismic noise as well as the gravity gradient noise by a factor of 20.

7. Even when going underground the gravity gradient noise seems still to be above the ET target sensitivity for frequencies below 6 Hz. Therefore it will be necessary to find some way to further reduce this noise by another factor 50 to finally get it below the ET sensitivity target. This is the only aspect of the analysis which cannot be achieved with "conventional" technologies.

8. Finally, in order to bring the radiation pressure below the ET design target, the weight of the mirrors has been increased from 42 kg to 120 kg.

The final result of this analysis is shown in fig.3.3, while fig.3.4 shows a summary of a possible choice of parameter to transform an advanced detector into a new detector which achieves a sensitivity compatible with the ET design target. The major weaknesses of this sensitivity curve are the suspension thermal noise which has not been included in the analysis, as well as the gravity gradient noise for underground site that, so far, is only in a preliminary study.

The sensitivity curve of fig.3.3, however, represents only one approach to achieve the ET target sensitivity and there might be other possible scenarios to be considered, such as the "Xylophone Option". For various reason, for instance the high power versus low temperature conflict, it might be beneficial to split the detection band into several detectors. The xylophone idea has been originally suggested by Riccardo De Salvo [20] and consists in having multiple specialized detectors, each of them covering only a part of the detection band: all the detectors together will finally give the targeted sensitivity.
ET, perhaps, could be composed of at least two xylophone interferometers, as in fig.3.5, where the high frequency (HF) detector and the low frequency (LF) one have completely different features [21].
In this model the HF detector has high intracavity power (3MW), is kept at room temperature on a surface location, uses normal suspension and no gravity gradient noise is subtracted. The LF detector, instead, has low power (18kW), is kept at cryogenic temperatures in an underground site, uses 50m long suspensions and takes into account the gravity gradient noise.
A crucial question to be answered, when considering the different sensitivity configurations, regards the astrophysics potentialities of such an interferometer, that I will describe in the next section.

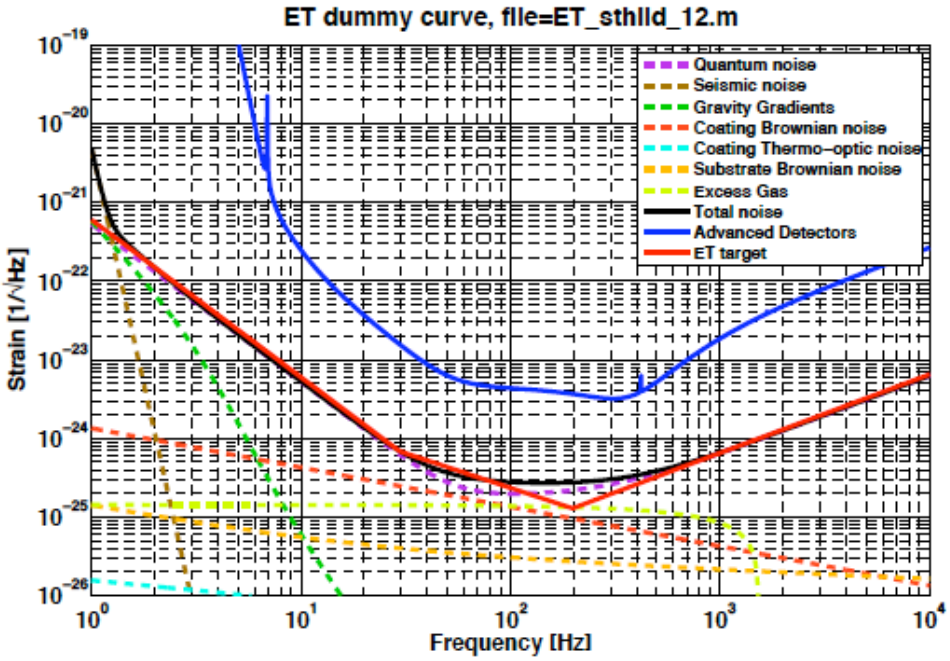

Figure 3.3: With the changes described above it is possible to achieve a sensitivity (black solid line) close to the ET design target (red solid line) [19].

	advanced detector	potential ET design
Arm length	3 km	10 km
SR-phase	detuned (0.15)	tuned (0.0)
SR transmittance	11 %	10 %
Input power (after IMC)	125 W	500 W
Arm power	0.75 MW	3 MW
Quantum noise suppression	none	10 dB
Beam radius	6 cm	12 cm
Temperature	290 K	20 K
Vacuum	$1.2 \cdot 10^{-7}$ mbar	$5 \cdot 10^{-9}$ mbar
Suspension	Superattenuator	5 stages of each 10 m length
Seismic	$1 \cdot 10^{-7}\,\mathrm{m}/f^2$ for $f > 1$ Hz (Cascina)	$5 \cdot 10^{-9}\,\mathrm{m}/f^2$ for $f > 1$ Hz (Kamioka)
Gravity gradient reduction	none	factor 50 required (cave shaping)
Mirror masses	42 kg	120 kg
BNS range	150 Mpc	2530 Mpc
BBH range	800 Mpc	17500 Mpc

Figure 3.4: Summary of the parameter changes necessary to go from the advanced detector sensitivity to the ET design target. Table from [19].

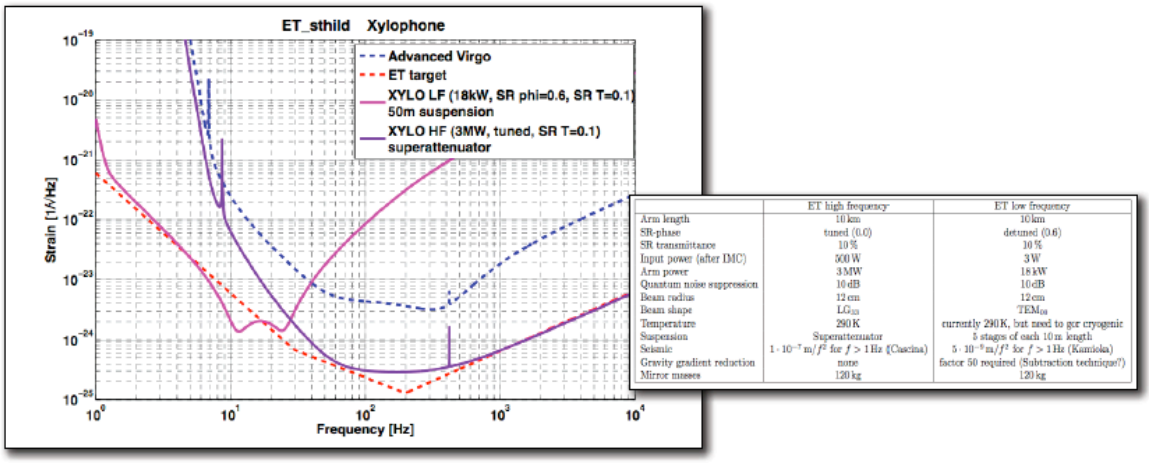

Figure 3.5: ET sensitivity curve reached by using a two detector xylophone configuration [21].

3.3 ET astrophysics issues

The sensitivity of an interferometric detector to astronomical and cosmological sources of gravitational waves crucially depends on several factors. As described in the previous sections, this Design Study will consider different options for the location of the interferometers, their topological, seismic and optical configurations. Each of these options will impact the science potential. The work package WP4 will consider in detail the quality and quantity of science afforded by the different choices. The strategy is to begin with a white paper on the science potential of the 'best' possible detector that could be constructed by pushing all technologies to their fundamental limits. WG4 will set forth key science requirements to be met by a third generation detector, the examples of which include [22]:

- studying cores of compact objects and general relativistic instabilities
- solving the enigma of gamma-ray bursts and resolving their different classes
- understanding the mass-spectrum of compact stars and their populations (neutron stars, strange stars, etc.)

ET is planned as a broadband detector, with good sensitivity over the frequency range from 1 Hz to 10.000 Hz, which promises many interesting

classes of sources. Binary neutron stars (NS) will sweep through the detector band from 1 Hz to 4 kHz, the signal lasting for several days as the system inspirals to a catastrophic merger event. Binary black hole (BH) mergers will also last for several hours, up to a day, in the detection band of ET. It could be possible also to follow the final stage of the merger process, thus opening the era of GW spectroscopy. The detector model sensitivity discussed in the previous section gives an inspiral range for binary neutron stars of about 2,5Gpc and of about 18Gpc for binary black hole systems. ET will be able to observe binary inspirals with SNR's of 100's about once each year: the higher harmonics that are present in the waveform will reveal the nature of the space-time geometry in strong gravitational fields (as it results when compact stars merge) and will help us answer fundamental questions about the end-product of a gravitational collapse. One of the most important challenge of ET is to understand the origin of gamma-ray bursts (GRB), confirming or ruling out the association of binaries of NS-NS/BH to GRBs and systematically studying different classes of gamma-ray burst sources.

Let us now describe in some detail the scientific motivation for probing the frequency band between 1 and 10 Hz, that is the band of major sensitivity improvement with respect to the advanced detectors. Stochastic gravitational wave background (SGWB), inspiral events, intermediate mass black holes (IMBH) and continuous waves from pulsars are believed to be the main sources of gravitational waves in this 1-10 Hz band [15].

The SGWB is expected to arise from a superposition of a large number of unresolved sources, located at different positions on the sky, and having different polarizations. It is usually described in terms of the GW spectrum:

$$\Omega_{GW}(f) = \frac{f}{\rho_c}\frac{d\rho_{GW}}{df} \tag{3.1}$$

where ρ_{GW} is the energy density of GWs at the frequency f and ρ_c is the critical energy density of the universe. The corresponding strain power spectrum is:

$$S_{GW} = \frac{3H_0^2}{10\pi^2}\frac{\Omega_{GW}(f)}{f^3} \tag{3.2}$$

Due to the f^{-3} factor in eq.(3.2), a third generation detector operating at or around 1 Hz (as opposed, for instance, to the 10-7000 Hz band

of Advanced LIGO) has at least 10^3 times better sensitivity to Ω_{GW} than the second generation detectors. This improvement would be sufficient to probe some of the most interesting cosmological models of SGWB. Moreover, known astrophysical sources of SGWB are significant either above the 0.1-10 Hz range (magnetars,Supernovae etc) or below this range (white dwarf binaries). Hence, this frequency band, or the 1-10 Hz range, offers the possibility of making a clean measurement of the cosmological models of SGWB. This would be a unique opportunity to directly probe the evolution of the Universe when it was less than 1 minute old, and to study the physics of the correspondingly high energy scale, which is not accessible to accelerator-based experiments.

The coalescence of two compact objects, on the other hand, is expected to be one of the most common sources for GW detectors. The coalescence event can be separated into three phases: inspiral, merger, and ringdown, as already illustrated in fig.1.5. The inspiral phase is characterized by an increasing frequency and amplitude (eq.(1.23)) as the binary loses energy to GWs and the orbit shrinks; the highest frequency of the inspiral is reached at the last stable orbit of the binary, approximately:

$$f = \frac{c^3}{6\sqrt{6}GM_{tot}}\ 4.4kHz \times (\frac{M_\odot}{M_{tot}}) \tag{3.3}$$

where M_{tot} is the total mass of the binary. The merger phase is very rapid with a smooth transition to the ringdown phase. Generally, the greatest strain amplitudes are found during the merger phase. The ringdown phase produces exponentially damped sinusoidal GWs as the newly formed black hole radiates away its perturbations and settles to a Kerr black hole with the dominant mode for emission being the quadrupole mode. For binaries up to $100M_\odot$, the merger and ringdown frequencies are in the LIGO-VIRGO or Advanced detectors band, but for intermediate mass black holes (IMBH), with total mass in the range $10^2 - 10^4 M_\odot$, both the merger and the ringdown frequencies are in the 0.1-10 Hz band, as in fig.3.6.

The capture of stellar mass compact objects by these IMBHs will produce signals in the 1-10 Hz region [23]. The mechanism for formation and growth of IMBHs is currently not understood, and several different scenarios have been proposed [24], with different consequences for the type of GW signals expected. In some scenarios, the IMBH forms from a direct, failed supernova collapse, while in other cases the IMBH is gradually built up through

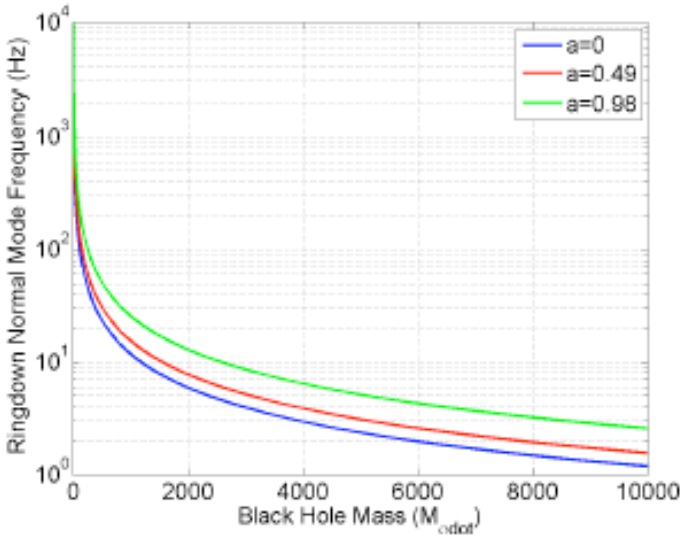

Figure 3.6: Frequency of the dominant ringdown mode of a compact binary coalescence as a function of the total binary mass. The parameter a is the dimensionless spin factor of the black hole. Picture from [15].

accretion and merger of stellar mass objects. Some ultra-luminous X-ray sources may be evidence of accreting IMBHs [25]. These cases can be distinguished by the existence (or non-existence) of an inspiral phase prior to the ringdown phase. Lower frequency sensitivity increases both the range to potential sources as well as improved ability to distinguish between these two scenarios. The 1-10 Hz band is also useful for studying lower mass binaries. Much of the angular position information of the binary is obtained through the inspiral phase. Consequently, going to lower frequency will allow for the better determination of the sky location of potential candidate sources.

Finally let us discuss the detection problem of continuous waves emitted from pulsars. As already explained in section 1.2, any deviation from axisymmetry in pulsars will produce continuous GWs with a frequency which is twice the pulsar spin frequency (eq.(1.10)). In general, the signal from these sources is quite weak, but the power in the signal can be built up through long-term observations of specific objects. The GW amplitude scales as $\epsilon\Omega^2/r$, see eq.(1.12), where ϵ is the deviation from axisymmetry and r is

the distance to the pulsar. This would appear to strongly favor high frequency pulsars, but the situation is more complicated. Fig.3.7 shows the distribution of the periods of known pulsars [26]: there are over 1100 pulsars that would produce GWs in the band from 1-10 Hz, compared to only 150 in the 100-1000 Hz band. Moreover, the evolutionary history of high and low frequency pulsars is believed to be rather different. Millisecond pulsars are believed to be the product of accretion onto a neutron star in a binary system, and they have significantly lower magnetic fields than the typical low frequency pulsar. Although a precise mechanism for maintaining a deviation from axisymmetry is not known, it is reasonable to speculate that large ϵ may be correlated with high magnetic field and thus lower frequencies. If detected, GWs could provide information about the equation of state of neutron stars. Precise phasing measurements may shed light upon the pulse emission mechanism by observing a phase difference between the GW signal and the pulse.

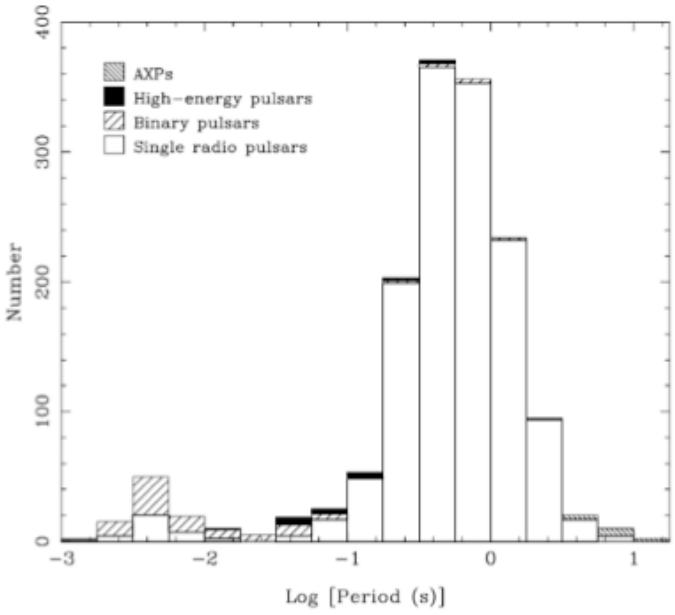

Figure 3.7: Histogram of periods of known pulsars. Data from the ATNF pulsar catalogue [26].

3.4 Detecting GWs from pulsars with ET

The most interesting frequency range, as explained above, to investigate about gravitational radiation emitted from pulsars is the 1 to 10 Hz band; third generation detectors, such as ET, seem to be the answer in this sense. I will discuss here the ET potentialities in detecting gravitational signals from pulsars, by using the sensitivity curve of fig.3.3 [19] (note that the analysis can easily be extended to different sensitivity configurations, such as the Xylophone one). We want to detect a signal with a signal-to-noise-ratio threshold of $S/N \geqslant 8$, which is an accepted value typically used in the GW community. Starting with the definition of S/N [24][27]:

$$\sigma^2 = (S/N)^2 = 4 \int_0^\infty \frac{\left|\tilde{h}(f)\right|^2}{S_n(f)} df \tag{3.4}$$

where $\tilde{h}(f)$ is the Fourier transform of the signal $h(t)$ and $S_n(f)$ is the noise power spectral density of the detector, i.e. the square of its sensitivity curve, we note that the power in the gravitational wave signal from a pulsar is concentrated at one frequency, f_1, which is twice the rotating frequency of the star f_0. It is therefore possible to consider the power spectral density of the noise to be a constant value through the integral. We get:

$$\sigma^2 \simeq \frac{4 \int_0^\infty \left|\tilde{h}(f)\right|^2 df}{S_n(f_1)} \tag{3.5}$$

It is convenient now to estimate σ^2 using the Parseval's theorem [27], which states that the total power of a signal calculated in the frequency domain must be the same as the total power calculated in the time domain, both of them representing the energy spectral density of the signal. Specifically, the Parseval's theorem is expressed as:

$$\int_{-\infty}^{\infty} |x(t)|^2 \, dt = \int_{-\infty}^{\infty} |X(f)|^2 \, df \tag{3.6}$$

where $X(f)$ is the Fourier transform of $x(t)$. Thus:

$$\sigma^2 = \frac{4}{S_n(f_1)} \int_0^\infty \left|\tilde{h}(f)\right|^2 df = \frac{4}{S_n(f_1)} \int_{-\infty}^{\infty} \left|\tilde{h}(f)\right|^2 df = \frac{4}{S_n(f_1)} \int_{-\infty}^{\infty} |h(t)|^2 \, dt \tag{3.7}$$

Being the waveform from a pulsar monochromatic and the observation time not infinite, we get:

$$\sigma^2 = \frac{4}{S_n(f_1)} \int_0^{T_{\rm obs}} h^2(f_1) dt \tag{3.8}$$

Finally, setting $S/N \geqslant 8$, or $\sigma^2 \geqslant 64$, we obtain:

$$\sigma^2 = \frac{4h^2(f_1)T_{\rm obs}}{S_n(f_1)} \geqslant 64 \tag{3.9}$$

To evaluate this quantity I've chosen an observation time of one 'sidereal year' = 31,558,149.540 s and the standard values $I_3 = 10^{38} Kgm^2$ and $\epsilon = 10^{-7}$ for typical pulsar, to be inserted into the constant component of eq.(1.11), which reads:

$$h(f_1) = \frac{G(2\pi)^2 f_1^2 I_3 \epsilon}{c^4 r} = \frac{4G(2\pi)^2 f_0^2 I_3 \epsilon}{c^4 r} \tag{3.10}$$

The sensitivity curve of ET, $S_n^{1/2}(f)$, has been reconstructed and evaluated at different frequencies following the model of fig.3.3 and the only free parameter, after inserting eq.(3.10) in eq.(3.9), is the maximum observation distance r. This distance has been calculated in the ET sensitivity frequency range, between 1 and 10,000 Hz (which corresponds to the pulsar spinning frequency band 0.5 to 5,000 Hz), as follows:

$$r \leqslant 2.96 \cdot 10^{-7} Kpc \left(\frac{I_3}{10^{38} Kgm^2}\right) \left(\frac{\epsilon}{10^{-7}}\right) \left(\frac{T_{obs}}{1yrs}\right)^{1/2} \left(\frac{f_0}{0.5Hz}\right)^2 \left(\frac{5 \cdot 10^{-22} s^{1/2}}{S_n^{1/2}(f_1)}\right)$$

Thus, for each pulsar spinning frequency f_0, ET can observe gravitational signals from pulsars coming from a distance less or equal to the value r. It is clear that the calculation above is only an approximation, being the sensitivity curve and the ellipticity still uncertain; it is significant, however, to show how the maximum observation distance changes as a function of the ellipticity ϵ. In fig.3.8 I've plotted the maximum distance achievable with the ET sensitivity target (shown in red in fig.3.3) versus the pulsar spinning frequency, as a function of the theoretical constraint on ϵ, which are typical stronger than the observational ones (see discussion in section 1.2). The ellipticity of the star has been varied between 10^{-6} and 10^{-9}, as in fig.3.8.

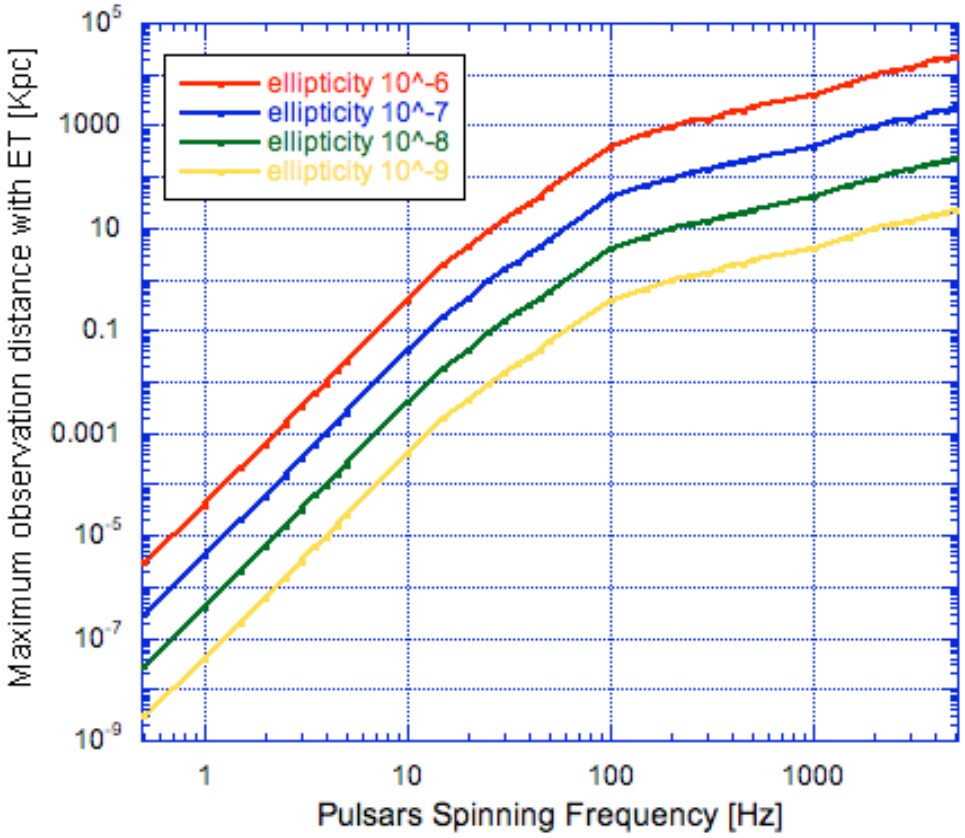

Figure 3.8: Limit distance, in Kpc, at which it is possible to detect gravitational signals from pulsars, as a function of the ellipticity of the stars, for one year observation at the ET nominal sensitivity.

An inspection at the distribution of the known pulsars in the sky, shown in fig.3.9 (data taken from the "Australia Telescope National Facility" pulsar catalogue, that includes all the pulsars presently discovered), allowed me to evaluate how many pulsar sources could be found with ET.

By overlapping fig.3.9 and fig.3.8 we can see a comparison, fig.3.10, between the maximum distance, in detecting GWs from pulsars, achievable with ET and the distance of the known pulsars: all the stars as far as the maximum ET distance curves can theoretically be detected. It is easy to see

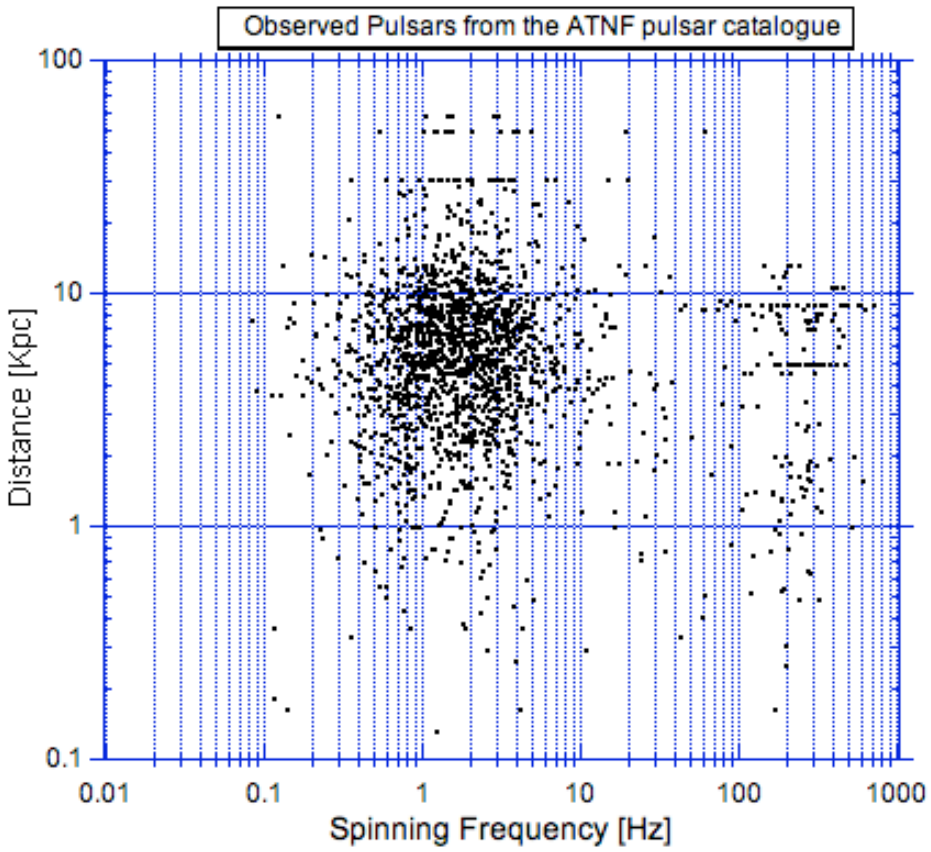

Figure 3.9: Distance of known pulsars versus spinning frequency.

that at 1 Hz, even with the best curve obtained for $\epsilon = 10^{-6}$, the distance of the discovered pulsars is four order of magnitude larger than the maximum distance reachable by ET: at that frequency the target sensitivity of ET is not good enough to detect gravitational signals from pulsars. The result at 10 Hz is much more interesting: with an ellipticity of 10^{-6} ET can observe as far as 400 pc for standard pulsar parameters. Although at that frequency there are very few pulsars within the ET distance range, not every pulsar has been discovered yet. In our galaxy thousands of neutron stars should exist and, until now, only a fraction of them has been found as pulsars. Pulsars, in fact, are highly magnetized, rotating neutron stars that emit a beam of

electromagnetic radiation, mostly in the radio wavelength. Only recently some pulsars have been found to emit also in the X-ray and gamma ray wavelength [28].The electromagnetic radiation can only be observed when the beam of emission is pointing towards the Earth and, since some pulsars are not beaming towards us, they cannot be found in this way. Finally, some neutron stars are not pulsars, but they could still be gravitational wave sources if there were some ellipticity. It is very likely that unobserved neutron stars spinning at 10 Hz will be within the range of ET, and that they could be detected thanks to their gravitational waves emission. To conclude, let us say that the sensitivity in detecting known pulsars increases at frequency higher than 10 Hz and, for the best curve obtainable with $\epsilon = 10^{-6}$, as many as $\sim$180 out of the total of $\sim$1770 visible pulsars can be observed with ET as gravitational waves sources. The detection of GWs from known as well as unknown pulsars will finally set a limit on their ellipticity and help having a better understanding on their equation of state.

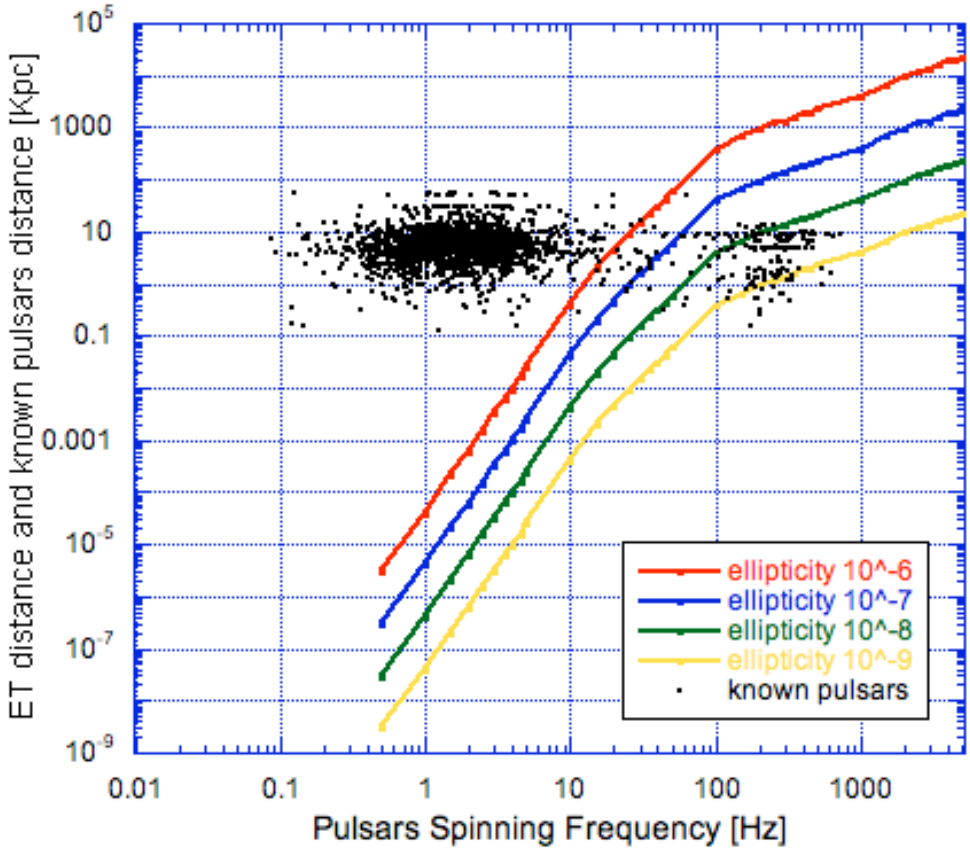

Figure 3.10: ET maximum observation range of GWs from pulsars and distance of known pulsars.

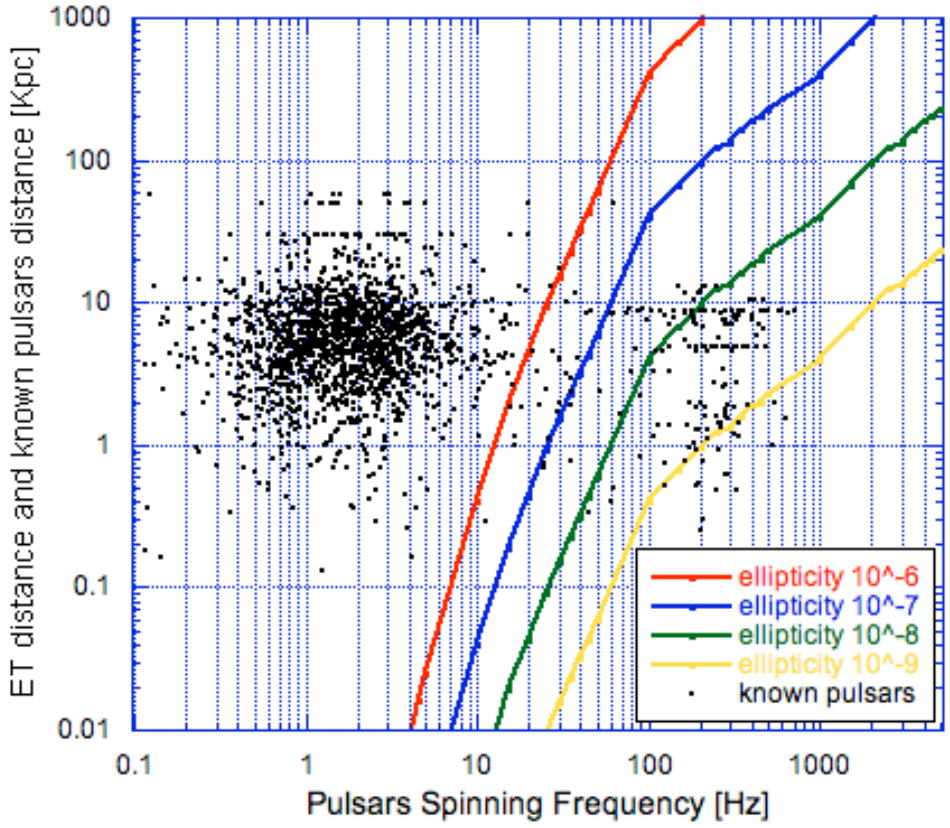

Figure 3.11: Zoom-in of fig.3.10 in the frequency range 0.1 to 5000 Hz. All the pulsars at the right side of each solid line can theoretically be detected with ET.

Chapter 4

Low frequency noise in Maraging blades

4.1 Abstract

From what we have seen about third generation gravitational waves detectors, is it clear that one of the major challenges is the reduction of the noise at low frequency, which is dominated by the seismic and the gravity gradient one: the seismic isolation thus plays a fundamental role in the improvement of the low frequency band sensitivity of these interferometers. All seismic isolation systems developed for gravitational waves interferometric detectors, such as LIGO, VIRGO and TAMA, make use of Maraging steel blades, a precipitation hardened alloy that allows the production of creep-free blade springs. Although these springs provide exceptional attenuation performance at high frequency (>1 Hz), anomalies were observed at lower frequency. The dissipation properties of these blades have been studied at low frequencies, using a Geometric Anti Spring (GAS) filter, which, together with the Electro Magnetic Anti Spring (EMAS) mechanism, allowed the exploration of resonant frequencies below 100 mHz. At this frequency an anomalous transfer function has been observed in the GAS filter: this is one of the several motivations for starting this research. The many unexpected effects observed and measured are explainable by the collective movement of dislocations inside the material, described with the statistic of the Self Organized Criticality (SOC). These dislocations are normally entangled in a precipitation hardened alloy, which is our case, but can disentangle under applied stress. It is well known

that dislocations carry stress and contribute to elasticity. At low frequencies, below 200 mHz, processes compatible with dislocation disentanglement are observed, resulting in anomalous dissipation mechanisms, hysteresis, reduced elasticity in the system, and non-predictive variations of the GAS filter equilibrium point. All of these fenomena are explainable in terms of slow dislocation "avalanches". At higher frequencies the anomalous behavior is not evident, which could be explained with the fact that the applied stress may be too fast to allow the full growth of dislocation "avalanches". As a result a more predictive behavior and less losses are observed, thus explaining the higher Q-factor in this frequency range. Although some of the effects studied in this thesis have been previously observed, the proposed explanation here is to connect all of them to the same underlying process, which is collective dislocations movement. Thanks to the knowledge gained during this research, it is immediate to think about choosing new materials and shapes for the realization of seismic attenuation filters in GW detectors, in order to avoid the problems encountered with the Maraging blades at low frequency.
This chapter is the result of my thesis work at the California Institute of Technology: I will discuss here the theoretical model which best explains our experimental findings, the mechanical filter that we used, the experimental procedure, the data analysis and the results obtained. Finally, I will give an overview about the future plans in this field.

4.2 Geometric Anti Spring (GAS) filter

With few exceptions, all seismic attenuation systems for gravitational waves interferometric detectors are passive attenuators, based on harmonic oscillators with resonant frequencies below the frequency region of interest: these consist of common pendula or Inverted Pendula (IP) for isolation in the horizontal direction, and soft springs for the vertical direction. The most common vertical springs are cantilever blade springs (the only exception being LIGO, which uses helical springs). The spring softness is inversely proportional to the pre-stressing length, and limited by the blade's size. Some cantilever blades are softened by different anti-spring configurations, magnetic or geometric. The apparatus used in our experiment is the so called Geometric Anti Spring filter [29], which is basically a second order passive mechanical filter. The GAS filter consists of a set of radially arranged cantilever blades, each about $38cm$ in lenght, clamped at the base to a common frame ring

and opposing each other via a central disk. In our case, we used the Monolithic GAS filter [30], in which both the three blades and the central disk are a monolithic piece machined from a flat sheet of Maraging steel [31]. The blades are loaded with a 65 Kg payload, curved as in fig.4.1 and secured at 45° to the filter frame:

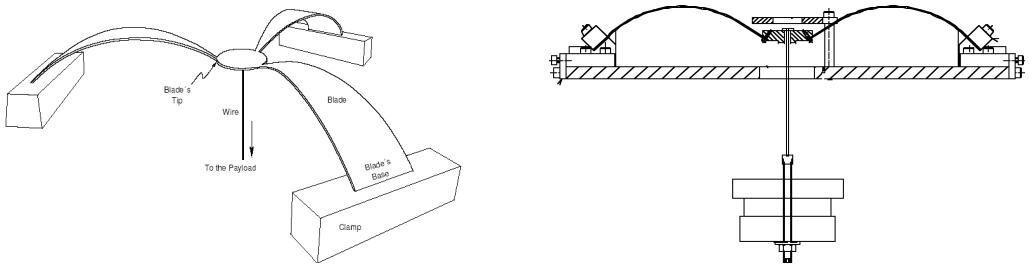

Figure 4.1: Schematic of a GAS filter: perspective (left) and side view (right). Three flat blades are pre-stressed and mounted face to face against a keystone which suspends the payload. The radial compression of the blades, governing the Geometric Anti Spring mechanism, is obtained by micrometrically pushing on the blade clamps with tuning screws.

The choice of the material is made to obtain a high loading factor without creep and with a good thermal stability. The 3.44 mm thick blades are composed of Maraging Marval-18 precipitation hardened at 435° C for 100 hours. A model of the GAS mechanism is sketched in fig.4.2, in which the payload is suspended by a vertical spring of elastic constant k_z and rest length l_{0z} and by two horizontal springs of elastic constant k_x and rest length l_{ox}. The equation of motion for the system is [32]:

$$m\ddot{z} = k_z(z_{eq} - z - l_{0z}) - k_x(l_x - l_{0x})\sin\theta - mg \tag{4.1}$$

where $l_x = \sqrt{x_0^2 + z^2}$ is the length of the horizontal spring and z_{eq} is the elongation of the vertical spring corresponding to $\theta = 0$. Approximating $\sin\theta$ to z/x_0 for small angles, eq.(4.1) reduces to

$$m\ddot{z} = k_z(z_{eq} - z - l_{0z}) - k_x(1 - \frac{l_{0x}}{x_0})z - mg \tag{4.2}$$

and at the first order the system has an effective spring constant

$$k_{eff} = k_z + k_x - \frac{k_x l_{0x}}{x_0} \tag{4.3}$$

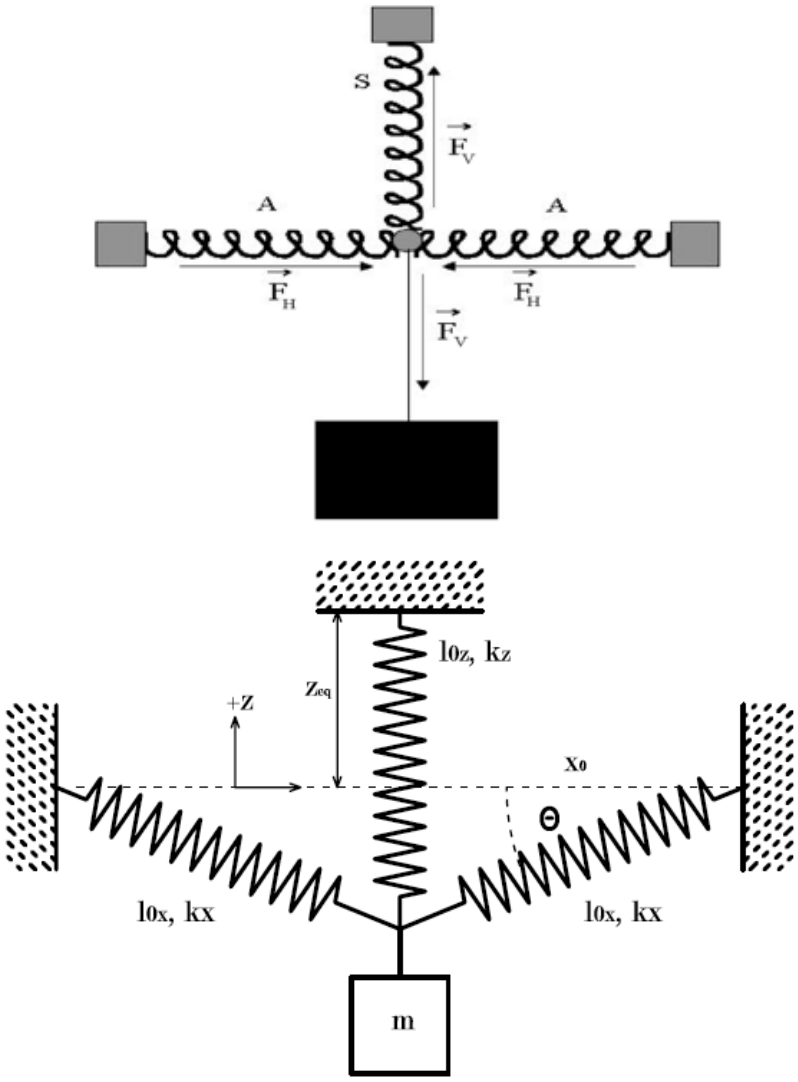

Figure 4.2: GAS model. At the working point (top sketch) the vertical spring S supports the weight of the payload. The two opposite springs A are compressed, and their forces cancel. Moving out of the working point (bottom sketch, courtesy of A. Stochino) the opposing forces of the A springs do not cancel completely, generating a vertical component proportional to the displacement from the working point, the so-called Anti-Spring force.

The last term of eq.(4.3) is the Geometric Anti-Spring contribution, that introduces a negative spring constant into the system: the effective stiffness is thus reduced, and so the resonant frequency, just by compressing the horizontal springs. The radial compression of the blades can be changed by means of radial screws, and the resonant frequency ω_0 of the system can be lowered. The theoretical transfer function of this filter is:

$$H_z(\omega) = \frac{\omega_0^2(1+i\phi)+\beta\omega^2}{\omega_0^2(1+i\phi)+i\gamma\omega-\omega^2} \tag{4.4}$$

where ω_0 is the resonant peak frequency, γ is an appropriate viscosity term that, together with the loss angle ϕ, determines the peak width, and β is a mass term which accounts for the inertia of the blades and provides the saturation level of the transfer function at high frequencies. Between the resonant frequency and the plateau given by the distributed mass of the blades, the filter transfer function is expected to scale as $1/\omega^2$: in this way it is possible to achieve a large seismic isolation above ω_0.

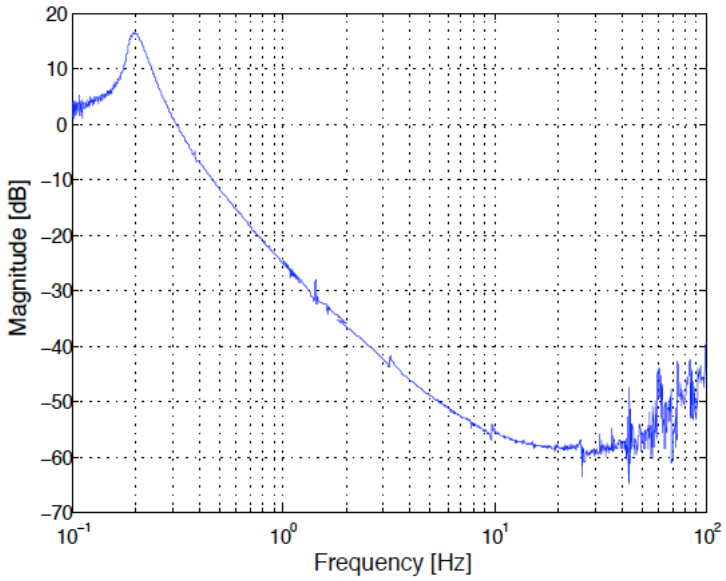

Figure 4.3: GAS filter transfer function, courtesy of A.Stochino. For frequencies higher than the resonant peak the slope is $1/\omega^2$. The attenuation saturates at -60 dB.

In our experiment the GAS mechanism is used to null up 95 to 96% of the spring restoring force near the filter working point, in order to study the dissipation properties of the Maraging blades at very low frequency. In order to lower even more the resonant frequency of the filter, the Electro Magnetic Anti Spring (EMAS) mechanism [35] has been implemented, which I will discuss in the next section. In this sense, being the restoring force of the spring almost completely nulled thanks to the GAS and EMAS mechanisms, we can use our filter as a microscope to explore the dissipation dynamics that occurs inside the Maraging blades.

4.3 Experimental setup

The GAS filter has been tuned at low mechanical resonant frequency, typically 200 mHz (in this experiment 220 mHz and 240 mHz tunes have been used). The experiment has been performed in a sub-basement laboratory at Caltech, where the main sources of perturbations were due to turbulent air currents and thermal cycles from the air conditioning system. For this reason a rigid box was built around the GAS filter, made of 2.5 cm thick polystyrene foam panels, which reduced the thermal fluctuations to less than a degree centigrade and deflected most air conditioning wind. However, since the thermal drift of the filter is of the order of one $mm/^{\circ}C$, while the measured effects can be on a submicron scale, an active thermal compensation was introduced. This feedback keeps the filter at its optimal working point, which corresponds to the height where the Anti Spring effect is maximized and the restoring force of the springs is minimized. For this task an Infinite Impulse Response (IIR) feedback integrator continuously calculates the displacement of the filter from its working point, integrates it and feeds it to a vertical actuator. The actuator [33] is a voice coil mounted coaxial to the load suspension wire, driven by a computer generated control signal and acting on the payload from the filter support. Similarly mounted, see fig.4.4, a Linear Variable Differential Transformer position sensor [34] was used to acquire the filter displacement signal. The LVDT calibration, 1.28 ± 0.01 V/mm, was performed by imposing a sequence of readout voltages (via the integrator feedback) and reading the blades height with the help of a web camera and a ruler. The actuator calibration, 26.3 ± 0.3 mN/V, was performed by adding and/or subtracting known masses and noting the current required by the feedback to return the system to the optimal working point.

Care was taken to repeat these measurements in opposite directions to eliminate the thermal and hysteresis systematic effects. In both calibrations the error was estimated from the dispersion of data points around the fits.

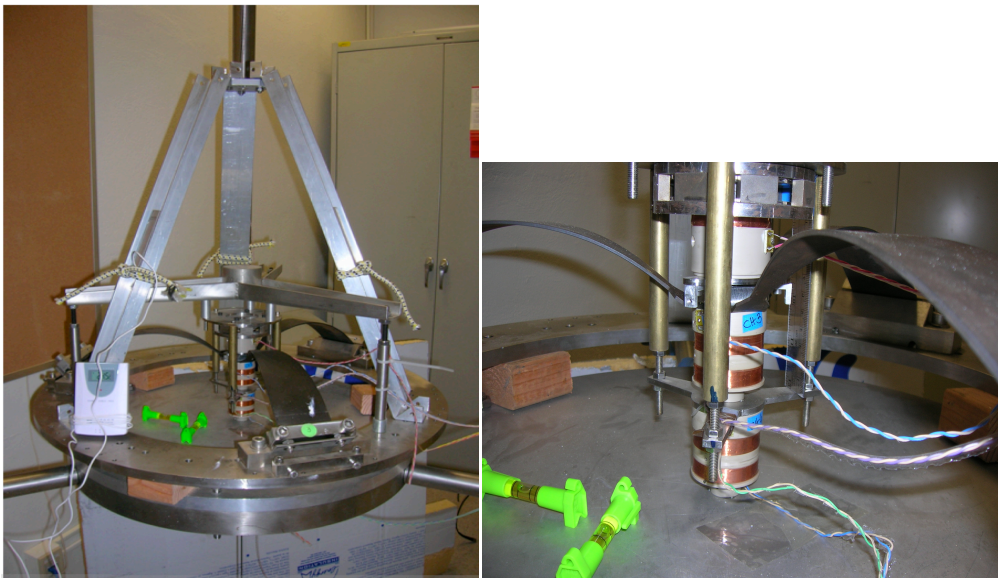

Figure 4.4: Left panel, the GAS filter used in this experiment, mounted on a rigid support. Right panel, zoom-in of the LVDT sensors (two bottom coils, only one of the two LVDTs shown is used in this experiment) and of the actuator (top coil).

The GAS mechanism is optimized at the height where the radial compression of the blades is maximized. To determine the optimal working point we used the actuator to apply a progression of fixed vertical forces (or constant currents) to explore the vertical movement. These currents were simply obtained requiring different set points to the IIR filter; at each height we applied a short force pulse to excite the spring, recorded the ringdown, and fit it to find the corresponding resonant frequency. We finally plotted the resonance frequencies versus the vertical height and looked for the minimal resonant frequency, which is thereafter defined as the filter's working point. The ringdown at each position was fitted over several oscillations with the damped sinusoid function:

$$h + Ae^{-\frac{t-t_0}{\tau}} \sin(2\pi f(t-t_0)) \tag{4.5}$$

where h is the oscillation mean height, A its amplitude, f the oscillation frequency, t_0 a phase taking into account the fit startup time, and τ the decay lifetime as in fig.4.5.

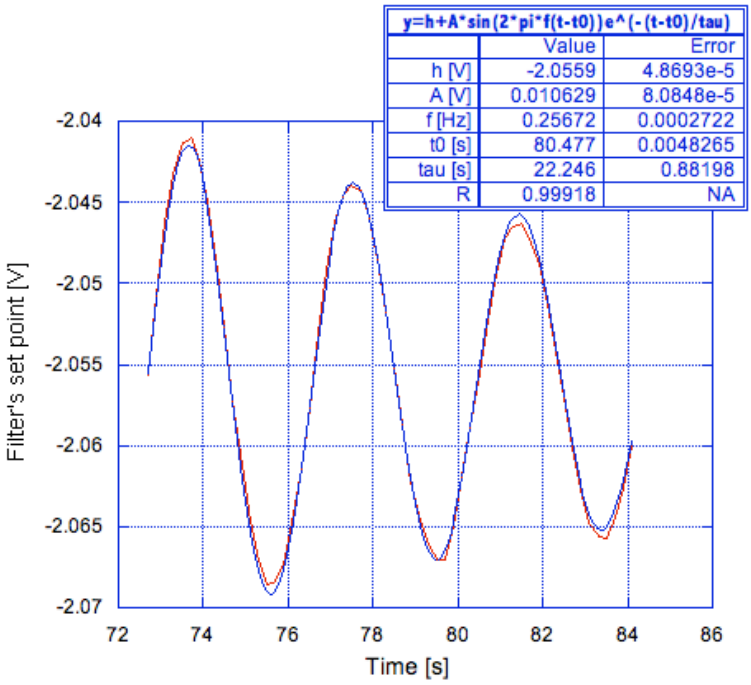

Figure 4.5: The ringdown (red line) has been fitted with eq.(4.5) *to find the filter resonant frequency f, its height h and its lifetime τ. In this example the filter oscillates around a set point of -2 V, imposed via the IIR integrator.*

We performed the position scan in both directions, fig.4.6, and applied the fitting procedure to data chosen to have the same initial oscillation amplitude. The up and down scan yielded a small difference ($\sim$ 1mHz) in the optimal resonant frequency of the parabola and ($\sim$ 0.06mm) in the corresponding height; we took the mean of the two measurements.

From this point on, we always kept the filter at its working point, which corresponds to the minimum of the parabola, acting through the feedback integrator. This was done with a slow integration time constant, typically 100 s. As previously mentioned, to further reduce the filter restoring force and resonant frequency, an Electro Magnetic Anti Spring (EMAS) [35] with variable gain has been implemented: the LVDT signal, to which we subtract

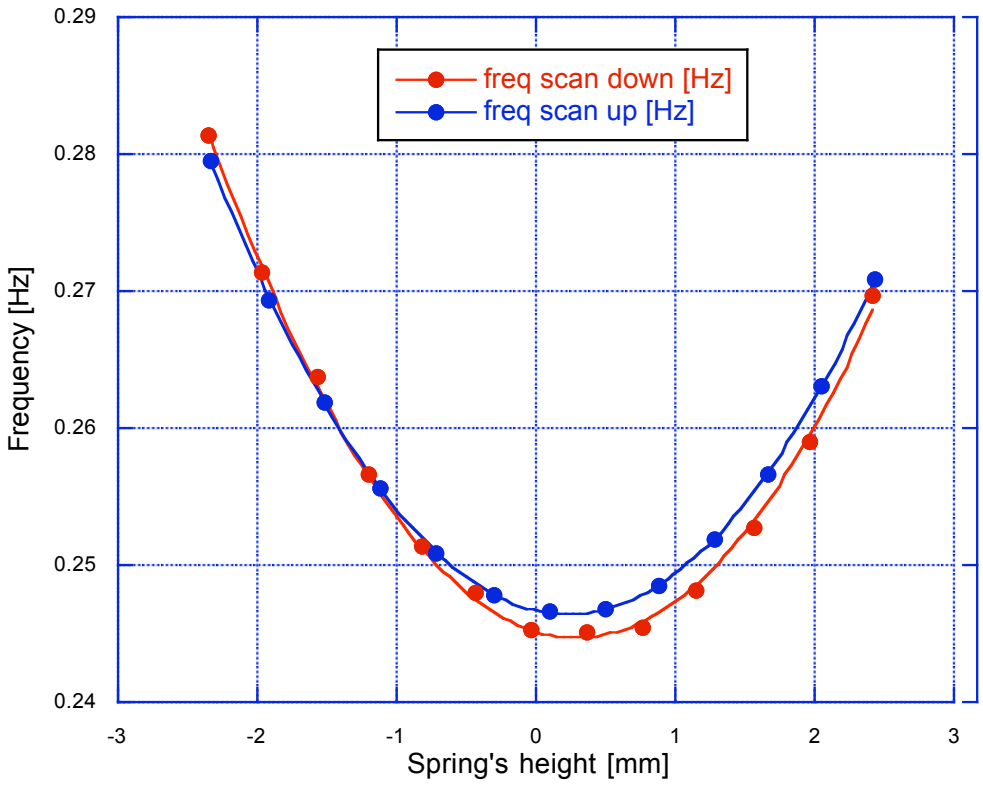

Figure 4.6: The spring is scanned around its best working point to find the minimum of the parabola, corresponding to the maximal GAS effect. The blue and the red curves correspond to two separate up- and down-scan measurements.

the set point in order to keep the filter at its working point, is multiplied for this EMAS variable gain and the resulting signal is sent to the actuator thus feeding it. A negative gain will introduce a negative spring constant K_{emas} into the system, to be added to the usual spring constant $K_0 = \omega^2 M$. The resonant frequency will be expressed as:

$$f = \frac{1}{2\pi}\sqrt{\frac{K_0 + K_{emas}}{M}} \tag{4.6}$$

where M is the 65 Kg payload mass, K_0 is determined by the mechanical filter's tune (K_0=155.96 N/m for 0.24 Hz GAS tune, K_0=127.15 N/m for 0.22 GAS tune) and K_{emas} is equal to the EMAS gain times a constant proportional to the actuator efficiency. The resonant frequency follows well the model of the previous equation, as illustrated in fig.4.7, whose corresponding mechanical tuning was 0.24 Hz.

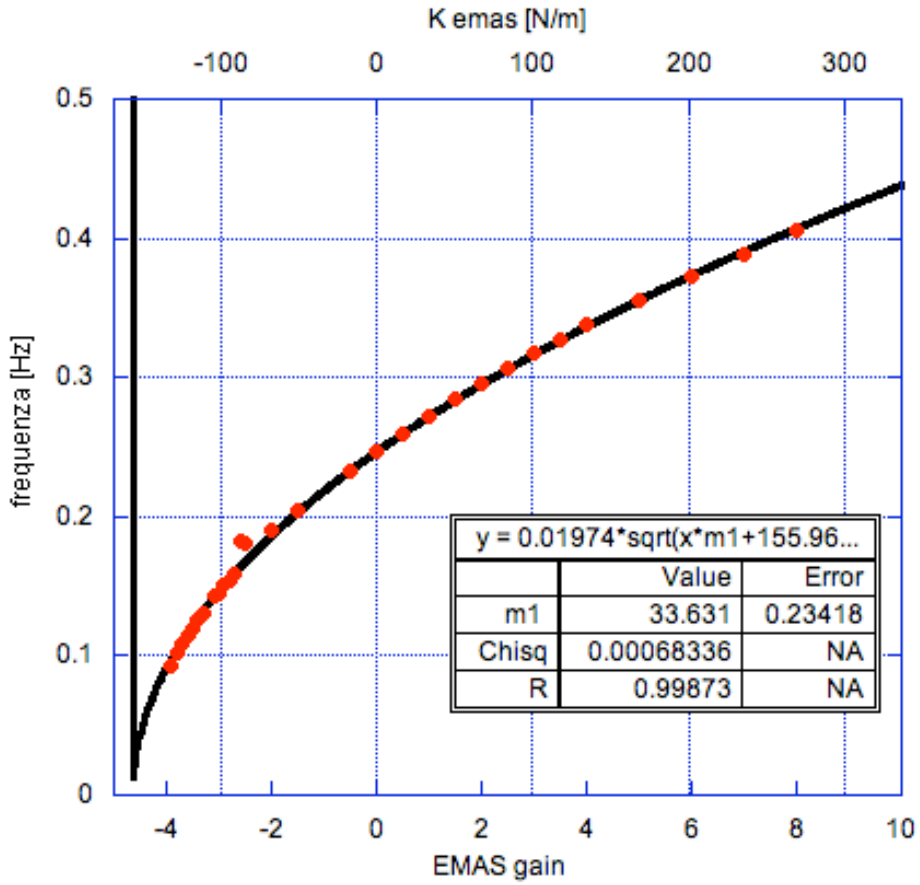

Figure 4.7: Filter resonant frequency versus EMAS gain and K_{emas}. The two points deviating from the fit at $\sim$ 0.17 Hz correspond to a payload resonance.

From the fit we found that K_{emas} is obtained from the EMAS gain times $33.6 N/m$. The EMAS mechanism is able to drive the oscillator all the way

to zero frequency or, with positive K_{emas}, to higher frequencies.
All the above functions are applied via an ad hoc Labview control program.

4.4 Motivations to this research

As shown in section 4.2, between the tuning dependent resonant frequency and the attenuation saturation frequency due to the distributed mass of the blades, the amplitude of the GAS filter transfer function is expected to drop as $1/f^{\alpha}$ with $\alpha = 2$. This $1/f^2$ slope is expected to simply slide to lower frequencies, following the shifting resonance. However, on tuning the system at very low frequencies, at or below 100 mHz, an anomalous $1/f$ transfer function with $\alpha = 1$ becomes experimentally detectable (fig.4.8) [36]. Such anomaly can not be explained by dissipative phenomena such as the thermoelastic effect which, for Maraging blades 3.44 mm thick and heat-diffusion coefficient $D_{th} = 5.5 \cdot 10^{-6} m^2 s^{-1}$, would peak at around 0.73 Hz, well outside the region of the GAS filter transfer function where the $1/f$ slope is observed.

The appearance of the 1/f term in the transfer function of the GAS filter was the initial motivation of our project. Further unexplained observations later appeared to be connected with this study and, totally or in part, clarified by our conclusions, namely:

- the hysteresis observed in GAS blades [37] and tilt hysteresis in Advanced LIGO mirror suspensions [38]
- the very low coherence between the four identical and co-located Virgo Inverted Pendula (IP) during storms
- the apparent random walk of the Virgo [39] and TAMA [40] IP equilibrium point
- the loss of predictability of the ringdown decay in the LIGO-SAS IP, as found in [37]
- the anomalous IP instability first reported in [41] and also observed in GAS filters and other IPs
- the failure of various tiltmeter designs to reach high sensitivity at low frequency

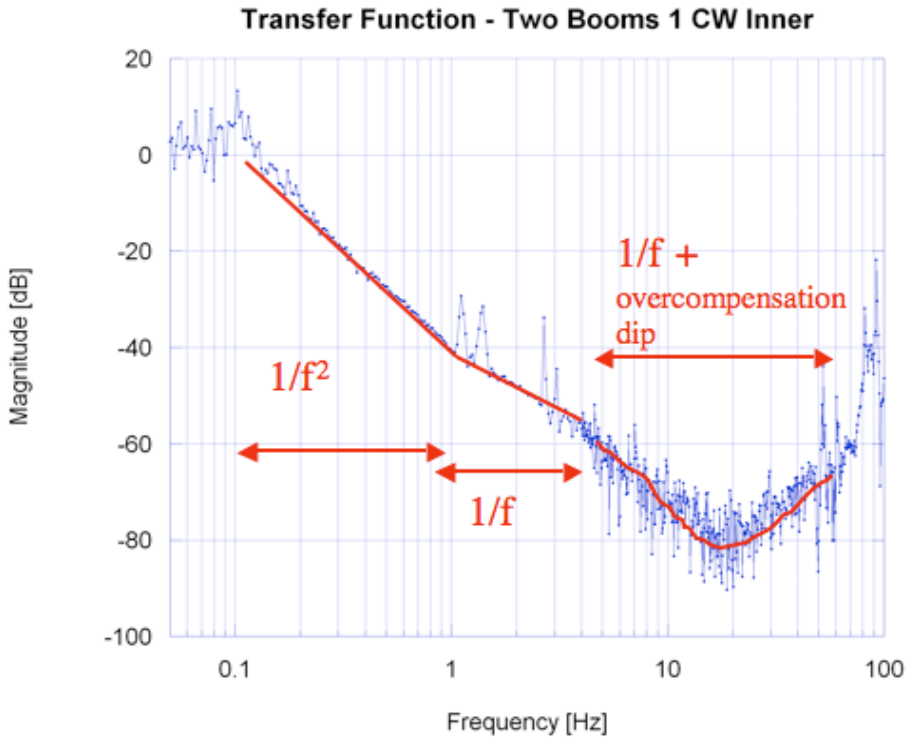

Figure 4.8: Anomalous $1/f$ slope above 1 Hz with the filter tuned at 100 mHz. The three peaks between 1 and 3 Hz are payload resonances. The dip below the $1/f$ slope is obtained with overcompensation of the blades mass term. Picture from [36].

- the long settling times required by seismometers and torsion pendulum gravimeters to reach high sensitivity after large excursion excitations

4.5 Theoretical models

Low frequency experiments, such as the one presented here, detect frequency independent losses and static hysteresis. Viscosity has been very successful in explaining dissipation properties of materials at higher frequencies, but, being proportional to speed, its effects vanish in the zero frequency limit and fails to explain static hysteresis. Hysteresis can be regarded as an effect of spatial disorder [42][43]: even the purest crystals contain a large amount

of point (impurities, vacancies) or linear defects (dislocations), and the observed equilibrium point of a macroscopic mechanical device, far from being uniquely defined, may then correspond to any of the infinitely many local minima of the disorder matrix, each with its statistical weight.
In materials science, a dislocation is a crystallographic defect, or irregularity, within a crystal structure and it is commonly accepted that mobile dislocations constitute an important dissipation source in metals [44]; until now dissipation was interpreted as the result of the incoherent sum of movements of individual dislocations. There are two main types of dislocation, edge and screw. Dislocations found in real materials typically are mixed, meaning that they have characteristics of both. Until the 1930s, one of the enduring challenges of materials science was to explain plasticity in microscopic terms. It has been realized later that plastic deformation could be explained in terms of the theory of dislocations [44]. Dislocations can move if the atoms from one of the surrounding planes break their bonds and rebond with the atoms at the terminating edge. In effect, a half plane of atoms is moved in response to shear stress by breaking and reforming a line of bonds, one (or a few) at a time.
In the context of the present investigation, the notion of losses controlled by collective motion of dislocations provides the most convincing interpretation of our experimental findings. In this chapter I will show how collective dislocation dynamics, such as avalanches of dislocations, must be considered to explain the observed properties, including static hysteresis and amplitude dependent losses, of very low frequency mechanical oscillators.
Metallurgy has many dislocation control methods, for example in work hardening dislocations are created in such large numbers that they entangle to the point that their motion is impeded and dissipation suppressed (the material acquires a higher Q-factor and larger elasticity modulus). The dislocation density increases due to the formation of new dislocations and dislocation multiplication induced by repeated plastic deformations. The consequent increasing overlap between the strain fields of adjacent dislocations gradually improve the resistance to further dislocation motion. These trapped dislocations substantially contribute to the mechanical properties of the material: in the presence of low amplitude harmonic stresses, dislocation segments remain pinned inside the crystal and vibrate like ideal elastic strings [45]. In a precipitation hardened alloy, that is the case of our Maraging blades, as well as in most polycrystalline metals, dislocations can entangle but are not numerous enough to fully interlock as in the case of work hardening, and

can disentangle under changing stresses. In Maraging, for example, the dislocation movement is impeded by the presence of intermetallic precipitates, essentially finite size point defects, impeding the large scale dislocation movement: the typical spacing of the precipitates in Maraging is tens of nm, i.e. large if compared with the atomic distances. A dislocation line defect may thus easily miss a point-like defect. Therefore, even in a precipitation hardened material, a dislocation can still move quite a ways before being stopped by a precipitate. Dislocations pin to impurities, precipitates, and other defects, but also to one another; interactions between each other can build up and be non linear. As they pile up they get trapped: a trapped dislocation needs to wait for neighboring ones to unpin before it can move again. Once it starts, the movement of a dislocation can engender domino effects spreading out from an initial point and sweeping through arbitrarily large volumes. Although vibrations of pinned dislocation segments may be extremely short lived, the domino effects involving large numbers of dislocations occur on substantially longer time scale. The observed effects we report here are in the time scale of seconds and involve up to the entire size of our flexures of ~ 38 cm. The description of the relaxation dynamics of a dislocation network is necessarily of a statistical type. A simple model, that closely interpreted our first observations and that was, therefore, adopted as a roadmap in our further investigations, is the so called Self-Organized Criticality (SOC) [46][47]. According to this theory, one can postulate that a certain fraction of the total dislocation network can rearrange according to self-organized patterns, scale-free in space and time, thus naturally explaining the residual internal friction at zero frequency (static hysteresis) and the ubiquitous 1/f noise [48] [49]. Combining SOC dislocation models with our measurements and observations, we propose the following overall picture. Entangled dislocations form a rigid lattice, which contributes to elasticity. Dislocations can be disentangled by mechanical oscillations, local stresses, or simply thermal fluctuations. If dislocations disentangle, in a domino effect, following a SOC statistics, the material elasticity is reduced; while disentangled, dislocations produce viscous-like effects. The eventual re-entanglement of dislocations in a different configuration can explain the observed static hysteresis, while the scale-free nature of such processes can explain the unexpected 1/f slope of the GAS transfer function, since this additional dissipation process contributes to raise it. Dislocation avalanches, finally, cannot contribute to internal friction at high frequencies because disentanglement is a slow process and, at frequencies higher than the characteristic avalanches growth times, they have

no time to build up, and much lower losses are observed. This thesis illustrates the experimental evidence in support to this theory.

4.6 Data acquisition, analysis and results

4.6.1 Thermal hysteresis

The filter position signal was acquired, through the LVDT, for several hours, without thermal feedback (the integrator was switched-off): a large amount of thermal hysteresis was observed in the filter movement, as shown in the left panel of fig.4.9. When switching on the feedback mechanism, which stabilized the filter working point to within a few micron, we expected no residual hysteresis. Instead a similar fractional level of thermal hysteresis has been found in the feedback current that feeds the actuator, right panel in fig.4.9. This observation clearly indicates that hysteresis does not originate from the GAS filter macroscopic movement, but rather from a microscopic dynamics inside the blades. A posteriori this effect is not surprising because the grains inside the material only see variations of internal stresses, and cannot distinguish between thermally and motion caused stresses. This simple insight, illustrates the importance of large dislocation movements under small, slow stress variations.

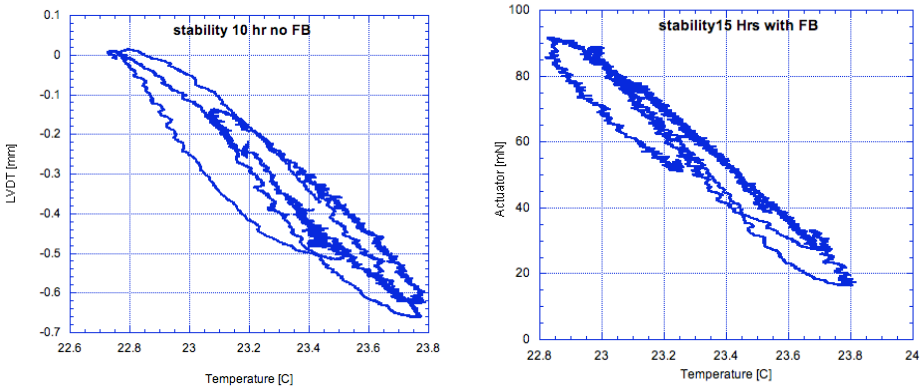

Figure 4.9: Thermal hysteresis of the filter movement subject to air conditioning thermal fluctuations without feedback (left) and variation of the control current with feedback (right). The data refer to a 10 hours and 15 hours acquisition respectively.

4.6.2 Hysteresis versus GAS filter frequency tune

In order to explore the effects of hysteresis at different filter tunes, excitations of various amplitudes and shapes have been applied through the actuator. The measurements have been repeated with alternate sign excitations to cancel thermal drift effects. A thermal feedback time constant much longer than the experiment time scale was used. The measurements were performed at different filter frequency tunes. With an EMAS spring constant K_{emas}=0 N/m and K_0=127.15 N/m, which, according to (4.6), corresponds to a resonant frequency of 220 mHz, we applied a force to the system, then slowly (slower than the oscillation frequency) returned it to zero: we observed hysteresis in the GAS filter displacement, only for alternated sign excitations (fig.4.10, left). Next, we subjected the system to the same force, but abruptly cut it when it reached its maximum, and let the system oscillate freely. No hysteresis has been observed in this case (fig.4.10, right): apparently the system oscillations are able to delete hysteresis.

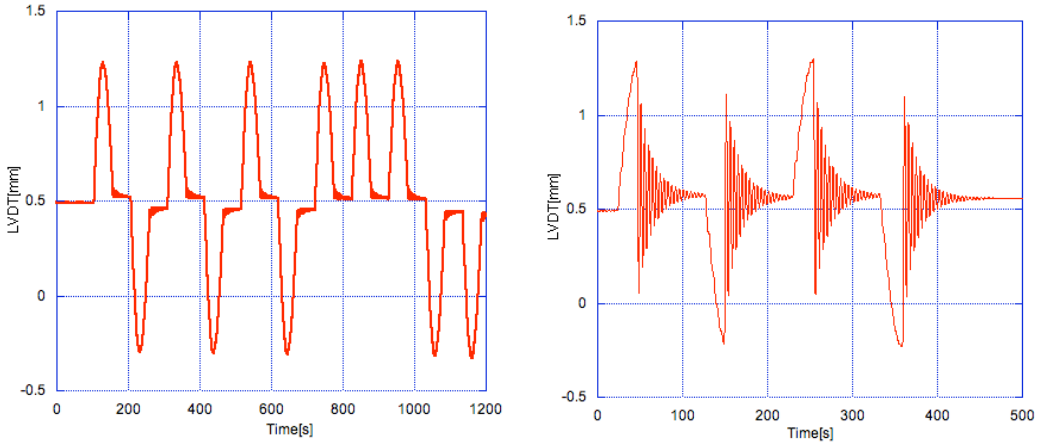

Figure 4.10: resonant frequency 220 mHz. Pulse excitation with half period sinusoidal lifting force that grows and then fades at a speed slower than the system response time, non negligible hysteresis is observed (left). Pulse excitation with quarter period sinusoidal lifting force, no hysteresis is observed after the first excitation (right).

The procedure was repeated with the same mechanical tuning for different K_{emas}, corresponding to progressively lower resonant frequencies. For

an EMAS spring constant K_{emas}=-66.86 N/m, that provides a resonant frequency of 150 mHz, the springs present such a low Q-factor that the residual oscillations are not sufficient to delete hysteresis even in the quarter period excitation (fig.4.11 right to be compared with fig.4.10 right). As for the half period excitation, we found that hysteresis grows rapidly for lower frequency tunes (fig.4.11 left to be compared with fig.4.10 left).

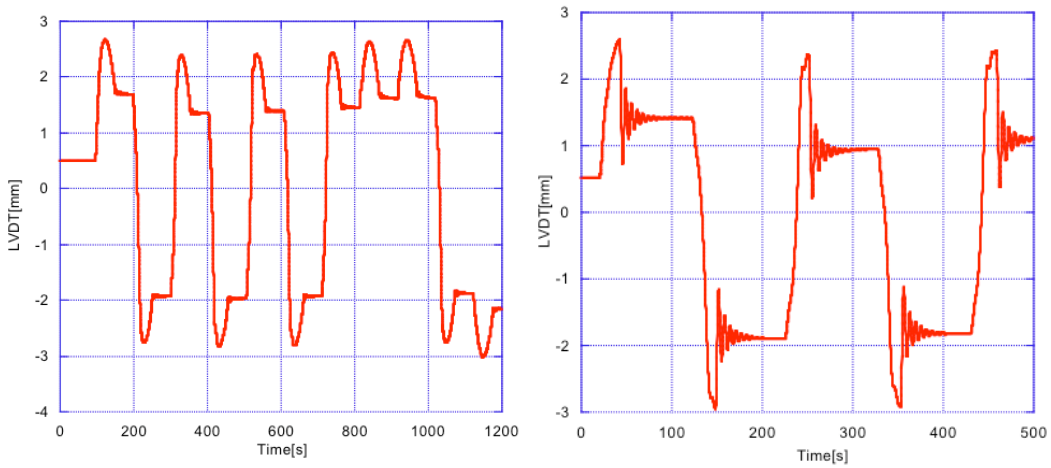

Figure 4.11: resonant frequency 150 mHz. Half period excitation (left) and quarter period excitation (right) both show hysteresis. The amount of hysteresis is much larger than the one found with 220 mHz resonant frequency of fig.4.10.

The amount of hysteresis increases rapidly for frequency tunes lower than ∼0.20 Hz, accelerating markedly as the system gets into the instability region (see instability study in section 4.6.4). At the lowest frequency settings, which are well inside the instability region, the excitation seems to simply drag the springs equilibrium point to a new location, with little resistance and very limited return, as in fig.4.11. Notice that with the same amplitude pulse (1V) the spring moves much more at lower frequency tunes, due to the weakness of the system (compare the 1.25mm initial growth in the signal of fig.4.10, whose tuning was 220 mHz, with the 2.5mm initial spring's height of fig.4.11, corresponding to a resonant frequency of 150 mHz).
The proposed explanation is that elasticity is composed of two parts: the bulk, immutable, provided by the crystalline structure, and a percentage provided by entangled dislocations. The second contribution changes with

the dislocation network distribution: the filter's equilibrium point depends on where the dislocations entangle and freeze. The dislocations, mobilized under the pulsed stresses, re-entangle eventually in different equilibrium position, thus explaining the observed hysteresis. The GAS and the EMAS mechanisms reduce the overall restoring force thus exposing and enhancing the effect. The effect is dramatically evident when the system approaches the lowest frequencies, where the restoring force of the crystal lattice structure is almost nulled by the EMAS mechanism: we found 3.5 mm of hysteresis in the filter position for a filter tuning of 220 mHz (fig.4.11), and less than 0.5mm with a 150 mHz tuning (fig.4.10).
To cross check that it is the oscillatory motion, and not its speed, that erases hysteresis, we subjected the system to a slow oscillatory force, driving the system with a 50 mHz sinusoid, namely slower than the system resonant frequency. Each excitation had an initial 0.5V amplitude, damped with an exponential lifetime of 80 s. Each individual excitation started with alternate sign. The forced oscillation used exactly mimics, at lower frequency, the damped oscillations of fig.4.10, right panel, which generated no hysteresis. This experiment was substantially longer than the preceding ones, and subject to thermal drift, since the thermal compensation system was disabled. At a resonant frequency of 150 mHz, no hysteresis but just a small, monotone thermal drift has been observed, as shown in fig.4.12; we conclude that damped oscillations efficiently wash-out static hysteresis forces from the system.

A possible explanation for the observed behavior is that the forced oscillations move the dislocation network back and forth, impeding the dislocation accumulation in both directions and the formation of metastable equilibrium points: no hysteresis can thus be observed. We also noticed that for very small excitation amplitudes the thermal drifts dominate, and completely alter, the hysteresis behavior. Even if the dislocation landscape is flattened below the critical slope, thermal drifts can later tilt it again, restarting the avalanche process and the equilibrium point random walk or run-away. This is an important consideration: since in seismic isolation system and seismometers the flexures will always operate in the small or null excursion regime, the thermal history of the instrument will inevitably dominate the spring behavior and its excess low frequency noise. Temperature variations can affect the internal stresses and change the dislocation landscape, providing the energy for avalanches that can be triggered by other stimuli, as well as by other non-observable causes like tilt, vibrations etc. In the GAS vertical

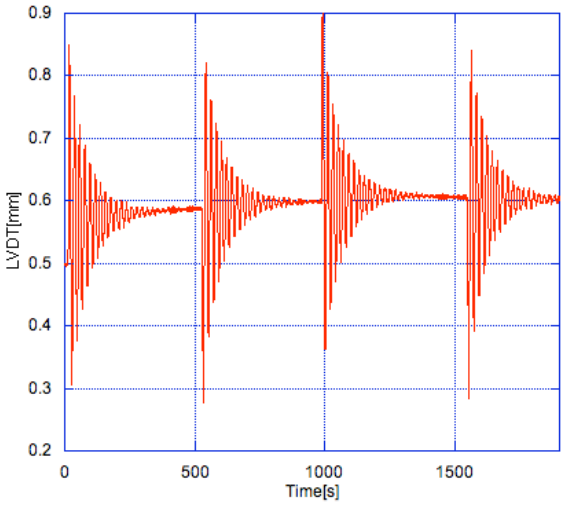

Figure 4.12: Forced, damped-sine excitations with frequency, 50mHz, slower than the filter frequency tune, 150 mHz, have been applied. The exponential lifetime, 80s, was chosen to drive the system through the same number of oscillations per lifetime than in the case of fig.4.10, right panel. The excitation is repeated with alternate sign. No hysteresis is observed.

springs temperature variations generate a tilt in the dislocation landscape. For horizontal oscillators like Inverted Pendula, actual ground tilts play the equivalent role, causing the random walk of the filters equilibrium point. Finally, for comparison with the behavior studied in the next two sections, I want to remark here that the onset of the disproportionate response to the excitation pulses seems to start at or around 0.20 Hz.

4.6.3 Quality factor measurements

We performed measurements of the system Q-factor for different frequency tunings. The EMAS mechanism has been particularly good for this measurement because it allows to remotely change the filter's resonant frequency all the way to zero frequency (mathematical instability), without perturbing the ambient (our mere presence in the laboratory has dramatic effects, mostly because of our body heat and the heat from the lights), without changing the mechanical stress in the system and without losses. For each EMAS set-

ting, which means for different resonant frequencies, we excited the spring applying a short voltage pulse on the actuator, and monitored the oscillation ringdown. Because of the higher stiffness, we applied 1V excitation amplitudes at higher frequency tune, reducing them to 0.1V at lower frequency tunes, to avoid triggering run-off instabilities (discussed in section 4.6.4). Analyzing each ringdown data with a damped sinusoid function we extracted the frequency and the lifetime, which correspond to the fit parameters $m3$ and $m5$ in fig.4.13. For each system tuning we calculated the system Q-factor, defined as $Q = \omega\tau$. For every setting we restricted the data used in the fits to similar oscillation amplitudes before extracting the frequency and the lifetime of the oscillation to obtain the Q-factor. We observed that both the fitted frequency and fitted lifetime slowly change with amplitude (see discussion in section 4.6.5 and 4.6.6), thus degrading the quality of long baseline fits: to improve the fit quality, we added an amplitude dependent term to the frequency and to the lifetime, but this expedient resulted in small corrections that did not significantly change our results.

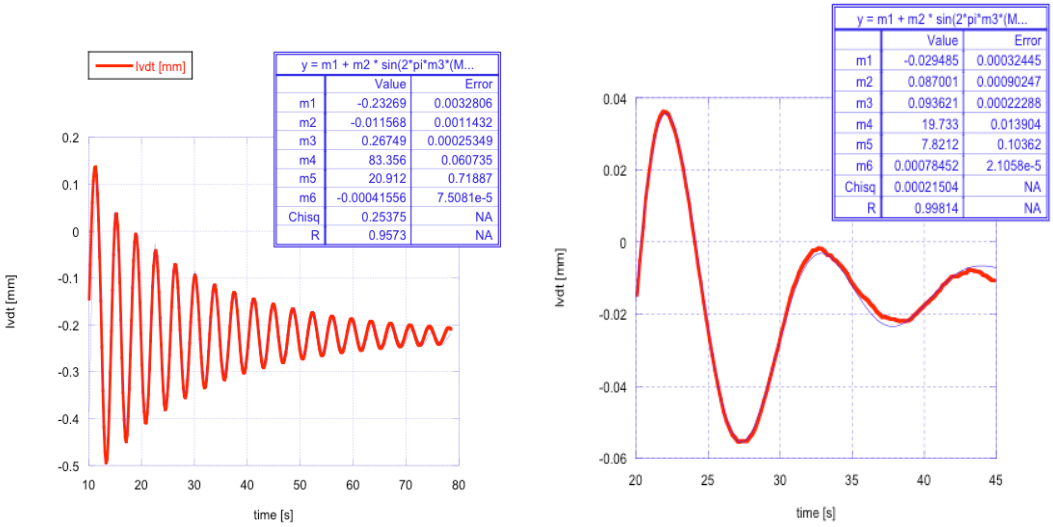

Figure 4.13: Fit of an intermediate frequency data set (left) and of the lowest achieved frequency with an almost critically damped oscillator (right).

The lowest frequency achieved is ∼0.94 Hz (fig.4.13 right panel), corresponding to K_{emas}=-130.38 N/m, according to eq. (4.6) with a mechanical filter tuning of 240 mHz at the working point. Attempts to tune the spring to

lower values resulted in sudden changes of the equilibrium position triggered by the excitation pulses, see fig.4.21.
Being the Q-factor defined as the energy stored in the system divided by the energy dissipated per cycle, it is clear that it should follow a quadratic function of frequency if the losses per cycle are frequency independent, i.e. if we are in a purely hysteretic regime.
We found the expected quadratic behavior at low frequency, and a deviation from it at frequencies at or above 0.20 Hz, as if a loss mechanism were depressed at high frequencies thus raising the Q-factor. In order to verify that the observed departure from the quadratic law was not related to a non-linearity in the control system, the GAS filter mechanical tune has been softened 23% in stiffness, by manually changing the radial compression of the blades, thus lowering the resonant frequency from 245 to 222 mHz, and the Q-factor has been measured again for several EMAS gains. The data of the two cases overlap, see fig.4.14 in which the two data sets are mixed together, and the point of departure from the quadratic law remained unchanged.
This indicates that the deviation from the f^2 law at $\sim$200 mHz is likely a property of the material, and not tune or EMAS dependent. The observed increase of the Q-factor implies strongly reduced losses at higher frequencies; this can be explained if the dissipation process needs a longer time, than the oscillation period, to develop. If the system is slow enough, a limit loss level is reached, corresponding to an hysteretic regime in which dislocation avalanches can fully grow and maximally mobilize, thus giving reason of the time independent dissipation (low Q-factor, quadratic in frequency) observed at low frequencies. At higher frequencies, less dissipation occurs, because there is no time for a full avalanche development, many dislocations are still entangled and cannot contribute to the dissipation processes: the Q-factor start to grow exponentially. Note that if the exponential fit used held all the way, the Q-factor would reach the well-known Maraging Q-factor [50] of more than 10,000 before 0.5 Hz.
For comparison, I want to report here a similar analysis already made on Maraging blades, even if with inferior measurement quality. In fig.4.15 the Q-factor of GAS and Monolithic GAS [37] (which is our case) filters is shown. The quadratic dependence from frequency was not evident at that time since the oscillations presented in that set of measurements did not contain very low frequency data and the Q-factor was limited by the different blade flexures.

One could suspect that the sample used in our experiment was somehow

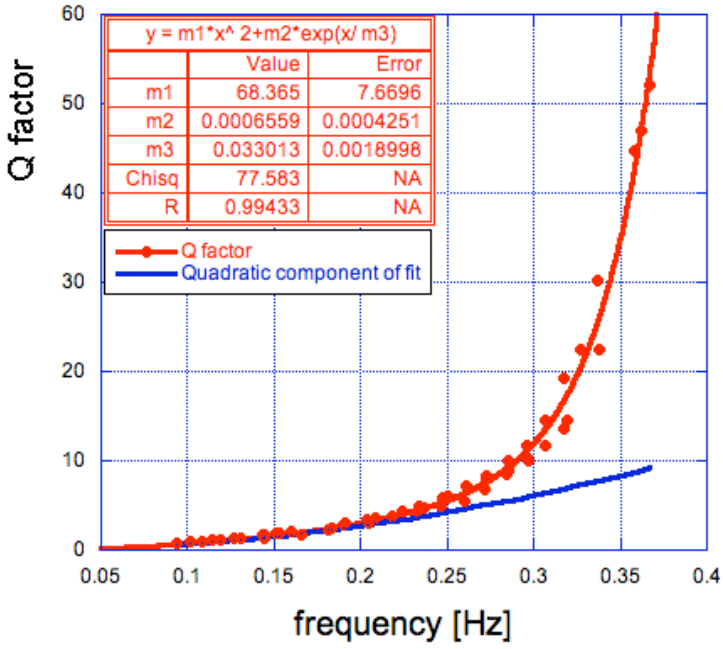

Figure 4.14: Q-factor of GAS filter.The data have been analyzed with an exponential profile deviation (red line) from a quadratic function. The blue line is the expected quadratic component of the fit, which dominates below 0.2 Hz. Data set of two different mechanical tunings are plotted here.

defective. As a cross check we took a spring from the same batch used in our setup. We tested a two-blade spring, but otherwise identical to the spring of the GAS filter used here, and suspended it in air from its center. We measured the Q-factor of its lowest resonances and plot it in fig.4.16.

As usual in these measurements the even modes, which bounce on the support point, have been found to have low Q-factor, while the odd modes, which have a node on the support point, present a Q-factor well above 10,000 even if the measurement is performed in air.
It is possible to conclude that the Maraging spring used is of good quality and our low frequency Q-factor measurements are representative of the material properties.
Remarkably, the frequency, ∼200 mHz, under which the Q-factor follows the quadratic law, it is exactly the same at which the hysteresis in the GAS filter displacement starts to be outstanding (see for example fig.4.11).

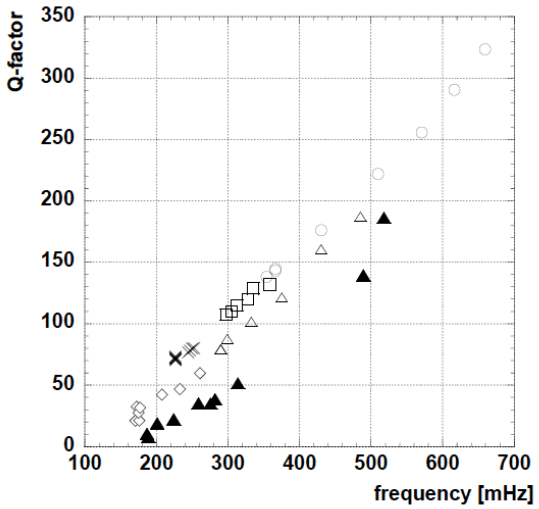

Figure 4.15: GAS (empty symbols) and Monolithic GAS (black triangles) filter Q-factor versus frequency. Picture from [37].

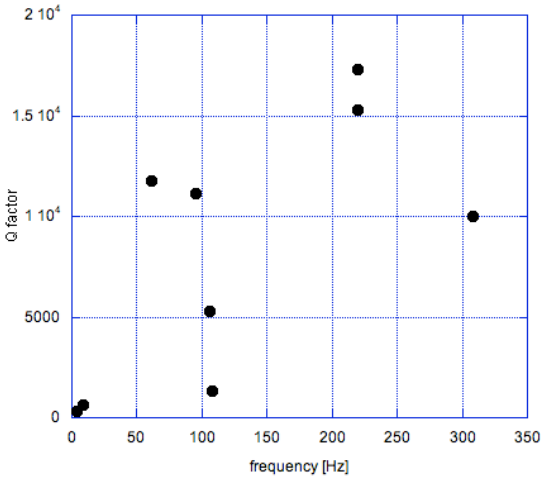

Figure 4.16: Q-factor lower limit measurement of a free Maraging spring from the same batch of the one used in this experiment. The even modes that bounce on the support have bad Q-factors, while the odd modes have normally high Q-factors ($\geqslant 10,000$).

4.6.4 Low frequency instability

Exciting the system, which was tuned below 200 mHz, we observed that the spring occasionally runs away from its equilibrium point, indifferently up or down: large pulses were necessary to destabilize the system at higher frequency settings, while at the lowest oscillation frequency achieved, 94 mHz, even a short pulse with amplitude of less than 3 mN (over the 65 kg payload) was able to drive the GAS filter into collapse. At lower EMAS gain, ambient perturbations are sufficient to cause the spring's run-off. It is important to remember that a stable oscillator cannot spontaneously destabilize without a failure of Hooke's law of elasticity. Unexplained collapse has been already observed in low frequency systems as different as IPs [41], Virgo [39] and TAMA [40] IP tables, Virgo SA filters, LIGO and TAMA GAS filters [37], etc.
In order to explore the run-off instabilities, the GAS filter was scanned with increasing negative K_{emas}, i.e. monotonously decreasing resonant frequencies, while maintaining the filter at its working point position with a slow position correction integrator. With the noise level of our laboratory, the run-offs were observed to start at around 40 mHz, substantially far from the mathematical instability marked by the zero frequency in fig.4.17. Evidently the perturbation level in the laboratory is sufficient to impede stability at that low frequency. The run-offs happened at random directions, either up or down, thus eliminating the hypothesis of creep or stress induced effects which would have happened only in the down direction.
As a comparison, in a much more thermally stable and quiet Synchrotron laboratory at Caltech, inside a more than 20 times stiffer hut to protect from air currents, it has been possible to bring the same spring at a minimum frequency of 30 mHz without excitation [35] and the HAM-SAS table [51] under vacuum and stable thermal conditions,operated at 10 mHz for hours during an FFT measurement and it only run-off when an external excitation was applied.

Note that the initial run-off is slow, much slower than the time constant corresponding to the frequency tune (the tune at the collapse was at about 40 mHz, corresponding to a 4 s characteristic time), and then accelerates, as illustrated in fig.4.18: this observation seems to indicate that some suddenly-activated, Young's modulus reducing mechanism occurred somewhere inside

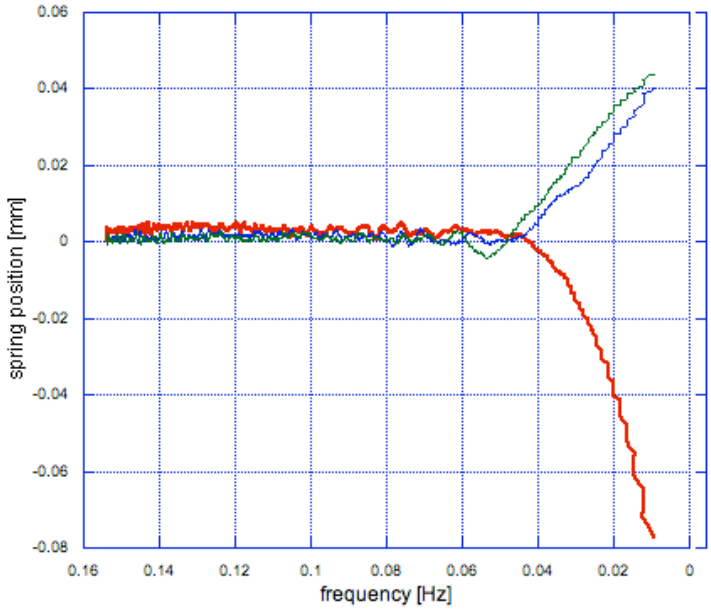

Figure 4.17: The filter tune is scanned down in frequency through the EMAS mechanism. The run-offs start at about 40mHz.

the blades and propagated through them. The effect can be explained if one accepts that the restoring force provided by the crystalline structure is nulled by the GAS and the EMAS mechanisms, and that the system is kept stable only through the restoring force provided by the entangled dislocations. A perturbation that causes some dislocations to disentangle can trigger collapse. To explain the macroscopic run-off of the large payload, the perturbation must propagate to the entire spring's volume (spring size ∼38cm). It can be seen as a domino effect in which a single localized event slowly sets in motion avalanches involving a growing number of dislocations in its neighborhood. The collapse happens when a sufficient number of disentangled dislocations are mobilized and stop providing their share of restoring force. Avalanche propagation is not appreciable at higher frequency oscillator tune, where the more rapid oscillation of the stress field limits the time for development of individual avalanches, thus preventing the domino effect from extending over macroscopic distances: no collapse events are observed at frequencies higher than 200 mHz. At low frequency, instead, dislocation avalanches can grow

indefinitely producing observable macroscopic effects, as the full collapse of the spring.

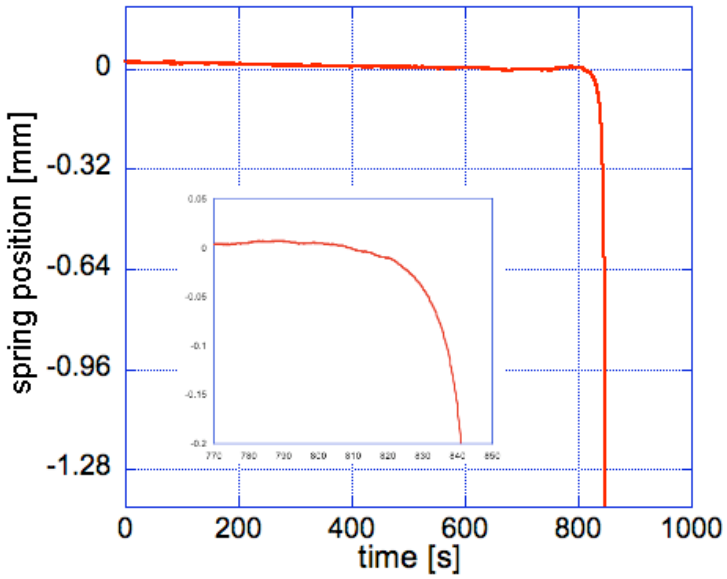

Figure 4.18: Single run-off at fixed frequency. The filter abandons the equilibrium position first very slowly (see insert), even slower than its characteristic time constant, then accelerates rapidly.

To verify that the process involved in this fall is connected to the propagation of dislocation avalanches, we wrote a program able to detect the beginning of a run-off with a threshold of 30 mV ($\sim$24 μm according to the LVDT calibration) and to instantly reduce the absolute value of the EMAS gain, that means to bring the K_{emas} toward a less negative value, increasing the resonant frequency. The spring is thus temporarily stiffened and the range of avalanche propagation is diminished. The filter was tuned under 200 mHz, inside the instability region. After the system has recovered equilibrium the K_{emas} is restored to the original value, following an exponential decay law as in fig.4.19. The lower (in modulus) K_{emas}, the higher resonant frequency and the stiffer spring simply increase the fraction of restoring force contributed by the fixed crystal and allows the spring to find an equilibrium point compensating for the accumulated thermal stress close to the old equilibrium point, thus stopping the collapse. Without the contribution from the

fixed crystal elasticity and without the recovery algorithm the dislocations would have simply moved creating avalanches, causing the system run-off. From the point of view of controls, the program was very unsophisticated, it simply restored the EMAS gain with a time constant slower than the thermal integrator. A more sophisticated program may detect the run-off at smaller values and change all integration parameters to re-stabilize the spring in a much shorter time and much less excursion.

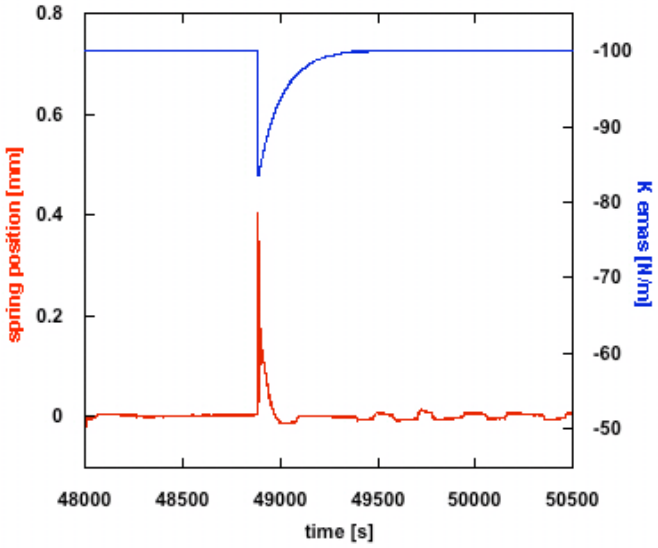

Figure 4.19: Reducing the K_{emas} (blue line), in this example from -100 to -80 N/m, the spring's run-off (red line) is stopped. The filter is then slowly returned to its equilibrium position using the integrator; finally the K_{emas} returns to its original value.

We also observed, fig.4.20, a substantial difference between night and day. During night-time essentially no run-off is generated while in day-time several ones are triggered and recovered.
More remarkably, the data suggest that most small events initiate but recover naturally without triggering the re-stabilization mechanism. In fig.4.21 one of these aborted run-offs is shown, when the filter was tuned below 150mHz: the system changes its equilibrium position after the collapse event, compat-

ibly with a dislocation network which finds a new equilibrium configuration. In this case the system responded to a large excitation pulse, which caused the equilibrium point to shift to -2V. Instead of oscillating around its working point, the filter oscillates around that position. While the integrator slowly drags the oscillation towards the working point (0.35V), the filter suddenly finds a different equilibrium position at +2.5 V and oscillated there.
If we tune the system to very low frequency all avalanches may grow unhindered and the system collapses after a very short time.
An appropriate recovery procedure as the one discussed above, however, suffices to damp avalanches without requiring high stiffness. Avalanches of dislocations probably happen both in quiescent soft and stiff systems, and in similar amounts: their propagation may be hindered in stiff systems and not apparent, but the underlying microscopic noise process may be the same. In absence of external drifting stimuli (thermal for vertical springs, tilt for IPs), after sufficient settling time, the noise level should be the same for soft and stiff systems.
To conclude this section I want to underline that the cut-off frequency for system instability is, again, $\sim$200mHz.
The hysteresis studies,the Q-factor behavior and the collapse events all bring us to think about the same underlying effect which is, very likely, the entanglement and disentanglement of dislocations.

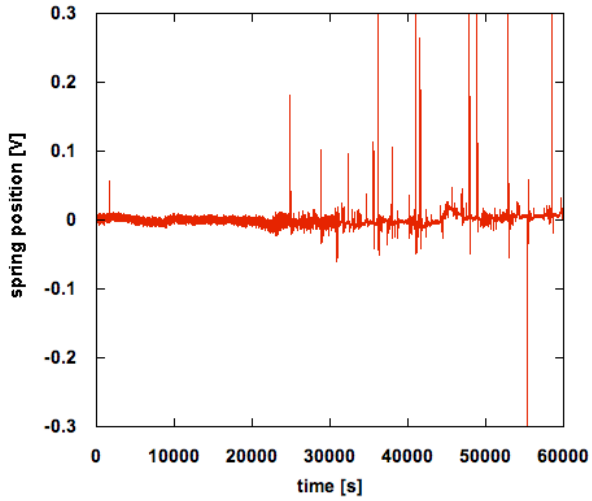

Figure 4.20: The filter is stable and virtually free from run-offs during the night (first 20,000 seconds of the graph) while during the day several events are detected.

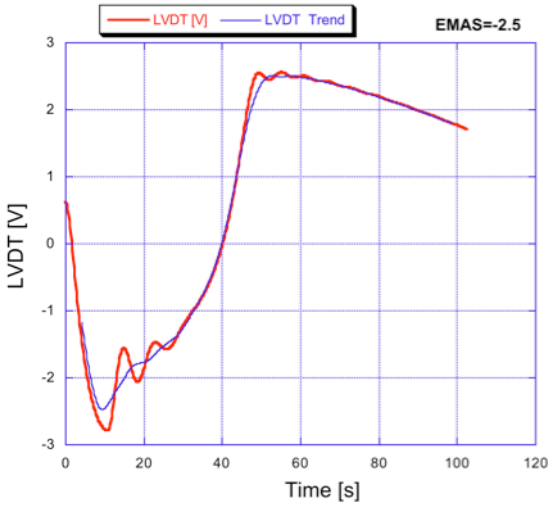

Figure 4.21: Single run-off event which recovers spontaneously. After excitation and ringdown the spring spontaneously leaves an equilibrium point and finds another one.

4.6.5 Expected and measured frequency versus amplitude

We studied the shape of the spring resonances versus frequency, performing two sets of swept sine measurements of different excitation amplitudes, one made with K_{emas}=0 N/m and one with K_{emas}=-66.86 N/m. In both cases the mechanical GAS tune was 220 mHz. Fig.4.22 shows these results, in which the scans have been repeated with increasing excitation amplitude starting from 0.1V up to 2.5V. Each scan has been made sweeping the frequency first up and then down: in the two cases a small difference, in the height of the resonant peaks, has been found, and we chose to take the mean value between the two.

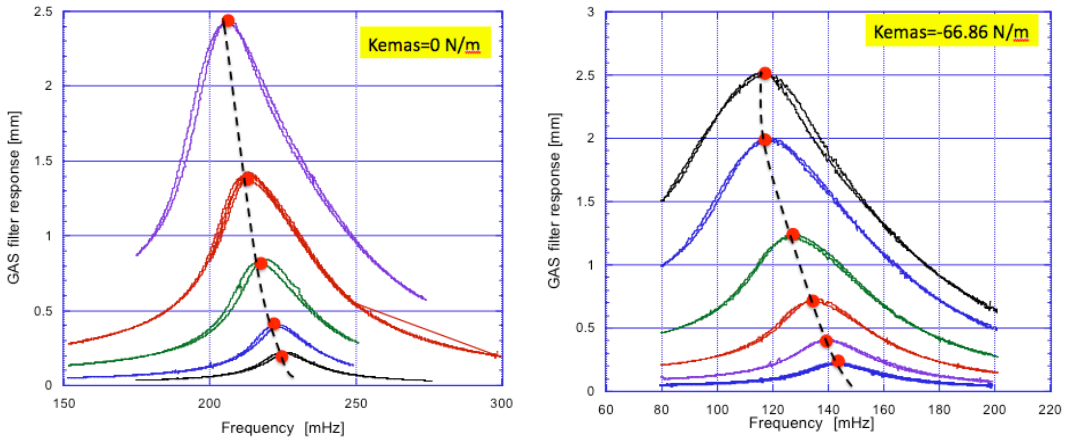

Figure 4.22: Swept sine response of the system to increasing excitation amplitudes, from 0.1 to 2.5V.

Following the dashed line which connects these resonant peaks, it is immediate to note that the resonant frequency of the system decreases for increasing excitation amplitudes. This was a very strange behavior: as detailed later we expected an increase of the resonant frequency with amplitude. As a cross check we looked for this effect in the time domain measurements and we observed the same behavior.
We repeatedly excited the filter with large pulses and let it ringdown for 6 or 7 lifetimes, until the oscillation signal faded in the measurement noise. Each ring-down was subdivided in 11 windows, each 25 second long, spaced

at 12.5 s intervals with a 50% overlap between the windows. In each window the ringdown of the signal was analyzed with the same damped sinusoid function of (4.5), from which we extracted the values of the amplitude A, the resonant frequency f and the damping time τ, and their relative fitting errors. We repeated the operation for several ringdowns and plotted the data of the frequency versus amplitude in fig.4.23:

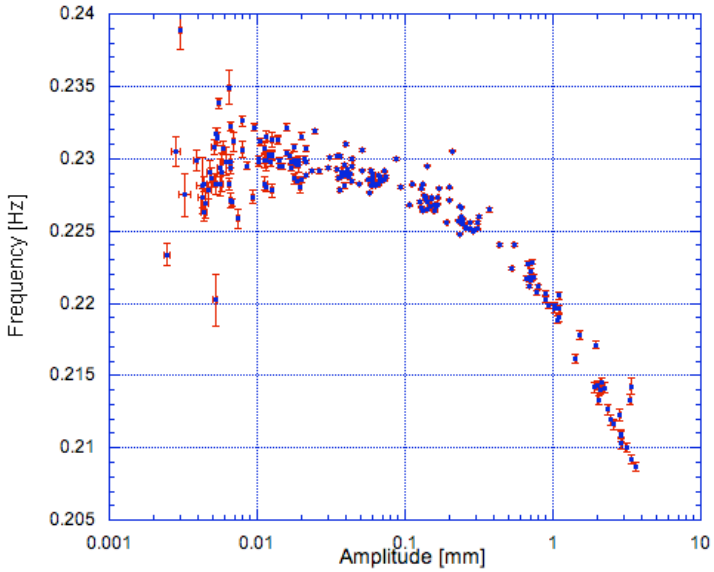

Figure 4.23: Frequency versus amplitude plot, obtained from sliding windows over ringdown data.

The graphs confirms the frequency reduction for increasing excitation amplitude.
This behavior is very unexpected: from the non-linear characteristics curve of fig.4.6 we would expect to observe an increase of frequency with larger oscillation amplitude, because larger oscillations force the system to explore regions of higher frequency. In order to quantify this discrepancy an accurate evaluation of the expected frequency dependence from amplitude was made. At the first order the force acting on a GAS spring is $F = -kx$, which would give an amplitude independent, and therefore constant, oscillation frequency $f = \sqrt{k/m}/2\pi$; the amplitude dependent frequency observed in fig.4.6 requires, instead, consideration of the higher order terms. Because fig.4.6 has no hint of asymmetry, the potential energy describing the ob-

served amplitude-dependent frequency has to be an even function of the displacement x. The simplest potential energy describing our data has the form:

$$U = \frac{1}{2}kx^2 + bx^4 \tag{4.7}$$

This is also the potential energy required to take into consideration the reduction of the radial compression induced by vertical motion in the simplified GAS mechanism model of fig.4.2. The resulting force is

$$F = -kx - cx^3 \tag{4.8}$$

and its equation of motion is

$$m\ddot{x} + kx + cx^3 = 0 \tag{4.9}$$

which we solved numerically using Mathematica with initial conditions m=65kg, K=125.5 N/m (from the resonant frequency f=0.2213 Hz at the working point). The coefficient c =2,200,000 N/m^3 was tuned with less than 5% error to match the frequency dependence of fig.4.6. Once fixed the coefficients, we simulated progressively larger oscillation amplitudes around the working point and monitored the frequency, thus obtaining fig.4.24.

The data were fitted with a parabola and the parameters of this quadratic fit were used to calculate the expected frequency for each of the points of fig.4.23. The experimental points of fig.4.23, in fact, must be compared against this expected frequencies, and not against a constant value as we have done in a previous work (see Appendix B). Finally, we plotted the expected and the measured frequency vs. amplitude in fig.4.25.

For completeness, we considered an additional amplitude-dependent contribution to the frequency. It is well-known that in a damped harmonic oscillator the oscillation frequency is reduced, with respect to the un-damped case, by a factor proportional to the square of the damping constant γ. Some authors already tried to measure such a reduction, see for example [52]: this "frequency redshift", however, is usually small and hard to quantify. Because, as shown in section 4.6.6, we observed an amplitude dependent lifetime, we can expect a correspondingly amplitude-dependent damped coefficient as well. We calculated this term to see if it could explain the unexpected frequency vs. amplitude dependence discussed above. Thus, using the lifetimes of fig.4.27, we calculated the $\gamma^2(A)$ term to be subtracted from

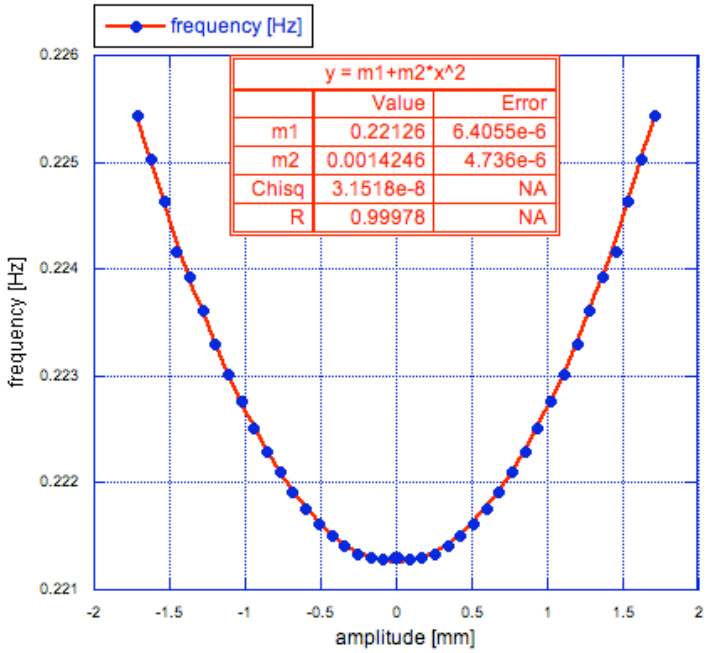

Figure 4.24: Expected frequency versus amplitude plot, obtained with small amplitude oscillations simulated from a four order potential energy. The data have been fitted with a quadratic function.

the frequency of each point of fig.4.23, and found it negligible. For additional caution, we added a viscous term $\gamma(A)\dot{x}$ in the differential equation (4.9), taking into consideration the varying damping lifetime of fig.4.27, and calculated the frequency reduction coming from this contribution. We found the same negligible reduction of the expected frequency in the amplitude range of interest: the viscosity of the system does not justify the observed frequency reduction.
The deviation of the measured frequency from the expected one is obtained by subtracting the two data sets of fig.4.25; the result, as in fig.4.26, is a quasi linear dependence of frequency from amplitude. If the data are fitted with a power law, an amplitude exponent of 0.92 ± 0.02 is found. We applied the same correction to the frequency-domain data of fig.4.22 left panel, and found them compatible with the same linear deviation (red dots in fig.4.26). The error bars of the frequency come from fit results in the case of ring-

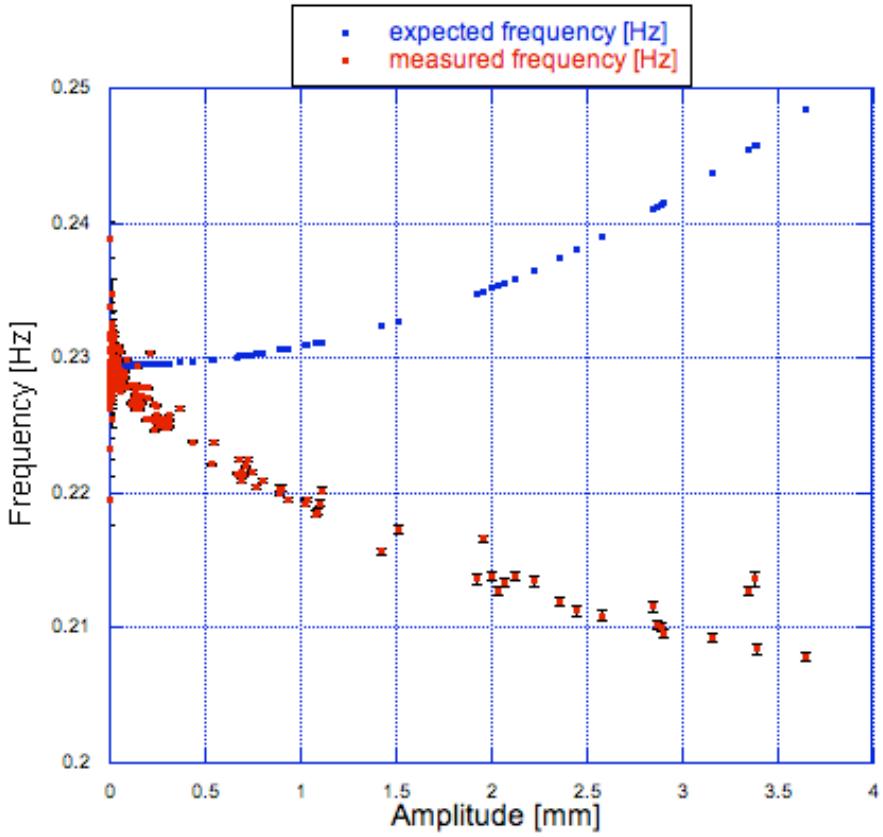

Figure 4.25: Expected (blue dots) and measured (red dots) frequency in the experimental amplitude range.

down measurements and from the experimenter's judgment in the case of swept-sine measurements.

The deviation of the measured frequency from the expected one has been attributed to the partial disappearance of the fraction of elasticity provided by entangled dislocation inside the material. For higher amplitude stress, in fact, the dislocations network can be disentangled thus reducing the elasticity of the system and therefore its resonant frequency. In other words this measurement corroborates our theoretical assumption that dislocations contribute to the elastic constant and, when disentangled, they can reduce the effective Young modulus.

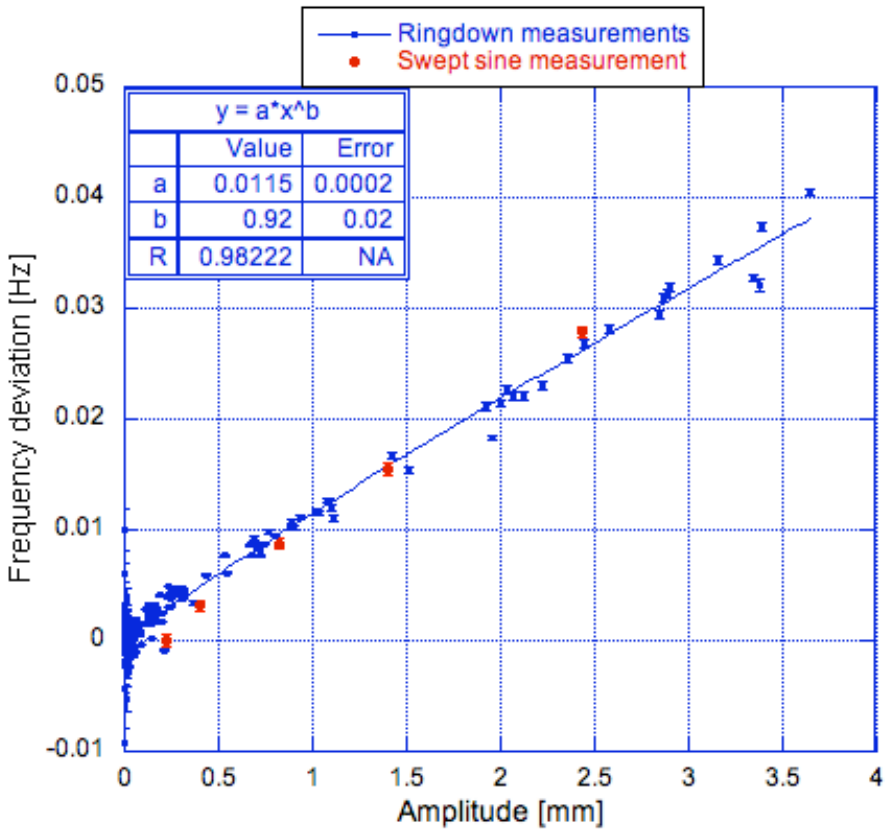

Figure 4.26: Frequency deficit: difference between the expected and the measured frequency for time-domain (blue points) and frequency-domain (red points) data. The two data sets were merged and fitted together and a quasi linear dependence from amplitude was found.

Remarkably, the dependence that we obtained is still a power law of the amplitude, compatibly with the SOC statistic.

4.6.6 Dissipation dependence from oscillation amplitude

The assumption that disentangled dislocations weaken the material Young's modulus led us to think that they might also cause increased dissipation. From the same set of ringdown data of fig.4.23, we extracted the damping time versus amplitude and fitted it with the function

$$\tau = \frac{1}{d_0 + \delta A^y} \tag{4.10}$$

where d_0 is the intrinsic dissipation and δA^y describes a possible contribution from the disentangled dislocations. The fit nails the exponent y very close to 0.5, compatible with this value within 1.2 standard deviations, as in fig.4.27. Note that only a power law can satisfactorily fits the data and all the other functions that we thought of failed.

As a further cross-check we re-analyzed the frequency-domain data of fig.4.22, extracting the damping constant τ from the resonance full width at half maximum (FWHM) of the swept sine measurements. Plotting these lifetimes versus the corresponding amplitudes and fitting them with the previously used eq.(4.10) it has been found an exponent $y = 0.34 \pm 0.46$ for $K_{emas} = 0N/m$ and $y = 0.86 \pm 0.17$ for $K_{emas} = -66.86N/m$. These values may seem distant from the exponent found in the time domain data of fig.4.27; however, by setting the exponent to the fixed value of 0.5, we still obtained good fits, as in fig.4.28.

In both cases we found the damping constant τ decreasing for higher oscillation amplitude, this reduction being proportional to the square root of the strain A. The proposed explanation is that larger oscillations can disentangle dislocations, which can thus move freely and cause increased dissipation with shorter lifetimes. All the studied effects can be regarded as the manifestation of one critical phenomenon: the dislocations disentanglement, which is responsible for the reduction of the Young's modulus and the simultaneous increase of dissipation.

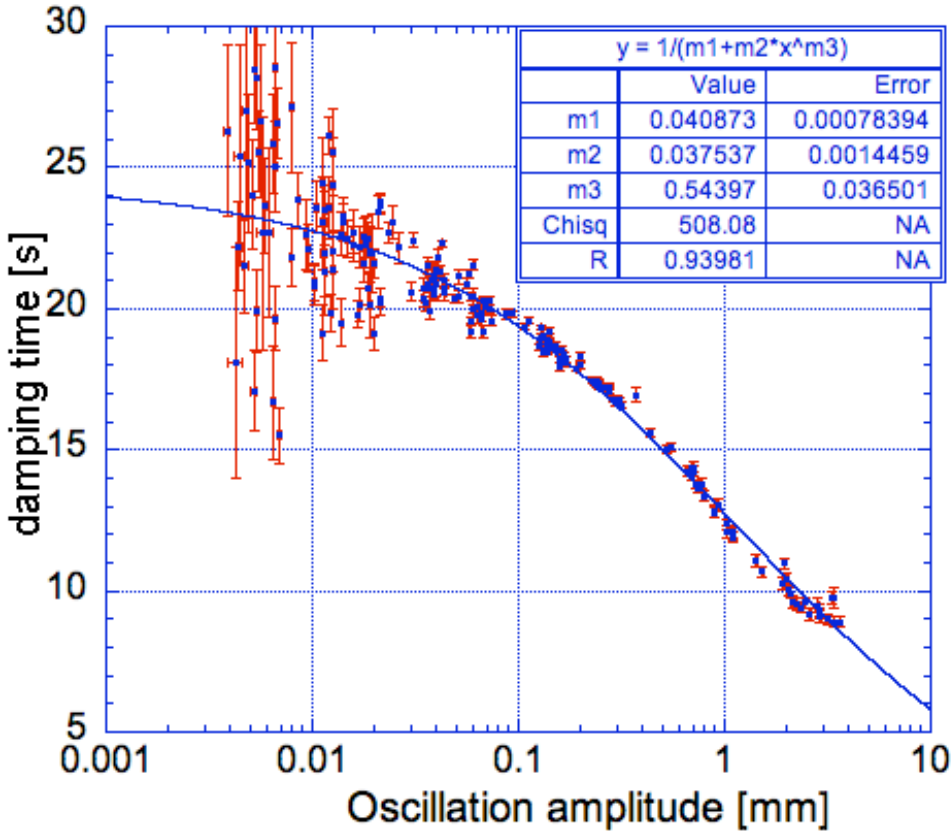

Figure 4.27: Lifetime versus amplitude plot, obtained from sliding windows of ringdown data, fitted with an amplitude dependent term.

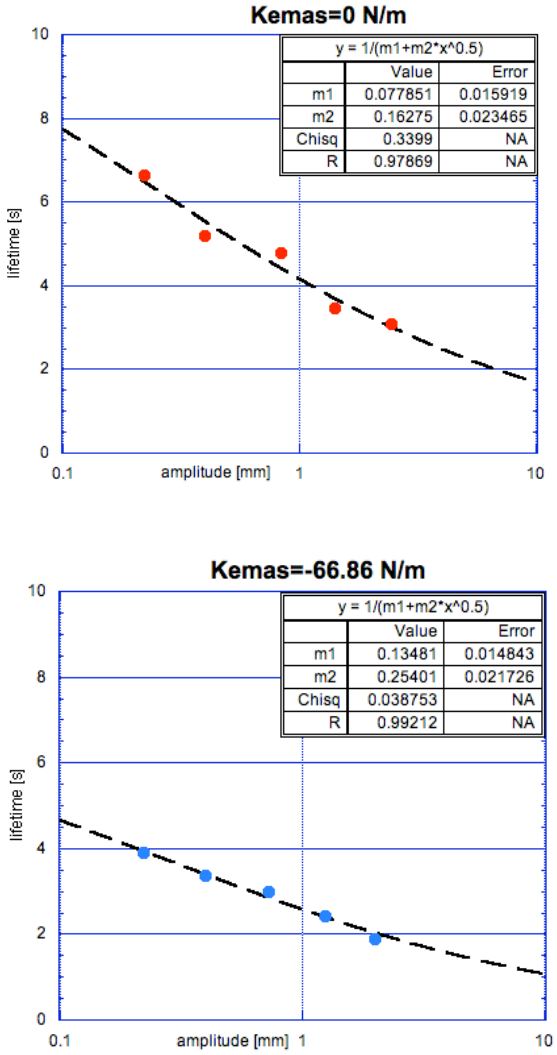

Figure 4.28: Lifetime versus amplitude, obtained from the swept-sine measurements of fig.4.22. The red points refers to the $K_{emas} = 0N/m$ case, while the blue ones are for $K_{emas} = -66.86N/m$.

Chapter 5

Conclusions

The extension of the detection bandwidth in the low frequency range of the third generation gravitational waves interferometers is a major challenge at present. I showed that the proposed sensitivity of the Einstein Telescope (ET) will permit the detection of signals from hundreds of pulsars.
I focused my experimental work on the reduction of low frequency mechanical noise in GW detectors, using a Geometric Anti Spring (GAS) filter.
Static hysteresis was the first indicator of something shifting inside the Maraging blades used in this experiment. This with the previously observed 1/f transfer function of the GAS filter were explained in terms of Self-Organized Criticality (SOC) dynamics of entangled/disentangled dislocations. Dislocations are usually entangled in a precipitation hardened alloy, such as Maraging, but they are not numerous enough to fully interlock as in a work hardened material. When, exposed to varying stress, the system reaches its critical state, the dislocations disentanglement induces avalanches which start spreading out in a domino effect, causing the system's partial or total collapse. Dislocation avalanches can also cause random walks of quiescent mechanical systems.
At low frequency mechanical tuning, below 0.2 Hz, an increased dissipation is observed in the GAS filter as well as an amplitude-dependent reduction of the system resonant frequency: these effects are attributed, once more, to the mobilization of dislocations inside the material. At higher frequencies, $>$0.2 Hz, we observed a different scenario. Disentanglement has no time to complete and a large fraction of dislocations remains inactive.
Inverted Pendula or GAS filters tuned at high frequency show the well-understood damped behaviors. This may be the case of most experimental

internal friction apparatuses, which are typically tuned at relatively high frequency, where the collective effects of dislocation are negligible. Therefore, extrapolating the result of a measurement to lower frequencies may lead to the underestimation of the low frequency losses and noise occurring in these devices. An avalanche dominated 1/f noise, in excess of that predicted by the fluctuation-dissipation theorem, may be expected at low frequencies according to the SOC.

The surprising behavior observed in Maraging steel may actually be typical of most, if not all, polycrystalline metals at sufficiently low frequencies. Further studies of loss mechanism are necessary to better understand and control the mechanical noise of the seismic attenuators in future low frequency interferometers, and in those presently under construction.

Referring, in particular, to the Einstein Telescope, it is imperative to take into account the noise which could be introduced by using Maraging blades in the seismic attenuation system: the entity of the problem is still unknown and it is not possible to rule out the hypothesis that the above mentioned mechanical noise would also affect the interferometer sensitivity at high frequency.

The presented results indicate that the most promising avenue will be to study materials or processes that would either stabilize the dislocations network, or at least eliminate their collective effects. Work hardening of the Maraging springs should be tried first to improve the quality of seismic attenuation filters with minimal changes. Later, new materials and processes need to be explored to design the seismic isolation of third generation, lower frequency GW interferometers, such as ET.

Glassy materials whose mechanical properties, unlike crystalline systems, are not dominated by topological defects such as dislocations, may be the ultimate materials for seismic attenuation filters and inertial sensors. They need, however, to be studied in detail, as different loss mechanisms may still spoil their performances.

Bibliography

[1] A. Einstein, *Die Grundlage der allgemeinen Relativittstheorie*, Ann. der Phys., 49, 769, (1916)

[2] J. H. Taylor, *Binary pulsars and relativistic gravity*, Rev. Mod. Phys., 66, 711, (1994)

[3] R. A. Hulse, *The discovery of the binary pulsar*, Rev. Mod. Phys., 66, 699, (1994)

[4] P.R.Saulson, *Fundamentals of interferometric gravitational wave detectors*, World Scientific, (1994)

[5] V.Ferrari, *Dispense del corso di Introduzione alla relativita' generale*, (2008-2009)

[6] C.Palomba, *Pulsars ellipticity revised*, Astron. Astrophys. 354, 163-168, (2000)

[7] LIGO project, www.ligo.caltech.edu

[8] B.Abbott et al, *Detector description and performance for the first coincidence observations between LIGO and GEO*, Nuclear Instruments and Methods in Physics Research A 517, 154-179, (2004)

[9] VIRGO project, www.virgo.infn.it

[10] VIRGO description, www.ego-gw.it

[11] GEO600 project, http://geo600.aei.mpg.de/

[12] G.Losurdo, *LIGO and VIRGO: large interferometers searching for gravitational waves*, http://hal.archives-ouvertes.fr, ICHEP, (2006)

[13] LISA 'Laser Interferometer Space Antenna', www.lisa.nasa.gov

[14] M.Punturo, *The VIRGO sensitivity curve*, VIRGO Note,VIR-NOT-PER-1390-51, (2003)

[15] DUSEL 'Deep Underground Gravity Laboratory', Final Proposal, (2009)

[16] G.Cella, *Underground reduction of gravity gradient noise*, GWADW talk, (2006)

[17] The Einstein Telescope 'ET', www.et-gw.eu

[18] M. Punturo on behalf of the ET design study team, *ET: Einstein Telescope design study* Presentation at ILIAS General meeting, (2008)

[19] S. Hild, S. Chelkowski and A. Freise, *Pushing towards the ET sensitivity using 'conventional' technology*, https://workarea.et-gw.eu/et/WG3-Topology, (2008)

[20] R.De Salvo, *The need for a Xylophone of GW interferometers*, Presentation, (2009)

[21] S. Hild for WP3, *News on the ET sensitivity curve*, https://workarea.et-gw.eu/et/WG4-Astrophysics/meetings/cardiff-090325WP4, (2009)

[22] B.S. Sathyaprakash and WG4 participants, *Einstein Telescope Design Study: WG4 Goals*, https://workarea.et-gw.eu/et/WG4-Astrophysics/presentations/ET-Goals, (2009)

[23] P. Amaro-Seoane and M. Freitag, *Intermediate-Mass black holes in colliding clusters: implication for lower frequency gravitational-wave astronomy*, Astrophys. J. 653, L53-L56, (2006)

[24] I. Mandel et al, *Rates and Characteristics of Intermediate-Mass-Ratio Inspirals Detectable by Advanced LIGO*, Astrophys. J. 681, 1431-1447, (2008)

[25] J.M.Miller, *Present evidence for intermediate mass black holes in ULXs and future prospects*, Astrophys. and Space Sc. 300, 227-238, (2005)

[26] ATNF Pulsar Catalogue, The Astronomical Journal 129, 1993 (2005)

[27] B. F. Schutz, *Introduction to the analysis of low frequency gravitational wave data*, Proc. of the Alpbach Summer School, (1997)

[28] G. F. Bignami, *Gamma Rays and Neutron Stars*, Science 322, 1193-1194, Published by AAAS, (2008)

[29] R. De Salvo, *Passive, Nonlinear, Mechanical Structures for Seismic Attenuation*, J. Comput. Nonlinear Dynam. 2, 290-98, (2007)

[30] G. Cella et al, *Monolithic Geometric Anti-Spring Blades*, Nucl. Instrum. Methods Phys. Res. A 540, 502-519, (2005)

[31] S. Braccini, F. Frasconi et al, *The maraging-steel blades of the Virgo super attenuator*, Meas. Sci. Technol. 11, 467-476, (2000)

[32] A. Stochino, *The HAM-SAS Seismic Isolation System for the Advanced LIGO Gravitational Wave Interferometers*, Master Thesis, (2006-2007)

[33] C. Wang et al, *Constant force actuator for gravitational wave detectors seismic attenuation systems (SAS*, Nucl. Instrum. Methods Phys. Res. A 489, 563-69, (2002)

[34] H. Tariq et al, *The linear variable differential transformer (LVDT) position sensor for gravitational wave interferometer low-frequency controls*, Nucl. Instrum. Methods Phys. Res. A 489, 570-76, (2002)

[35] M. Mantovani and R. De Salvo, *One hertz seismic attenuation for low frequency gravitational waves interferometers*, Nucl. Instrum. and Meth. 554, 546-54, (2004)

[36] A. Stochino et al, *Improvement of the seismic noise attenuation performance of the Monolithic Geometric Anti-Spring filters for gravitational wave interferometric detectors*, Nucl. Instrum. Methods Phys. Res. A 580, 1559-64, (2007)

[37] R. De Salvo et al, *Study of Quality Factor and Hysteresis Associated with the State-of-the-art Passive Seismic Isolation System for Gravitational Wave Interferometric Detectors*, Nuclear Instr. and Meth. A, 538, 526-537, (2005)

[38] J. Greenhalgh and I. Wilmut, LIGO Technical Report LIGO DCC T080033-01-K, (2008)

[39] P. Ruggi, VIRGO project, private comm.

[40] K. Arai, TAMA project, private comm.

[41] P. Saulson et al, *The inverted pendulum as a probe of anelasticity*, Rev. Sci. Instrum. 65, 182-91, (1994)

[42] J. M. Ziman, *Models of disorder*, CUP Cambridge UK, (1979)

[43] A. S. Nowick and B .S. Berry, *Anelastic Relaxation in Crystalline Solids*, Academic New York, (1972)

[44] J. P. Hirth and J. Lothe, *Theory of Dislocations*, McGraw-Hill New York, (1968)

[45] A. V. Granato and K. Lucke, *Physical Acoustics*, edited by Mason and Thurston Academic New York IVA 225, (1966)

[46] P. Bak et al, *Self-organized criticality: An explanation of the 1/f noise*, Phys. Rev. Lett. 59, 381-84, (1987)

[47] P. Bak et al, *Self-organized criticality*, Phys. Rev. A 38, 364-74, (1988)

[48] F. Marchesoni and M. Patriarca, *Self-Organized Criticality in Dislocation Networks*, Phys. Rev. Lett. 72, 4101, (1994)

[49] F. Marchesoni et al, *Damping in low-frequency mechanical pendulums*, Phys. Lett. A 187, 359, (1994)

[50] S. Braccini et al, *The maraging-steel blades of the Virgo super attenuator*, Meas. Sci. Technol. 11, 467-476, (2000)

[51] A. Stochino et al, *The SAS Seismic Attenuation System for the Advanced LIGO Gravitational Wave Interferometric Detectors*, Nucl. Instrum. Methods Phys. Res. A, 598, 737-753, (2008)

[52] D. Randall, *Friction at the mesoscale*, (2003)

Appendix A

Labview code

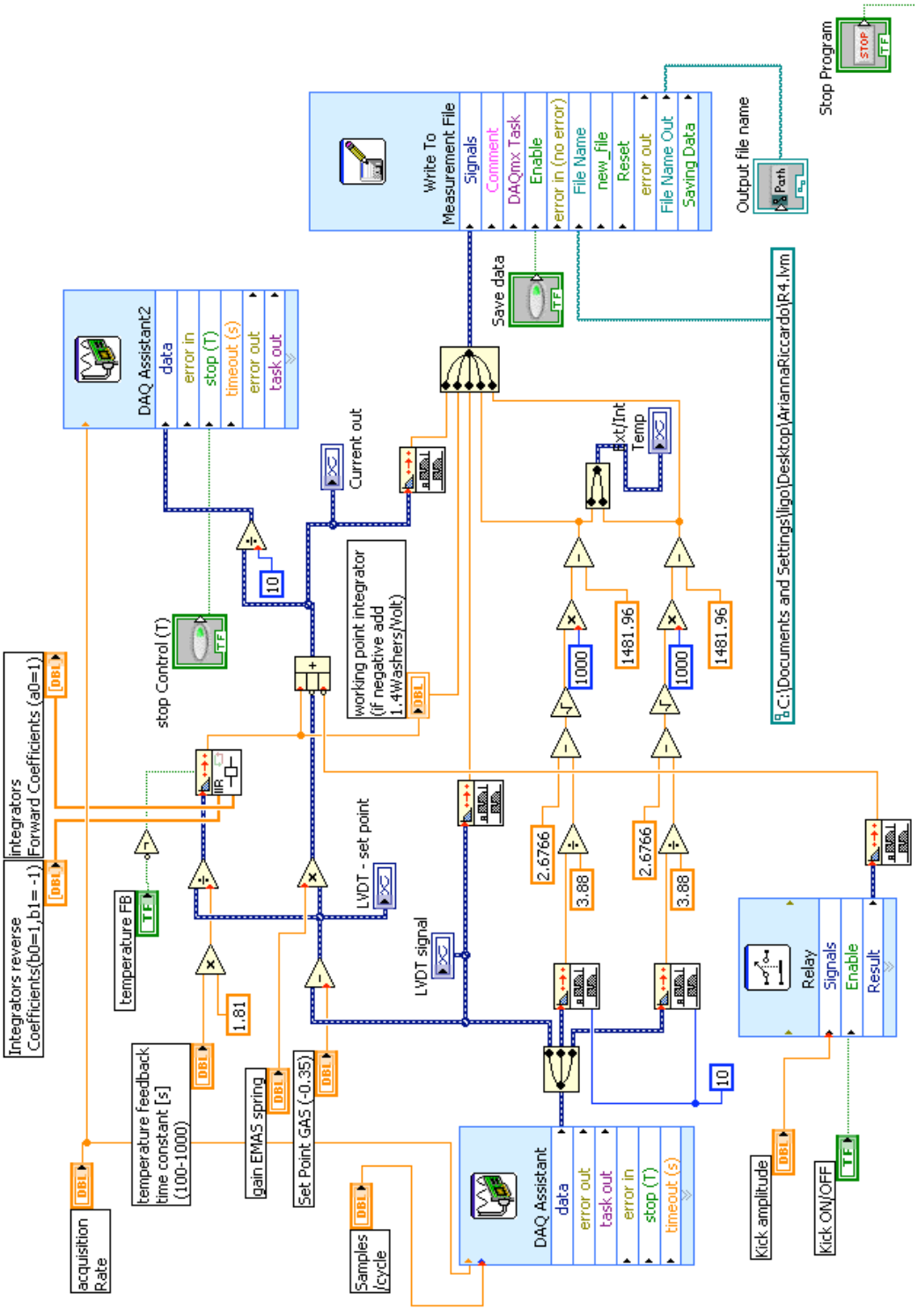

Figure A.1: Example of a Labview code with the IIR filter used to keep the GAS at its working point.

Appendix B

Paper

Proceeding of the 13th GWDAW conference.
Paper submitted to Classical and Quantum Gravity.

Dislocation movement and hysteresis in Maraging blades

Arianna Di Cintio [a,b], Fabio Marchesoni[c], Maria Ascione [a,d], Abhik Bhawal [e] and Riccardo De Salvo [a]

[a]*LIGO Laboratory, California Institute of Technology, MS 18-34, 1200 E.California Blvd., Pasadena, CA, 91125 USA*
[b]*Dipartimento di Fisica, Università degli studi di Roma "Sapienza", 00185 Roma, Italy*
[c]*INFN-VIRGO Project Dipartimento di Fisica, Universita' di Camerino, I-62032 Camerino, Italy*
[d]*Dipartimento di Ingegneria, Università del Sannio in Benevento, I-82100 Benevento, Italy*
[e]*Arcadia High School, Arcadia, CA, USA*

Abstract

All seismic isolation systems developed for Gravitational Waves Interferometric Detectors, such as LIGO VIRGO and TAMA, make use of Maraging steel blades. The dissipation properties of these blades have been studied at low frequencies, by using a Geometric Anti Spring (GAS) filter, which allowed the exploration of resonant frequencies below 100 mHz. At this frequency an anomalous transfer function was observed in GAS filter: this is one of several motivation for this work.
The many unexpected effects observed and measured are explainable by the collective movement of dislocations inside the material, described with the statistic of the Self Organized Criticality (SOC). At low frequencies, below 200 mHz, the dissipation mechanism can subtract elasticity from the system, even leading to sudden collapse. While the Young's modulus is weaker, excess dissipation is observed. At higher frequencies the applied stress is probably too fast to allow the full growth of dislocation avalanches, and less losses are observed, thus explaining the higher Q-factor in this frequency range. The domino effect that leads to the release of entangled dislocations allows the understanding of the random walk of the VIRGO and TAMA IPs, the anomalous GAS filter transfer function as well as the loss of predictability of the ringdown decay in the LIGO-SAS IPs.

1. Introduction

A study of the dissipation processes in Maraging blades has been carried out by using the Geometric Anti Spring (GAS) mechanism [1].
The GAS filter consists of a set of three radially arranged cantilever blades, clamped at the base to a common frame ring, opposing each other via a central disk. The blades are loaded with a 65 kg weight, as illustrated in figure 1.

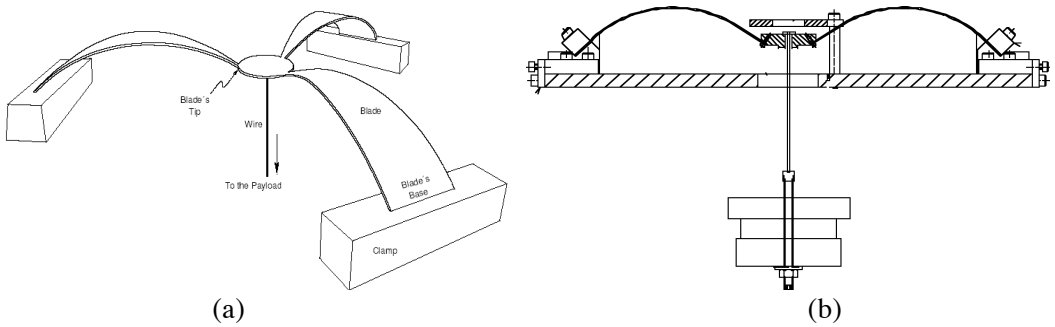

Figure 1: Schematic of a GAS filter: perspective (a) and side view (b). The flat blades are held in 45^0 clamps and pre-stressed.

The clamps can be adjusted to change the blade's horizontal compression, thus generating a theoretically arbitrarily low effective spring constant and resonant frequency, through to the resulting Anti-Spring effect [2].
The GAS mechanism has been used to null 95 to 96% of the spring restoring force at the filter working point, in order to explore hysteresis and any other underlying effects.
The theoretical transfer function of such a filter is

$$H_z(\omega) = \frac{{\omega_0}^2(1+i\phi)+\beta\omega^2}{{\omega_0}^2(1+i\phi)+i\gamma\omega-\omega^2} \quad (1)$$

where ω_0 is the resonant peak frequency, γ is an appropriate viscosity term that, together with the loss angle ϕ, determines the peak width, and β is a mass term which provides the saturation level of the transfer function at high frequencies. Between the resonant and the saturation frequency the amplitude of the transfer function is expected to decrease as $1/\omega^2$
Instead it has been observed that tuning the system at or below 100 mHz, an anomalous transfer function with $1/\omega$ slope appears, in the frequency range 1 to 5 Hz [3].
This anomaly cannot be explained by dissipative phenomena such as the thermoelastic effect, which, for Maraging blades 3.44 mm thick and a heat diffusion coefficient $D_{th} = 5.5\times10^{-6} m^2 s^{-1}$, would peak at a frequency of 0.73 Hz, thus outside the $1/\omega$ region of the anomalous GAS filter transfer function.
This observation, together with many others, such as the hysteresis already observed in GAS filters [4], the tilt hysteresis in Advanced LIGO mirror suspensions [5] and the run-off instability in IPs [6] motivated this study.
The next section will give an overview of the theoretical starting point of this research. In section 3 the experimental set up will be presented and in section 4 we will discuss the data analysis method and the results obtained. Section 5, finally, offers an interpretation of our results, as well as a discussion of future perspective.

2. Theoretical models

Viscosity has been very successful in explaining dissipation properties of materials, but, being proportional to speed, its effects vanish in the zero frequency limit and fails to explain static hysteresis. Low frequency experiments, such as the one presented in [7] and this paper, detect frequency independent losses and static hysteresis.
Hysteresis can be regarded as an effect of spatial disorder [8,9]: even the purest crystals contain a large amount of point (impurities, vacancies) and linear defects (dislocations).
Collective dislocation losses provide the most convincing interpretation of our experimental findings. It is well known that mobile dislocations produce dissipation in metals [10]; until now dissipation was interpreted as the result of the incoherent sum of movements of individual dislocations. In this paper we show how collective dislocation dynamics (avalanches) must be considered to explain the observed properties, including static hysteresis and amplitude dependent losses, of very low frequency mechanical oscillators.
Metallurgy has many dislocation control methods, for example in work hardening dislocations are created in such large numbers that they entangle to the point that their motion is impeded and dissipation suppressed (the material acquires a higher Q-factor and larger elasticity modulus). These trapped dislocations substantially contribute to the mechanical properties of the material: in the presence of low amplitude harmonic stresses, dislocation segments remain pinned inside the crystal and vibrate like ideal elastic strings [11].
In a precipitation hardened alloy, that is our case, as well as in most polycrystalline metals, dislocations can entangle but are not numerous enough to fully interlock, and can disentangle under stress.

Movement of a dislocation can engender domino effects spreading out from an initial point and sweeping through arbitrarily large volumes. Although vibrations of pinned dislocation segments may be extremely short lived, say, in the kHz domain, the domino effects involving large number of dislocations occur on substantially longer time scales. The observed effects we report here are in the time scale of seconds and involve up to the entire size of our flexures of ~ 38 cm. A simple model that closely interpreted our first observations is the Self Organized Criticality (SOC) [12,13]: according to this theory, one can postulate that a certain fraction of the total dislocation network can rearrange by following a self organized pattern, scale-free in space and time (a fractal scenario), thus naturally explaining the residual internal friction at zero frequency and the ubiquitous 1/f noise [14,15].
Combining SOC dislocation models with our measurements we propose the following overall picture. Entangled dislocations form a rigid lattice, which contributes to elasticity. Dislocations can be disentangled by mechanical oscillations, local stresses, or simply thermal fluctuations. If dislocations disentangle, in a domino effect, following a SOC statistic, the material elasticity is reduced and enhanced viscous-like effects are observed. The eventual re-entanglement of dislocations can explain the observed static hysteresis, while the scale-free nature of such processes can explain the unexpected 1/f slope of the GAS transfer function, as well as the presence of 1/f mechanical noise in the system and the other effects that we observed. Dislocation avalanches, finally, cannot contribute to internal friction at high frequencies because they have no time to grow, and lower losses are observed.

3. Experimental setup

The GAS filter has been tuned at low mechanical resonant frequency, tipically 200 mHz (in this experiment 220 mHz and 240 mHz tunes have been used).
The experiment has been performed in a sub-basement laboratory at Caltech, where the main sources of perturbations were due to turbulent air currents and air conditioning thermal cycles. For this reason a box around the GAS filter has been built, made of 2.5 cm thick polystyrene foam panels, which reduced the thermal fluctuations to less than a degree centigrade and deflected most air conditioning wind. However, since the thermal drift of the filter is of the order of one mm/^{0}C, while the measured effect can be on a submicron scale, an active thermal compensation was introduced. This feedback is also necessary to keep the filter at its optimal working point, which corresponds to the height where the Anti Spring effect is maximized and the restoring force of the springs is minimized. For this task an Infinite Impulse Response (IIR) feedback integrator continuously calculates the displacement of the filter from its working point, integrates it and feeds it to a vertical actuator. The actuator [16] is a voice coil mounted coaxial to the load suspension wire.
Similarly mounted, a Linear Variable Differential Transformer [17] sensor was used to acquire the filter displacement signal.
The LVDT calibration, in the linear range of the sensor, was found to be 1.28±0.01 V/mm, while the measured actuator calibration is 26.3±0.3 mN/V.
To further reduce the filter restoring force and resonant frequency, an Electro Magnetic Anti Spring (EMAS) [18] with variable gain has been implemented; it feeds the LVDT signal to the actuator introducing a negative spring constant K_{emas} into the system, to be added to the usual spring constant $K_0 = \omega^2 M$, so the resonant frequency can be expressed

$$f = \frac{1}{2\pi}\sqrt{\frac{K_0 + K_{emas}}{M}} \qquad (2)$$

with a payload M=65 Kg. The EMAS mechanism is able to drive the oscillator all the way to zero frequency or, with positive K_{emas}, to higher frequencies. All the above functions are applied via a Labview control program.

4. Data acquisition and results

4.1 Thermal drift

The LVDT signal was first acquired for several hours, without the thermal feedback: a large amount of thermal hysteresis was observed in the filter movement, as in figure 2a. When switching on the feedback mechanism, which stabilized the filter working point to within a few micron, we expected no residual hysteresis. Instead a similar fractional level of thermal hysteresis has been found in the feedback current that feeds the actuator, as in figure 2b. This observation clearly indicates that hysteresis does not originate from the filter macroscopic movement, but rather from a microscopic dynamics inside the blades.

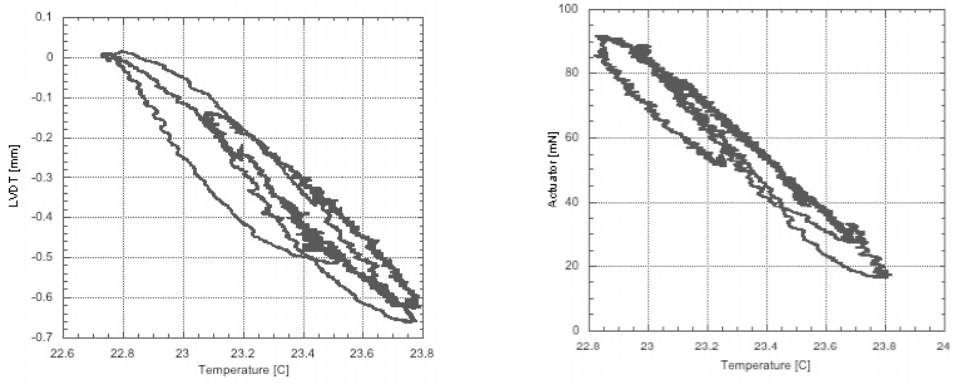

(a) (b)

Figure 2: thermal hysteresis of the filter movement subject to air conditioning thermal fluctuations without feedback (a) and variation of the control current with feedback (b). The data refer to a 10 hours acquisition.

4.2 Hysteresis versus restoring force strength

In order to explore the effects of hysteresis at different filter tunes, excitations of various amplitude and shapes have been applied through the actuator. The measurements have been repeated with alternate sign excitations to cancel thermal drift effects. A thermal feedback time constant much longer than the experiment time scale was used. The measurements were performed at different filter frequency tunes.

With an EMAS spring constant $K_{emas} = 0$ N/m, that corresponds to a resonant frequency of 220 mHz, we applied a force to the system, then slowly returned it to zero: we observed hysteresis in the GAS filter displacement, only for alternated sign excitations (figure 3a). Next, we subjected the system to the same force, but abruptly cut it when it reached its maximum, and let the system oscillate freely. No hysteresis has been observed in this case (figure 3b): apparently the system oscillations can delete hysteresis.

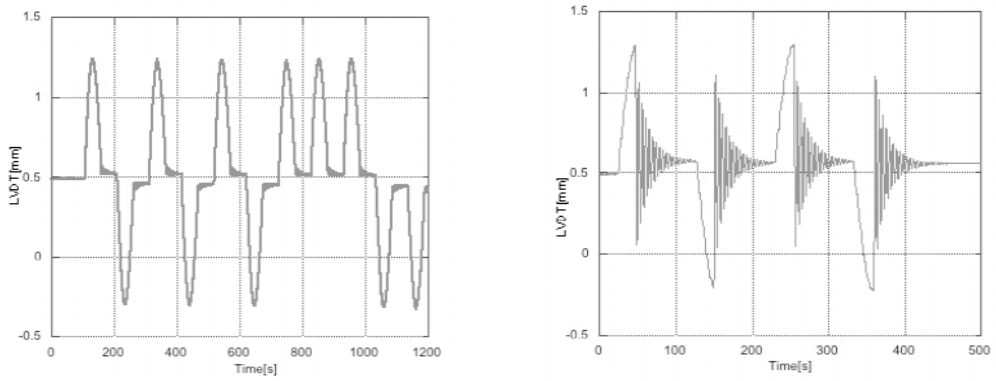

(a) (b)

Figure 3: resonant frequency 220 mHz. Pulse excitation with half period sinusoidal lifting force that grows and then fades at a speed slower than the system response time, non negligible hysteresis is observed (a). Pulse excitation with quarter period sinusoidal lifting force, no hysteresis is observed after the first excitation (b).

The same analysis has been repeated for different K_{emas}, corresponding to progressively lower resonant frequencies. For an EMAS spring constant $K_{emas} = -66.86$ N/m, that provides a resonant frequency of 150 mHz, the springs present such a low Q-factor that the residual oscillations are not sufficient to delete hysteresis in the quarter period excitation (figure 4b to be compared with figure 3b). As for the half period excitation, we found that hysteresis grows rapidly for lower frequency tunes (figure 4a).

The proposed explanation is that elasticity is composed of two parts: the bulk, immutable, provided by the crystalline structure, and a percentage provided by entangled dislocations. The second contribution changes with the dislocation's distribution: its equilibrium point depends on where the dislocation entangle and freeze. The dislocations, mobilized under the pulsed stresses, re-entangle eventually in different equilibrium position, thus explaining the observed hysteresis. The GAS and the EMAS mechanisms reduce the overall restoring force thus enhancing the effect.

The effect is dramatically evident when the system approaches the lowest frequencies, where the restoring force of the crystal lattice structure is almost nulled by the EMAS mechanism (compare figure 3a and 4a). Large excitations triggered run-off instabilities (discussed in section 4.4).

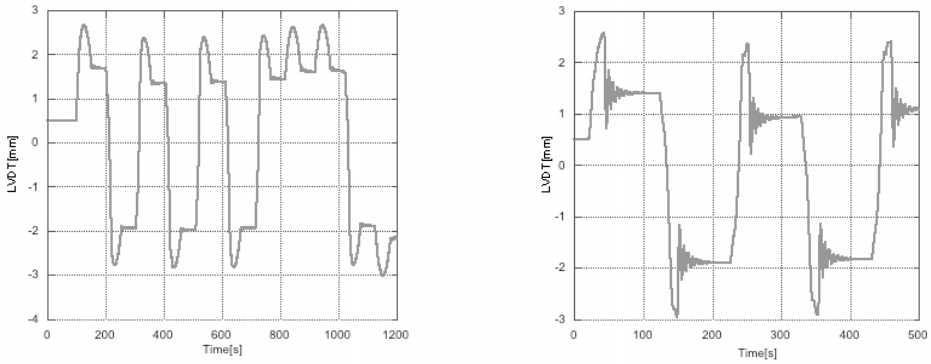

(a) (b)

Figure 4: resonant frequency 150 mHz. Half period excitation (a) and quarter period excitation (b) both show hysteresis. The amount of hysteresis is much larger than the one found with 220 mHz resonant frequency (figure 3a).

4.3 Q-factor

We performed measurements of the system Q-factor for different frequency tunings. The spring was excited by applying a short voltage pulse on the actuator for each EMAS gain setting, and the ensuing ringdown has been monitored. Because of the higher stiffness, we applied 1V excitation amplitudes at higher frequency tune, reducing it to 0.1V at lower frequency tunes, to avoid triggering run-off instabilities (discussed in section 4.4).

Analyzing the ringdown data with a damped sinusoid function we extracted the frequency and lifetime for each system tuning, thus obtaining the Q-factor defined as $Q = \omega\tau$.

The Q-factor should follow a quadratic function of frequency if the losses per cycle are frequency independent [7]; we found the expected quadratic behavior at low frequency, and a deviation from it at frequencies at or above 0.20 Hz, as if a loss mechanism were depressed at high frequencies (figure 5).

In order to verify that the observed departure from the quadratic law was not related to a non-linear control system, the filter's GAS mechanical tune has been softened 23% in stiffness (lowering its resonant frequency from 245 to 222 mHz) and the Q-factor has been measured again for several EMAS gains. The data of the two cases overlap (the two data sets are mixed in figure 5), and the point of departure from the quadratic law is unchanged. This indicates that the deviation from the f^2 law at ~200 mHz is likely a property of the material, and not tune or EMAS dependent. The observed increase of the Q-factor implies strongly reduced losses at higher frequencies; this can be explained if the dissipation process needs a longer time to develop. If the system is slow enough, a limit loss level is reached, corresponding to an hysteretic regime in which dislocation avalanches can fully grow and maximally mobilize, thus giving reason of the time independent dissipation (low Q-factor, quadratic in frequency) observed at low frequencies; at higher frequencies, less dissipation occurs, because there is no time for a full avalanche development, many dislocations are still entangled and cannot contribute to the dissipation processes.

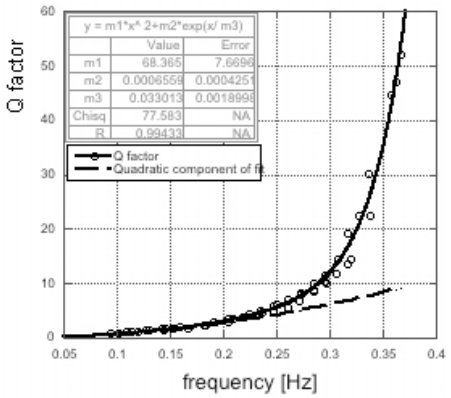

Figure 5: Q-factor of a GAS filter. The data have been analyzed with an exponential profile deviation (solid line) from a quadratic function. The dashed line is the expected quadratic component of the fit, which dominates below 0.2 Hz. Note that if the exponential fit used held all the way, the Q-factor would reach the well-known Maraging Q-factor in excess of 10,000 before 0. 5 Hz.

4.4 Low frequency instability

Exciting the system below 200 mHz we observed that the system occasionally runs away from its equilibrium point, indifferently up or down: large pulses were necessary to destabilize the system at high frequency settings, while at the lowest oscillation frequency achieved, 94 mHz, even a short pulse with amplitude of less than 3 mN (over the 65 kg payload) was able to drive the system into collapse. At lower EMAS gain, ambient perturbations are sufficient to cause the spring's run-off. It is important to remember that a stable oscillator cannot spontaneously destabilize without a failure of Hooke's law of elasticity. Unexplained collapse has been already observed in low frequency systems as different as IPs [6], Virgo [19] and TAMA IP tables, Virgo SA filters, LIGO and TAMA GAS filters [20], etc.. In order to explore the run-off instabilities, the GAS filter has been scanned with increasing negative K_{emas}, i.e. decreasing resonant frequencies, while maintaining the filter at its working point position with a slow position correction integrator. The run-offs start at random directions around 40 mHz, substantially far from the mathematical instability marked by the zero frequency in figure 6a. Evidently the perturbation level in the laboratory is sufficient to impede stability at that low frequency. Note that the initial run-off is slow, much slower than the time constant corresponding to the frequency tune, and then accelerates, as illustrated in figure 6b: this observation seems to indicate that some suddenly-activated, Young's modulus reducing mechanism occurred inside the blades. The effect can be explained if one accepts that the restoring force provided by the crystalline structure is nulled by the GAS and the EMAS mechanisms, and that the system is kept stable only through the metastable restoring force provided by the entangled dislocations. A perturbation that causes some dislocations to disentangle can trigger collapse. To explain the macroscopic run-off of the large payload, the perturbation must propagate to the entire spring's volume. It can be seen as a domino effect in which a single localized event slowly sets in motion avalanches involving a growing number of dislocations in its neighborhood. The collapse happens when a sufficient number of disentangled dislocations stop providing their share of restoring force. Avalanche propagation is not appreciable at higher frequency oscillator tune, where the more rapid oscillation of the stress field limits the development of individual avalanches, thus preventing the domino effect from extending over macroscopic distances. At low frequency dislocation avalanches can grow indefinitely producing observable macroscopic effects.

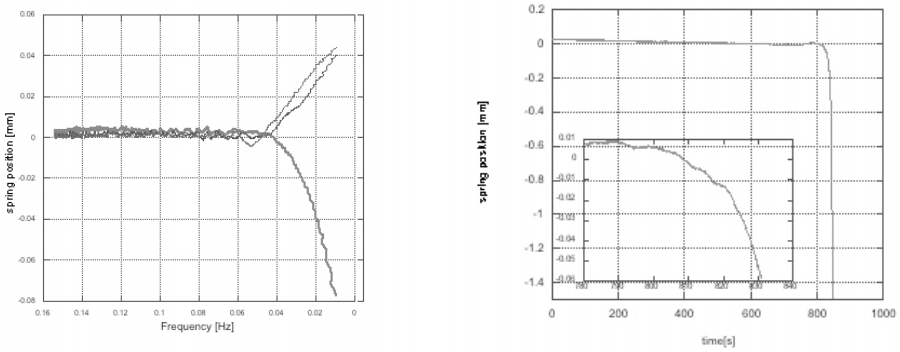

(a) (b)

Figure 6: (a) EMAS gain sweeps with run-offs of the GAS filter starting at about 40 mHz; (b) time evolution and zoom-in of a collapse event. The filter first abandons the equilibrium position very slowly (see insert), then it accelerates. It looks as if an unobserved perturbation had triggered the event by injecting some destabilization energy in the system, and the fall then provides more energy to accelerate the process.

To verify that the process involved in this fall is connected to dislocation avalanches, we wrote a program able to detect the beginning of a run-off with a threshold of 30 mV (~24 μm). The filter has been tuned under 200 mHz, inside the instability region. When a collapse is detected the program temporarily reduced the K_{emas} toward a less negative value, thus slightly increasing the resonant frequency, to give the system more rigidity. When the system has recovered equilibrium the K_{emas} is restored to the original value, following an exponential decay law (figure 7).

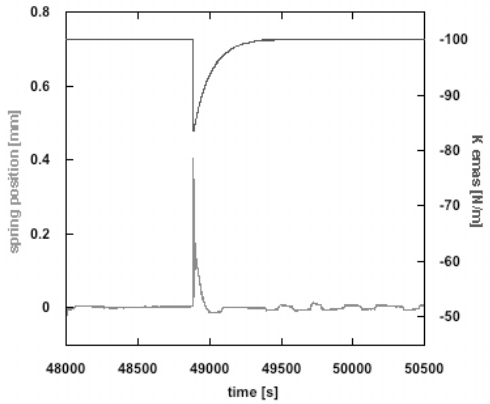

Figure 7: reducing the K_{emas} (top line), in this example from -100 to -80 N/m, the run-off (jump in the bottom line) is stopped. The filter is then slowly returned to its equilibrium position by the integrator; finally the K_{emas} returns to its original value.

4.5 Dissipation and stiffness dependence from amplitude

The stiffness and dissipation measured in forced oscillatory regime were observed to share the same amplitude dependence, proportional to the square root of the oscillation amplitude, a power law typical of SOC systems. We performed two sets of swept sine measurements one made with K_{emas} =0 N/m and one with K_{emas} =-66.86 N/m. In both cases the GAS tune was ~225 mHz. Considering a scenario involving SOC of dislocations, the total elastic constant of the system can be thought as:

$$K_{effective} = K_B + K_A A^x$$

where K_B is a fixed term and $K_A A^x$ is an amplitude dependent term, to account for the stiffness loss due to the fraction of dislocation network disentangled by the motion. The resonant frequency for the M=65kg payload mass thus becomes amplitude dependent according to the formula:

$$f = \frac{1}{2\pi}\sqrt{\frac{K_B + K_A A^x}{M}} \qquad (3)$$

Fitting the swept sine data with the previous function we expect that K_A, indicated as the fit parameter m2 in figure 8, takes a negative value if dislocation disentanglement weakens the Young's modulus.

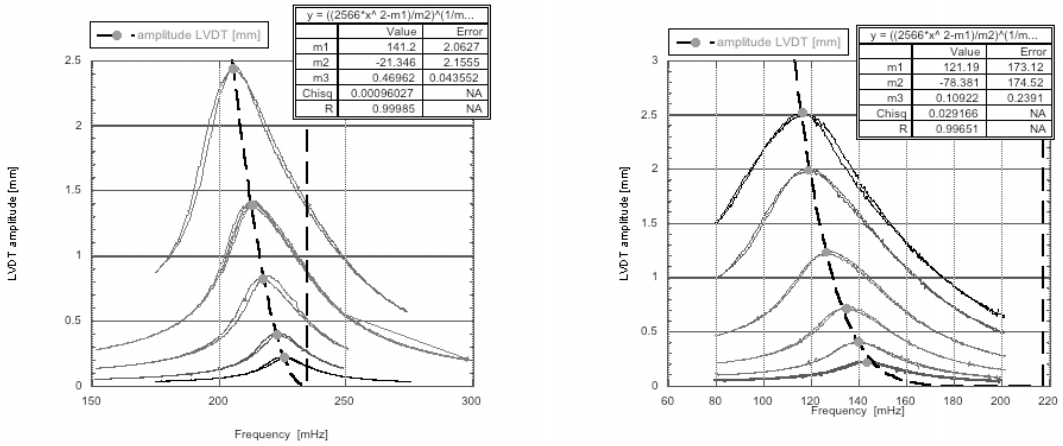

Figure 8: Swept sine response of the system. Each scan was performed sweeping the frequency first up and then down. The scans were repeated with increasing excitation amplitudes. The entire procedure was performed without EMAS, left, and with K_{emas} =-66.86 N/m, right. For each scan we identified the peak value of the resonance, and we applied the formula (3) to fit the position of the peaks.

The fitted value of the amplitude exponent (fit parameter m3 in figure 8) is x=0.5 within less than a standard deviation without EMAS and within 1.7 σ for a K_{emas} =-66.86 N/m. The amplitude-dependent frequency described by formula (3) was also observed in the time domain, studying ring-down measurements.

The assumption that disentangled dislocations weaken the material Young's modulus led us to think that the freed dislocations might cause increased dissipation. The idea was tested studying short sections of long ring-downs and analyzing them with a damped-sinusoidal function to extract the damping time τ as function of the oscillation amplitude A. Fitting the data with the following function,

$$\tau = \frac{1}{d_0 + \delta A^y} \tag{4}$$

where d_0 is the intrinsic dissipation of the material and δA^y describes a possible contribution from the disentangled dislocations, an amplitude exponent of 0.544±0.037 has been found, only 1.2 σ from the 0.5 value (fit parameter m3 in figure 9).

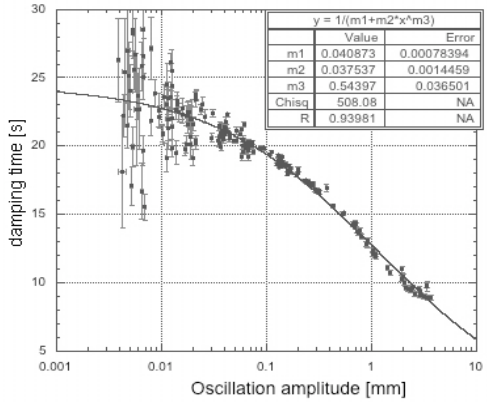

Figure 9: Ring-down lifetime versus amplitude, fitted with a "viscous" term with a power law dependence from the oscillation amplitude.

The fact that the observed loss of Young's modulus and a corresponding increase of dissipation follow the same power law give a strong indication that the two effects share the same source, most likely disentangled dislocations.

5. Conclusion and future perspective

Static hysteresis was the first indicator of something shifting inside the material. That and the previously observed 1/f transfer function of the GAS filter were explained in terms of SOC dynamics of entangled/disentangled dislocation. An avalanche dominated 1/f noise, in excess of that predicted by the fluctuation dissipation theorem, is expected at low frequencies. Individual dislocation avalanches can merge into a single plastic flow causing partial or total collapse. Dislocation avalanches also cause random walks of quiescent mechanical systems. At higher frequencies (>0.2Hz) we may be observing a different scenario. Disentanglement has no time to complete and a large fraction of the dislocations remains inactive. IP or GAS filters tuned at high frequency show well-understood damped behaviors. This may be the case of most experimental internal friction apparatuses, which are typically tuned at relatively high frequency, where dislocation collective effects are negligible. Therefore, extrapolating the result of a measurement to lower frequencies and considering only the thermal noise contribution, may lead to gross underestimation of the low frequency losses and noise. The surprising behavior observed in Maraging steel may actually be typical of most, if not all polycrystalline metals at sufficiently low frequencies. Further studies of loss mechanism are necessary to better understand and control the mechanical noise of future low-frequency interferometers, and of those presently under construction.

The presented results indicate that the most promising avenue will be to study materials or processes that would either stabilize the dislocations, or at least eliminate their collective effects. New materials and processes need to be explored to design the seismic isolation of third generation, lower-frequency GW interferometers.

Glassy materials (metals or ceramics) that do not contain dislocations may be the ultimate materials for seismic attenuation filters and inertial sensors, but need to be studied in depth, as different loss mechanisms like shear bands may still spoil their performance.

Aknowledgements

We would like to thank Christian Cepeda and John Miller for their help in making these measurements possible.

The authors gratefully thank the National Science Foundation, cooperative agreement number PHY-0823459. This document has LIGO number LIGO-P0900028-v2.

References

[1] DeSalvo R 2007 *J. Comput. Nonlinear Dynam.* **2** 290-98
[2] Cella G *et al.* 2005 *Nucl. Instrum. Methods Phys. Res. A* **540** 502-19
[3] Stochino A *et al.* 2007 *Nucl. Instrum. Methods Phys. Res. A* **580** 1559-64
[4] DeSalvo R *et al.* 2005 *Nucl. Instrum. and Meth.* **538** 526-37
[5] Greenhalgh J and Wilmut I 2008 *LIGO Technical Report* LIGO DCC T080033-01-K
[6] Saulson P *et al.* 1994 *Rev. Sci. Instrum.* **65** 182-91
[7] Kimball A L and Lovell D E 1927 *Phys. Rev.* **30** 948-59
[8] Ziman J M 1979 Models of disorder, *CUP Cambridge UK*

[9] Nowick A S and Berry B S 1972 Anelastic Relaxation in Crystalline Solids, *Academic New York*
[10] Hirth J P and Lothe J 1968 Theory of Dislocations, *McGraw-Hill New York*
[11] Granato A V and Lucke K 1966 *Physical Acoustics, edited by Mason and Thurston Academic New York* **IVA** 225
[12] Bak P *et al*. 1987 *Phys. Rev. Lett*. **59** 381-84
[13] Bak P *et al*. 1988 *Phys. Rev. A* **38** 364-74
[14] Marchesoni F and Patriarca M 1994 *Phys. Rev. Lett*. **72** 4101
[15] Marchesoni F *et al*. 1994 *Phys. Lett. A* **187** 359
[16] Wang C *et al*. 2002 *Nucl. Instrum. Methods Phys. Res. A* **489** 563-69
[17] Tariq H *et al*. 2002 *Nucl. Instrum. Methods Phys. Res. A* **489** 570-76
[18] Mantovani M and DeSalvo R 2004 *Nucl. Instrum. and Meth*. **554** 546-54
[19] Ruggi P, VIRGO project, private comm.
[20] R&D and various collaborators

Acknowledgements

I want to deeply thank my supervisor at Caltech, Riccardo De Salvo, who gave me the possibility to study there and to experience the life of an experimental physicist: I spent constructive days at the LIGO laboratory and I thank him for his numerous discussions about physics and not and for his constant work and help during the period of the experiment.
I'm grateful to my supervisor in Rome, Fulvio Ricci, for first introduced me to this field and for always supported me.
A special thanks goes to Matthew Benacquista, for his interesting advices about the astrophysics issues of this thesis, the help in the realization of chapter 3.4 and his kind hospitality at the University of Texas at Brownsville.
I want to thank Fabio Marchesoni, who collaborated with us in writing the paper above and for his help in developing the theoretical model presented here.
I'm indebted to Giulio Cimini, Maria Ascione, Abhik Bhawal and John Miller for their contribution to various sections of this thesis.
Thanks to Christian Cepeda, Larry Wallace and Melody Araya for their constant technical support during my year at Caltech.
Thanks to all the LIGO people who made my experience possible.

The LIGO Observatories were constructed by the California Institute of Technology and the Massachusetts Institute of Technology with funding from the National Science Foundation under cooperative agreement PHY 9210038. The LIGO Laboratory operates under cooperative agreement PHY-0757058. This thesis has been assigned LIGO Document Number LIGO-P0900076-v1.